Magnetoelectric resonant metamaterial scatterers

Ph.D. thesis University of Amsterdam, September 2012
Magnetoelectric resonant metamaterial scatterers
Ivana Seršić
ISBN: 978-90-77209-65-3
A digital version of this thesis can be downloaded from http://www.amolf.nl

Magnetoelectric resonant metamaterial scatterers

ACADEMISCH PROEFSCHRIFT

ter verkrijging van de graad van doctor
aan de Universiteit van Amsterdam
op gezag van de Rector Magnificus
prof. dr. D. C. van den Boom
ten overstaan van een door het college voor promoties ingestelde
commissie, in het openbaar te verdedigen in de Agnietenkapel
op dinsdag 11 september 2012, te 10.00 uur

door

Ivana Seršić

geboren te Rijeka, Kroatië

Promotor: prof. dr. A. F. Koenderink

Overige leden: prof. dr. A. Fiore
prof. dr. rer. nat. H. Giessen
prof. dr. T. Gregorkiewicz
prof. dr. A. Lagendijk
prof. dr. H. B. van Linden van den Heuvell
dr. A. P. Mosk

Faculteit der Natuurwetenschappen, Wiskunde en Informatica

The work described in this thesis was part of the research program of the "Stichting voor Fundamenteel Onderzoek der Materie (FOM)", which is financially supported by the "Nederlandse Organisatie voor Wetenschappelijk Onderzoek (NWO)". This work was also supported by the NanoNed technology program of the Dutch Ministry of Economic affairs.

This work was carried out at the *FOM Institute for Atomic and Molecular Physics, Science Park 104, 1098 XG, Amsterdam, The Netherlands*, where a limited number of copies of this thesis is available.

Contents

Chapter 1

Introduction

Metamaterials are a class of optical media that have earned much attention from the scientific community at the end of the 20th and the beginning of the 21st century. The name is derived from the Greek word *meta*, meaning 'beyond', and refers to the ability of the material to exhibit properties that are not found in nature. Metamaterials aim to mimic naturally occurring homogeneous media composed of atoms or molecules, yet made of artificially structured building blocks in order to go beyond parameters accessible with just molecular interaction with light. Beating the diffraction limit and arbitrary bending of light with the help of transformation optics are the visions that have resulted in a plethora of man-made meta-molecules for nanophotonics.

1.1 Negative index materials

Research in the field of metamaterials is driven by the possibility to control the properties of light on the nanoscale by using coupled resonant nanoscatterers to create optical materials with very unusual effective medium parameters. Engineering arbitrary values for the effective permittivity ϵ and permeability μ would allow new forms of light control based on achieving negative index materials [1–5], or transformation optics media [6, 7] that arbitrarily reroute light through space. The possibility of achieving negative index of refraction has coined the name 'negative index materials' (NIMs) [8]. Depending on the choice of parameters, a positive or a negative sign can be taken in the definition of the refractive index of a material

$$n = \pm\sqrt{\epsilon\mu}, \tag{1.1}$$

where ϵ and μ are the relative electric permittivity and magnetic permeability, respectively. The conventional choice is to choose the positive sign of the square

root, appropriate for positive ϵ and μ [2, 9]. All naturally occurring materials have μ=1 at optical frequencies since they exhibit no, or very weak, response to the magnetic field of light. Furthermore, insulators usually have $\epsilon > 1$, while metals have $Re(\epsilon) < 1$ due to the free electron gas. Light incident at an oblique angle θ_1 from a medium with n_1 upon a material with n_2 will be refracted under an angle θ_2 according to Snell's law

$$n_1 \sin\theta_1 = n_2 \sin\theta_2. \tag{1.2}$$

Veselago [1] first suggested that when a material possesses both negative ϵ and μ, a negative square root must be taken as a definition of refractive index to avoid violating causality. It follows that $n < 0$ results in two fundamental anomalies: (1) negative refraction of light at oblique incidences, and (2) phase velocity opposite to energy flow. Choosing $n_2 = -1$ in Eq. (1.2) implies a negative θ_2, i.e., light will be refracted on the same side of the normal as the incident wave. This is unlike conventional materials where light is refracted on the other side of the normal and it always bends away or towards it, but never through it, as shown in Fig. 1.1 (a). Since boundary conditions require $\boldsymbol{k}_{||}$ vector conservation, negative refraction means that the Poynting vector $\boldsymbol{S}$ has a negative sign, i.e., the energy flows away from the interface while the phase fronts travel towards the interface [1, 10]. This is easy to see from the fact that

$$\boldsymbol{S} = \boldsymbol{E} \times \boldsymbol{H} = \frac{1}{\mu}\boldsymbol{E} \times \boldsymbol{B} \propto -\boldsymbol{k}. \tag{1.3}$$

A consequence of negative refractive index is strong focusing of light through a thin negative index slab that led to the idea of perfect lensing. In order to understand how perfect lenses work, let us first consider a positive thin lens. The distance v of an object to the lens and the distance b of its image to the lens are related to the focal length f of the lens via

$$\frac{1}{v} + \frac{1}{b} = \frac{1}{f}. \tag{1.4}$$

The magnification M of a thin lens is given by the ratio of the distances of the image to the lens and the object to the lens. Turning our attention back to the perfect lens, Fig. 1.1 (b) shows a ray tracing diagram from a source at a distance $d/2$ to the image (black arrows) that is made by a slab of material with $n = -1$ and thickness d. Due to the negative refractive index, the rays are focused inside the material creating a virtual image (white arrow). A real upright image with unit magnification is created at a distance $d/2$ from the material slab. The distances of the image and the object to the lens have to conserve the relation

$$b + v + d = 2d. \tag{1.5}$$

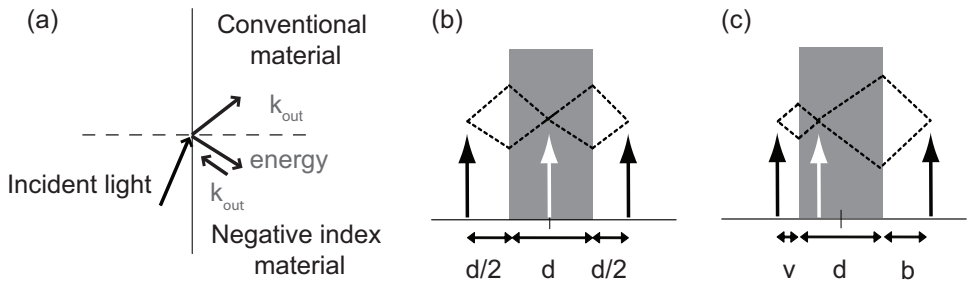

Figure 1.1: *(a) A schematic of light propagation upon refraction from a conventional material and a NIM. The wavevector points in the opposite direction to the energy flow in a NIM. (b) An object placed at a distance $d/2$ in front of a slab with $n = -1$ and thickness d will be imaged with magnification $M = 1$ on the other side of the slab. Note that a virtual image is formed within the slab. (c) If an object is placed at a distance $v < d$, it will also be imaged with the same magnification.*

As the object is brought closer to the lens in Fig. 1.1 (c), the magnification remains 1 and the total object to image distance remains constant. A real image is formed when $v < d$, while for $v > d$ no image is formed. Surprisingly, when compared to a standard positive lens, the magnification for a slab of $n = -1$ is always 1.

The unique property that initially steered attention to the field of metamaterials is not solely that a slab of $n = -1$ acts as a lens, but that it would in fact outperform any conventional lens. A usual lens is limited to a resolution no better than $\lambda/2$ due to the following argument. Suppose one has an object rich in spatial information that radiates towards the lens. Its field can be represented as

$$\boldsymbol{E}(\boldsymbol{r}, z, t) = \int \boldsymbol{E}(\boldsymbol{k}_{||}, \boldsymbol{z}_{\rm obj}) e^{i\boldsymbol{k}_{||}\boldsymbol{r} + ik_{\perp}(z - z_{\rm obj}) - i\omega t} d\boldsymbol{k}_{||}, \tag{1.6}$$

where z is the distance away from the object at a distance $z_{\rm obj}$, and towards the lens. This representation Fourier transforms the field to parallel wave vector space $\boldsymbol{k}_{||}$. The sharpest features carry the highest $\boldsymbol{k}_{||}$. However, due to the dispersion relation for vacuum ${k_{||}}^2 + {k_{\perp}}^2 = \omega^2/c^2$, any feature with $k_{||} > \omega/c$ is exponentially damped as it propagates towards the lens, since $k_{\perp}$ is imaginary. These are evanescent waves characterized by $\mathrm{Re}(k_{\perp}) = 0$ and $\mathrm{Im}(k_{\perp}) \neq 0$. Since fine details do not reach any far field lens, far field optics is limited to the diffraction limit of Abbe [2]. Resolving finer detail is hence the hallmark of near-field optics, where detection is attempted directly inside the evanescent field of the object. The unique insight of Pendry [2] that triggered interest in metamaterials, is that when an object is placed at a small, typically subwavelength distance of a thin negative index

slab, the negative index slab has a transmission coefficient far exceeding one for the evanescent wave. In fact, the perfect lens effectively amplifies the evanescent field components to such a degree that on the other side of the slab, the transmitted field exactly reconstitutes the object in the image plane [2, 11, 12]. To understand how such amplification can occur, let us analyze refraction of a propagating wave again. For $n = -1$, causality implies that the phase fronts must travel opposite to energy. In other words, the proper understanding of the ray diagram in Fig. 1.1, is that energy refracts negatively, and by causality, points from left to right throughout the diagram. Because k opposes energy flow, this means that the wave acquires *negative* phase as it propagates through the lens. All the waves recombine at the real image with net zero phase, because the negative phase acquired in the lens exactly cancels that acquired in the air. This particular argument carries over to evanescent incident waves, where the full *complex* phase is negated by the negative index medium, i.e., both the phase and the evanescent decay. It is important to realize that the only way for this reasoning not to imply violation of causality, is that the lens will only operate in a narrow frequency band and is intrinsically limited by unavoidable dispersion and absorption in the lens material [13–18]. The ability of a material to act as a perfect lens has important implications for applications where high resolution is needed, such as medical imaging, data storage, material fabrication where high resolution is needed, and as optical components [12, 19–23].

We have just seen how one might manipulate light if we choose $\epsilon = \mu = -1$. In case of arbitrary ϵ and μ, however, light can be manipulated in even more complex manner described by transformation optics. Leonhardt [6] and Pendry *et al.* [7] suggested that light can be bent in space continuously by an inhomogeneous distribution of ϵ and μ. Therefore, metamaterials offer the possibility to smoothly guide light around any object by realizing appropriate spatial variations in material parameters, i.e., both ϵ and μ. This has led to the idea of cloaking devices. An object placed within a sphere with carefully engineered values of ϵ and μ will seem invisible to any outside observer however the object is illuminated, since the cloak guides any near and far field around the object [24]. Bending of light is also of immediate importance for waveguiding, optoelectronics and photovoltaics.

1.2 Origin of material parameters

Realizing arbitrary ϵ and μ is far from trivial and requires building blocks with a response to both $\boldsymbol{E}$ and $\boldsymbol{H}$. Metamaterial building blocks are excellent candidates for realizing negative ϵ and μ provided they each have a large electric and a magnetic response to light. In order to quantify the response of such scatterers, we first need to examine how material response arises in known materials. Conventional materials consist of very dense assemblies of atoms and molecules, as shown in

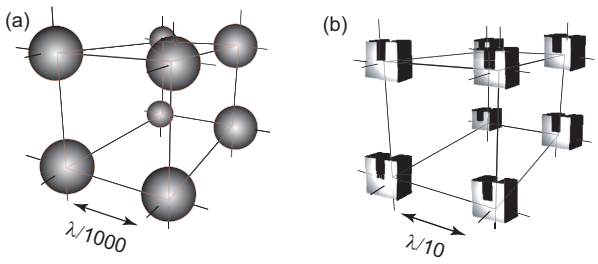

Figure 1.2: *(a) A schematic of a simple cubic crystal consisting of atoms (grey circles). (b) A schematic of the same cubic crystal with split rings as atoms.*

Fig. 1.2 (a). Typical spacings between, e.g., Si atoms in a diamond crystal structure are 3 to 5 Å [25]. Therefore, the wavelength usually exceeds the atomic spacing by a factor 1000 or more. Although generally most materials are charge neutral, they are made of polarizable particles that contribute to material polarization $\boldsymbol{P}$ and magnetization $\boldsymbol{M}$. Rather than having to treat the scattering of each atom separately, the response of the medium can be captured in constitutive parameters ϵ and μ that enter Maxwell's relations via

$$\nabla \times \boldsymbol{E} = -\mu \frac{\partial \boldsymbol{B}}{\partial t}, \quad \nabla \times \boldsymbol{H} = \epsilon \frac{\partial \boldsymbol{D}}{\partial t}, \tag{1.7}$$

where $\boldsymbol{E}$ is the electric and $\boldsymbol{H}$ is the magnetic field of light. An incident electric field $\boldsymbol{E}$ induces an electric displacement in the material

$$\boldsymbol{D} = \epsilon_0 \epsilon \boldsymbol{E} = \epsilon_0 \boldsymbol{E} + \boldsymbol{P}, \tag{1.8}$$

where ϵ_0 is the electric permittivity in vacuum. Likewise the magnetic response μ is due to material magnetization via

$$\boldsymbol{B} = \mu_0 \mu \boldsymbol{H} = \mu_0 \boldsymbol{H} + \boldsymbol{M}, \tag{1.9}$$

where μ_0 is the magnetic permeability in vacuum.

Since most materials respond strongly only to the electric field of light $\boldsymbol{E}$, in order to understand how material parameters arise, let us consider the motion of an electron bound to an atom in such a material driven by an incident electric field $\boldsymbol{E}$. According to the classical Lorentz model [26], the excitation of an electron bound to an atom is analogous to driving a harmonic oscillator with mass m on

a spring with a damping constant γ. The response of such an oscillator to the monochromatic driving $\boldsymbol{E}_0 e^{-i\omega t}$ is described by the differential equation

$$\frac{d^2\boldsymbol{x}}{dt^2} + \gamma\frac{d\boldsymbol{x}}{dt} + {\omega_0}^2\boldsymbol{x} = \frac{q}{m}\boldsymbol{E}_0 e^{-i\omega t}. \tag{1.10}$$

The resulting electron displacement is $\boldsymbol{x}(t) = \frac{q}{m}\boldsymbol{E}_0\frac{e^{-i\omega t}}{{\omega_0}^2-\omega^2-i\omega\gamma}$. Therefore, an atom acquires a dipole moment proportional to the charge separation $\boldsymbol{x}$ in Eq. (1.10),

$$\boldsymbol{p}(t) = \frac{q^2/m}{\omega_0^2 - \omega^2 - i\omega\gamma} V\boldsymbol{E}e^{-i\omega t} = \alpha(\omega)\boldsymbol{E}e^{-i\omega t}, \tag{1.11}$$

where the Lorentzian prefactor $\alpha(\omega)$ is the polarizability of the atom that describes the frequency dependent strength of the resonant response, ω is the driving frequency, ω_0 is the frequency at which the system is resonant, and γ is the damping of the material. For a material consisting of many atoms, the material polarization density $\boldsymbol{P}$ is equal to the volume average of the dipole moments $\boldsymbol{p}$.

Material polarization arises whenever the applied electric field distorts the electron distribution inducing a dipole moment $\boldsymbol{p}$, whether in a medium consisting of, e.g., molecules, plasmonic nanoparticles or metamaterial building blocks, schematically drawn in Fig. 1.3. In all cases the important figure of merit is the polarizability α defined above through $\boldsymbol{p} = \alpha\boldsymbol{E}$. A well known example where *polarizability* is applied not to an atom or molecule, but to a bigger scatterer, is that of a small sphere of dielectric constant ϵ, which in the long-wavelength limit has polarizability

$$\alpha = 3V\left(\frac{\epsilon - 1}{\epsilon + 2}\right). \tag{1.12}$$

The fact that the denominator yields a resonance in α for $\epsilon = -2$, is exploited in 'plasmonics'. Indeed, 10-100 nm sized gold and silver particles have polarizabilities far in excess of their physical volume V at frequencies where $\epsilon = -2$, which is associated with a collective response of the free electron plasma. Similarly, metamaterial building blocks are polarizable metal structures which contain magnetic polarizability in addition to an electric polarizability. Therefore, one can consider metamaterial scatterers, such as split ring resonators, as a sum of two objects with an electric dipole moment $\boldsymbol{p}$ and a magnetic dipole moment $\boldsymbol{m}$. Fig. 1.3 (b) shows how the incident electric field induces charge separation across a split ring gap, giving rise to the in plane electric dipole moment $\boldsymbol{p}$. The current oscillating in the ring will give rise to the out of plane magnetic dipole moment $\boldsymbol{m}$. Section 1.3 discusses this mechanism in detail.

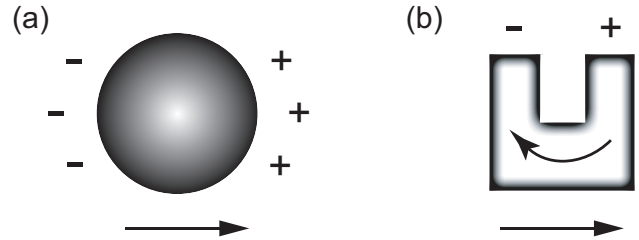

Figure 1.3: *Incident field (black arrows) induces a charge separation that sets up a dipole moment in (a) a metallic particle and (b) a metamaterial scatterer.*

1.3 Metamaterial building blocks: split ring resonator

The principle to realize metamaterials with unusual ϵ and μ is to assemble dense arrays of nano-scatterers with strong electric and magnetic polarizability that, when combined, render a strongly polarizable quasi-homogeneous medium. Therefore, it is important to remain at lattice spacings $< \lambda/2$, so that diffractive effects as in photonic crystals and gratings do not occur. We call this the effective medium limit, since the $\boldsymbol{E}$ and $\boldsymbol{H}$ only 'see' a homogeneous material. Realizing negative ϵ is relatively easy, since free electron metals by themselves supply negative ϵ at optical frequencies. However, they still maintain $\mu = 1$ at optical frequencies. In 1999, Pendry *et al.* [27] suggested that a response to the magnetic field $\boldsymbol{H}$ could be evoked via resonances of metal rings. Since then, many efforts have been aimed at further strengthening the magnetic response of metamaterial scatterers by introducing double-gap or double split ring structures [28, 29]. In the previous section we have analyzed how an electric response arises in sub-wavelength scatterers via induced dipole moments. In order to understand how the magnetic response arises in metamaterials, we examine a case of an archetypical metamaterial building block, the split ring resonator (SRR).

A split ring resonator exhibits strong resonances in the visible and infra-red regime as an electric and magnetic response to both components of the electromagnetic field of light. The magnetoelectric response is electrostatically described as an LC circuit with a parallel plate capacitance C and inductance L of an N-loop coil with $N = 1$. We can calculate the LC frequency of a split ring by a simple electrostatic formula

$$\omega = \frac{1}{\sqrt{LC}} \tag{1.13}$$

where L is the inductance and C the capacitance of the Au ring. Assuming the

'coil' has one loop, the inductance of a solenoid becomes

$$L = \frac{\mu_0 A_{\text{loop}}}{t}, \tag{1.14}$$

where A_{loop} is the area of the loop. The parallel-plate capacitance is given by

$$C = \epsilon \frac{wt}{d}, \tag{1.15}$$

where w, d and t are the dimensions of the capacitor as noted in Fig. 2.2 (a). The incident magnetic field $\boldsymbol{H} = \boldsymbol{H}_0 e^{-i\omega t}$ can drive a current in the ring that sets up a voltage over the loop via Faraday's law

$$V = -\oint \frac{d\boldsymbol{H}}{dt} \mu_0 dA = i\omega\mu_0 \boldsymbol{H}_0 e^{-i\omega t} A_{\text{loop}}. \tag{1.16}$$

Vice versa is also true. Incident electric field can excite charge separation across the SRR gap, consequently inducing a current in the ring, as shown in Fig. 1.3 (b). The current induced in the ring depends on the impedance Z via Ohm's law $V = I \cdot Z$, with the impedance of an LC circuit given by

$$Z = i\omega L + \frac{1}{i\omega C} + R, \tag{1.17}$$

where R is the Ohmic resistance of the circuit. The current sets up a magnetic dipole moment $m = IA_{\text{loop}}$ pointing out of the loop. Since evidently, $\omega = 1/\sqrt{LC} \propto$ size, scaling down split rings pushes the resonance to optical frequencies [30].

The first metamaterial made of cm-sized double-SRRs resonant structures was reported in [28, 31], where negative refraction was demonstrated in the microwave regime. The promise of NIMs in the visible part of the electromagnetic spectrum, i.e., to create transformation optical devices such as cloaks and near field lenses, has prompted state-of-the art fabrication of split rings with very small dimensions [31–35]. However, due to the material properties of the most commonly used metal, Au, size scaling ultimately reaches its limit at frequencies approaching the Au plasma frequency [34]. Though the choice of metal determines the LC frequency limit, resonance frequencies have remained above 750 nm [34].

Negative refractive index has furthermore been studied in literature in structures fabricated in metal-dielectric multilayers [36–39], such as rod-pairs [40] and coaxial waveguides [41]. Shalaev *et al.* [40] have reported on a NIM in the optical regime (1.5 μm) consisting of pairs of parallel Au nanorods. These cut-wire pair structures consist of two nobel metal wires separated by a dielectric, as shown in Fig. 1.4 (a), where the light incident along the stacking axis induces an

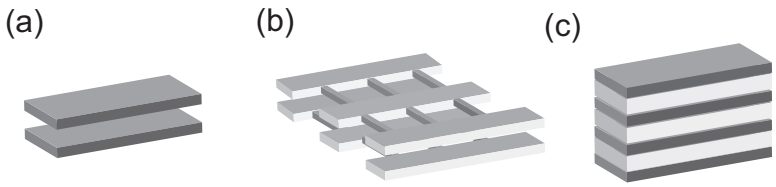

Figure 1.4: *Schematic representation of metamaterials (a) cut-wire pair [40, 42], (b) fishnet structure [43–45], and (c) metal-dielectric multilayer [39].*

anti-symmetric mode resulting in a magnetic dipole moment induced between the wires [42]. Particularly interesting is the fishnet structure where wire pairs ($\epsilon < 0$) and parallel-plate pairs ($\mu < 0$) are fabricated together in metal-dielectric-metal multilayers and together make up $n < 0$ [43–45], as shown in Fig. 1.4 (b). Chettiar *et al.* [37] fabricated a film similar to the fishnet structure consisting of perforated silver multi-layer on a glass substrate separated by a dielectric. In the near field, Zhang *et al.* [36] experimentally demonstrated negative index at 2 μm via resonant interactions of nanoholes in a multilayered metal-dielectric fishnet film. Recently, Verhagen *et al.* [39] studied a metal-dielectric multilayer structure where refractive index is based on coupling between adjacent plasmonic waveguides. Such a multilayer structure is schematically shown in Fig. 1.4 (c).

1.4 Metamaterial building blocks as scatterers

Many researchers have recently aimed to achieve negative refractive index by stacking metamaterial building blocks in densely packed arrays. Due to the existence of both electric and magnetic dipoles, these scatterers are expected to couple strongly in arrays. Such coupling can at the same time result in unwanted complications when predicting and engineering ϵ and μ, yet also can provide valuable insight in the relative strengths of the electric and magnetic dipole moments. The key question of this thesis is to identify what the polarizability that underlies the electric and magnetic response is, and how dipole-dipole coupling can be quantified. We wish to quantify how large the polarizability α of metamaterial building blocks is, and to identify if any magnetic character is evident in scattering. Experiments outside the domain of effective media have appeared only recently. These include experiments by Husnik *et al*. [46], and Banzer *et al*. [47] that quantify the extinction cross section of single split rings under differently polarized illumination, experiments where split ring resonators act as near field probes [48, 49], as well as a range of experiments on coupled systems. These experiments include extinction measurements on split ring dimers [50] that point at resonance hybridization, as

well as reports of magnetization waves [51], structural and geometrical chirality in arrays, as evident in, e.g., massive circular dichroism [52–59], and chiral effects in split ring stereo-dimers studied by Liu *et al*. [60]. In many instances, metamaterial building blocks are in fact very strong scatterers with large cross sections [46, 61–63], comparable to the large cross sections of plasmonic structures. Therefore, metamaterial building blocks are excellently suited to construct magnetic antennas, array waveguides and gratings in which electric and magnetic dipoles couple and form cooperative excitations, in analogy to the functionality imparted by plasmon hybridization [64].

In order to introduce the measures that quantify how strongly nanoscatterers scatter, let us consider the simple textbook problem of a nanoparticle placed in a homogeneous electromagnetic field. The nanoparticle will either absorb part of the light, or it will cause light to be scattered and propagate in different directions. These phenomena both take power out of the incident beam, which is termed 'extinction'. Energy conservation means that extinction equals absorption plus scattering

$$\text{Extinction} = \text{Absorption} + \text{Scattering}. \tag{1.18}$$

Let us now suppose the particle is so small, that it can be viewed as just a polarizable point dipole

$$\boldsymbol{p} = \alpha \boldsymbol{E}_{\text{in}}. \tag{1.19}$$

The amount of energy removed from the incident beam by the dipole is called the extinction. It is equal to the cycle-average work done per unit time by the incident field $\boldsymbol{E}_{in}$ to drive the dipole $\boldsymbol{p}$,

$$W = \langle\langle \text{Re}\boldsymbol{E}_{\text{in}} \cdot \text{Re}\frac{d\boldsymbol{p}}{dt}\rangle\rangle. \tag{1.20}$$

Assuming a harmonic time dependence in the driving $\boldsymbol{E}_{\text{in}}(t) = \boldsymbol{E}_0 e^{-i\omega t}$ the time derivative of the dipole becomes $\frac{d\boldsymbol{p}}{dt} = -i\omega\alpha\boldsymbol{E}_0 e^{-i\omega t}$, where $\boldsymbol{E}_0$ is the amplitude of the incident electric field and ω is the driving frequency. Taking the real part of $\boldsymbol{E}_{\text{in}}$ and $\frac{d\boldsymbol{p}}{dt}$, the work done per cycle average becomes

$$W = \langle\langle \text{Re}\boldsymbol{E}_{\text{in}} \cdot \text{Re}\frac{d\boldsymbol{p}}{dt}\rangle\rangle = \omega \text{Im}(\boldsymbol{E}_0^* \alpha \boldsymbol{E}_0). \tag{1.21}$$

The loss of energy from the beam due to extinction normalized to the incident intensity is the extinction cross section $\sigma_{\text{ext}} = W/I$ [65]. In case of a simple spherical electric dipole scatterer, polarizability α is a scalar, and the extinction cross section (units of area) is given by

$$\sigma_{\text{ext}} = 4\pi k \text{Im}\alpha. \tag{1.22}$$

We will see in Chapter 3 how the extinction cross section depends on a tensorial and magnetoelectric $\boldsymbol{\alpha}$. Once excited, the dipole re-radiates a certain field $\boldsymbol{E}_{\mathrm{out}}$ in a process called scattering. However, some of the radiation will be absorbed by the dipole, i.e., lost as heat in the scatterer, leading to a relation

$$\sigma_{\mathrm{ext}} = \sigma_{\mathrm{abs}} + \sigma_{\mathrm{scatt}}, \tag{1.23}$$

where σ_{abs} is absorption cross section and σ_{scatt} is the scattering cross section, all in units of area (m^2). The scattering cross section quantifies how much power an induced dipole radiates. It is obtained by dividing the angle integrated radiated intensity of an oscillating dipole by the incident intensity, to get

$$\sigma_{\mathrm{scatt}} = \frac{8\pi^2}{3} k^4 |\alpha|^2. \tag{1.24}$$

The ratio of scattering to extinction is called the albedo a of the particle. It tells us how much light that was taken out of the beam the particle actually re-radiates. In case of a lossless scatterer, $\sigma_{\mathrm{ext}} = \sigma_{\mathrm{scatt}}$, the albedo equals one. This means that the scattering resonance loses energy only due to radiative losses [65]. Material absorption losses limit the albedo to $a \leq 1$. Eq. (1.22) and (1.23) are best known in the context of Rayleigh scattering for very small scatterers where α is simply given by Eq. (1.12). In this regime, the equations imply the well known λ^{-4} increase of scattering strength with wavelength, and the fact that scattering scales as V^2, while absorption scales linearly with particle volume V. In other words, the smallest particles tend to just absorb, while bigger objects are strong scatterers and weak absorbers.

A fact that is not so broadly appreciated is that Eq. (1.22) and (1.23) hold equally for very strong dipole scatterers that have cross sections comparable to λ^2, though in such cases the polarizability as in Eq. (1.12) must be modified to include radiative damping. We will generalize this strongly scattering dipolar description common for plasmon scatterers [66–69] to metamaterials in Chapter 3.

1.5 This thesis

The aim of this thesis is to characterize the magnetoelectric response of metamaterial building blocks, specifically split rings, and to quantify scattering and extinction of sinlge building blocks as well as coupled systems. At the start of this work, in 2008, several groups had just recently reported on achieving negative μ using split rings [31, 33, 70]. Our quest does not revolve around engineering μ, but concentrates on identifying what the underlying polarizability α is. To this end, we have fabricated periodic arrays of split ring resonators with sub-wavelength lattice

spacing and different dimensions along x and y directions in Cartesian coordinate space. We present experimental proof of strong electric and magnetic dipole-dipole coupling of SRRs in such arrays in Chapter 2. Chapter 3 is a theoretical study of the polarizability of individual SRRs. We have developed an electrodynamic scattering model that describes the magnetoelectric response of SRRs and predicts their extinction cross sections and radiation patterns. The theory shows strong support for our experimental findings from Chapter 2 on coupling in arrays as evidenced by direct comparison in Chapter 4. Furthermore, optical activity due to the magnetoelectric coupling in the polarizability of geometrically achiral scatterers, as previously reported for molecules, is explored in Chapter 5. In Chapter 6 we describe a custom built Fourier microscope set up to image radiation patterns of single photonic structures. This set up can be used to probe radiation patterns of individual and coupled plasmonic as well as metamaterial scatterers, a possibility that is outlined in Chapter 7. Here we propose further experiments for quantifying the magnetic response, coupling and optical activity of SRRs, as well as potential applications.

Bibliography

[1] V. G. Veselago, Sov.Phys. USPEKHI **10**, 509-514 (1968).

[2] J. B. Pendry, Phys. Rev. Lett. **85**, 3966 (2000).

[3] J. B. Pendry, Physics World **14**, 47 (2001).

[4] C. M. Soukoulis, S. Linden, and M. Wegener, Science **315**, 47 (2007).

[5] V. M. Shalaev, Nature Photonics **1**, 41 (2007).

[6] U. Leonhardt, Science **312**,1777 (2006).

[7] J. B. Pendry, D. Schurig, and D. R. Smith, Science **312**, 1780 (2006).

[8] C. M. Soukoulis, M. Kafesaki, and E. N. Economou, Adv. Mater. **18**, 1941 (2006).

[9] J. D. Jackson, *Classical Electrodynamics (3rd ed.)*, John Wiley & Sons, New York (1999).

[10] N. Engheta and R. W. Ziolkowski, *Metamaterials: Physics and Engineering Explorations*, John Wiley & Sons, USA (2006).

[11] D. R. Smith, J. B. Pendry, and M. C. K. Wiltshire, Science **305**, 788 (2004).

[12] N. Fang, H. Lee, C. Sun, and X. Zhang, Science **308**, 534 (2005).

[13] G. W. 't Hooft, Phys. Rev. Lett. **87**, 249701 (2001).

[14] J. M. Williams, Phys. Rev. Lett. **87**, 249703 (2001).

[15] J. B. Pendry, Phys. Rev. Lett. **87**, 249702 (2001).

[16] J. B. Pendry, Phys. Rev. Lett. **87**, 249704 (2001).

[17] N. Garcia and M. Nieto-Vesperinas, Phys. Rev. Lett. **88**, 207403 (2002).

[18] N. Garcia and M. Nieto-Vesperinas, Phys. Rev. Lett. **90**, 229903 (2003).

[19] X. Zhang and Z. Liu, Nat. Mater. **7**, 435 (2008).

[20] T. Taubner, D. Korobkin, Y. Urzhumov, G. Shvets, and R. Hillenbrand, Science **313**, 1595 (2006).

[21] Z. Liu, H. Lee, Y. Xiong, C. Sun, and X. Zhang, Science **315**, 1686 (2007).

[22] I. I. Smolyaninov, Y. J. Hung, and C. C. Davis, Science **315**, 1699 (2007).

[23] Y. Xiong, Z. Liu, C. Sun, and X. Zhang, Nano Lett. **7**, 3360 (2007).

[24] J. Valentine, J. Li, T. Zentgraf, G. Bartal, and X. Zhang, Nat. Mater. **8**, 568 (2009).

[25] W. C. O'Mara, R. B. Herring, and L. P. Hunt, *Handbook of Semiconductor silicon technology*, Noyes Publications, 1990.

[26] L. Novotny and B. Hecht, *Principles of Nano-Optics*, Cambridge University Press, UK (2006).

[27] J. B. Pendry, A. J. Holden, D. J. Robbins, and W. J. Stewart, IEEE Trans. Microwave Theory Tech. **47**, 2075 (1999).
[28] R. A. Shelby, D. R. Smith, and S. Schultz, Science **6**, 77 (2001).
[29] K. Aydin, I. Bulu, K. Guven, M. Kafesaki, C. M. Soukoulis, and E. Ozbay, New J. Phys. **7**, 168 (2005).
[30] K. Busch, G. von Freymann, S. Linden, S. F. Mingaleev, L. Tkeshelashvili, and M. Wegener, Phys. Rep. **444**, 101 (2007).
[31] D. R. Smith, W. J. Padilla, D. C. Vier, S. C. Nemat-Nasser, and S. Schultz, Phys. Rev. Lett. **84**, 4184 (2000).
[32] C. Enkrich, M. Wegener, S. Linden, S. Burger, L. Zschiedrich, F. Schmidt, J. F. Zhou, T. Koschny, and C. M. Soukoulis, Phys. Rev. Lett. **95**, 203901 (2005).
[33] C. Rockstuhl, T. Zentgraf, H. Guo, N. Liu, C. Etrich, I. Loa, K. Syassen, J. Kuhl, F. Lederer, and H. Giessen, Appl. Phys. B **84**, 219 (2006).
[34] M. W. Klein, C. Enkrich, M. Wegener, C. M. Soukoulis, and S. Linden, Opt. Lett. **31**, 1259 (2006).
[35] B. Lahiri, S. G. McMeekin, A. Z. Khokhar, R. M. De La Rue, and N. P. Johnson, Opt. Express **18**, 3210 (2010).
[36] S. Zhang, W. Fan, N. C. Panoiu, K. J. Malloy, R. M. Osgood, and S. R. J. Brueck, Phys. Rev. Lett. **95**, 137404 (2005).
[37] U. K. Chettiar, A. V. Kildishev, H.-K. Yuan, W. Cai, S. Xiao, V. P. Drachev, and V. M. Shalaev, Opt. Lett. **32**, 1671 (2007).
[38] H.-K. Yuan, U. K. Chettiar, W. Cai, A. V. Kildishev, A. Boltasseva, V. P. Drachev, and V. M. Shalaev, Opt. Express **15**, 1076 (2007).
[39] E. Verhagen, R. de Waele, L. Kuipers, and A. Polman, Phys. Rev. Lett. **105**, 223901 (2010).
[40] V. M. Shalaev, W. Cai, U. K. Chettiar, H.-K. Yuan, A. K. Sarychev, V. P. Drachev, and A. V. Kildishev, Opt. Lett. **30**, 3356 (2005).
[41] S. P. Burgos, R. de Waele, A. Polman, and H. A. Atwater, Nature Mat. **9**, 407 (2010).
[42] G. Dolling, C. Enkrich, M. Wegener, J. F. Zhou, C. M. Soukoulis, and S. Linden, Opt. Lett. **30**, 3198 (2005).
[43] G. Dolling, C. Enkrich, M. Wegener, C. M. Soukoulis, and S. Linden, Opt. Lett **31**, 1800 (2006).
[44] G. Dolling, M. Wegener, C. M. Soukoulis, and S. Linden, Opt. Lett. **32**, 53 (2007).
[45] J. Valentine, S. Zhang, T. Zentgraf, E. Ulin-Avila, D. A. Genov, G. Bartal, and X. Zhang, Nature **455**, 376 (2008).
[46] M. Husnik, M. W. Klein, N. Feth, M. König, J. Niegemann, K. Busch, S. Linden and M. Wegener, Nature Photonics **2**, 614 (2008).
[47] P. Banzer, U. Peschel, S. Quabis, and G. Leuchs, Opt. Express **18**, 10905

(2010).
[48] M. Burresi, D. van Oosten, T. Kampfrath, H. Schoenmaker, R. Heideman, A. Leinse and L. Kuipers, Science **326**, 550 (2009).
[49] M. Burresi, T. Kampfrath, D. van Oosten, J. C. Prangsma, B. S. Song, S. Noda and L. Kuipers, Phys. Rev. Lett. **105**, 123901 (2010).
[50] N. Feth, M. König, M. Husnik, K. Stannigel, J. Niegemann, K. Busch, M. Wegener, and S. Linden, Opt. Express **18**, 6545 (2010).
[51] M. Decker, S. Burger, S. Linden, and M. Wegener, Phys. Rev. B **80**, 193102 (2009).
[52] J. K. Gansel, M. Thiel, M. S. Rill, M. Decker, K. Bade, V. Saile, G. von Freymann, S. Linden, and M. Wegener, Science **325**, 1513 (2009).
[53] E. Plum, J. Zhou, J. Dong, V. A. Fedotov, T. Koschny, C. M. Soukoulis, and N. I. Zheludev, Phys. Rev. B **79**, 035407 (2009).
[54] E. Plum, X.-X. Liu, V. A. Fedotov, Y. Chen, D. P. Tsai, and N. I. Zheludev, Phys. Rev. Lett. **102**, 113902 (2009).
[55] S. Zhang, Y.-S. Park, J. Li, X. Lu, W. Zhang, and X. Zhang, Phys. Rev. Lett. **102**, 023901 (2009).
[56] B. Wang, J. Zhou, T. Koschny, M. Kafesaki, and C. M. Soukoulis, J. Opt. A: Pure Appl. Opt.. **11**, 114003 (2009).
[57] E. Plum, V. A. Fedotov and N. I. Zheludev, J. Opt. A Pure Appl. Opt. **11**, 074009 (2009).
[58] M. Decker, M. W. Klein, M. Wegener, S. Linden, Opt. Lett. **32**, 856 (2007).
[59] M. Decker, R. Zhao, C. M. Soukoulis, S. Linden, M. Wegener, Opt. Lett. **35**, 1593 (2010).
[60] N. Liu, H. Liu, S. Zhu and H. Giessen, Nature Photonics **3**, 157 (2009).
[61] C. Rockstuhl, F. Lederer, C. Etrich, T. Zentgraf, J. Kuhl, and H. Giessen, Opt. Express **14**, 8827 (2006).
[62] T. D. Corrigan, P. W. Kolb, A. B. Sushkov, H. D. Drew, D. C. Schmadel, and R. J. Phaneuf, Opt. Express **16**, 19850 (2008).
[63] A. Pors, M. Willatzen, O. Albrektsen, and S. I. Bozhevolnyi, J. Opt. Soc. Am. B **27**, 1680 (2010).
[64] E. Prodan, C. Radloff, N. J. Halas and P. Nordlander, Science **302**, 419 (2003).
[65] A. Lagendijk and B. A. van Tiggelen, Phys. Rep. **270**, 143 (1996).
[66] P. de Vries, D. V. van Coevorden, and A. Lagendijk, Rev. Mod. Phys. **70**, 447 (1998).
[67] W. H. Weber and G. W. Ford, Phys. Rev. B. **70**, 125429 (2004).
[68] A. F. Koenderink and A. Polman, Phys. Rev. B **74**, 033402 (2006).
[69] F. J. García de Abajo, Rev. Mod. Phys. **79**, 1267 (2007).
[70] S. Linden, C. Enkrich, M. Wegener, J. Zhou, T. Koschny, and C. M. Soukoulis, Science **306**, 1351 (2004).

Chapter 2

Electric and magnetic dipole coupling in split ring arrays

We present experimental observations of strong electric and magnetic interactions between split ring resonators in metamaterials. We fabricated near-infrared (1.4 μm) planar metamaterials with different inter-split ring spacings along different directions. Our transmission measurements show blueshifts and redshifts of the magnetic resonance, depending on ring orientation relative to the lattice. The shifts agree well with a simple model with simultaneous magnetic and electric near-field dipole coupling. We also find large broadening of the resonance, accompanied by a decrease in effective cross section per split ring with increasing density. These effects result from superradiant scattering. Our data may shed new light on Lorentz-Lorenz approaches to metamaterials.

2.1 Introduction

Full control over ϵ and μ requires 'metamaterials' of artificial nano-scatterers with electric and magnetic response, arranged in sub-wavelength arrays. The archetypical building block is the split ring resonator consisting of a single cut metal loop with an inductive response. In recent years the field of metamaterials has made tremendous progress in shifting the resonant response from microwave to optical frequencies [1–9]. An important conceptual question is whether the effective response captured by ϵ and μ is influenced by coupling between constituents. Coupling between SRRs in vertical 1D stacks [10, 11] has attracted great attention lately outside the scope of metamaterials, e.g., for magnetic waveguides [10, 12–14], antennas [15], metamaterial lasers [16], and stereomaterials [17, 18]. Although constituent coupling might be anticipated to affect effective medium parameters [19],

measured effective responses have been attributed to single constituents in all experiments on metamaterial arrays to date.

In this chapter we present the first measurements of strong constituent coupling in planar SRR metamaterial arrays. We fabricated and characterized SRR lattices with a magnetic response at $\lambda = 1.4$ μm [4, 5] in which we vary the spacing between SRRs along different lattice directions independently, as described in Section 2.2. In Section 2.3 we observe large redshifts and blueshifts in the transmission resonances depending on SRR orientation relative to the lattices. We establish that in-plane electric-electric dipole coupling and out-of-plane magnetic-magnetic dipole coupling are strong competing interactions. In subsection 2.3.2 we explain the shifts by a quasistatic electric and magnetic dipole coupling model [11], that enables us to estimate the static magnetic and electric polarizability of SRRs. Finally, in subsection 2.3.3 we discuss the role of dynamic effects on the metamaterial resonance, which are evident in density-dependent broadening and a saturation of the transmission.

2.2 Methods

We have fabricated Au split rings arranged in arrays on glass substrates by electron beam lithography and lift-off using poly(methyl methacrylate) (PMMA) resist [14], without any adhesive layers. Fig. 2.1 shows a schematic of the fabrication process. A Raith e-LiNE electron beam lithography machine was set to a beam current of 0.04 nA at 20 keV voltage, 10 μm aperture size, and a nominal dose of 160 μC/cm^2. We spin coated a bi-layer of PMMA (120 nm /100 nm thickness) separated by a thin 15 nm Ge layer on base-piranha cleaned glass substrate (10$\times$10$\times$0.5 mm, PGO). Once the structures were written with the e-beam, the sample was developed in 3:1 methyl isobutyl ketone:isopropyl alcohol (MIBK:IPA) solution. An undercut in the lowest PMMA layer is necessary as to avoid deposition of Au onto the PMMA walls, and its subsequent lift-off with the PMMA layer. Ge is used as a mask during plasma etching of the lowest layer of PMMA. The two PMMA layers have different densities which ensure that the undercut is formed. After etching, 30 nm of Au was evaporated in a physical vapor deposition machine (p$\sim 10^{-7}$ mbar) after which the remaining PMMA layer was removed in a lift-off in acetone at 60°C. Geometrical parameters are determined after scanning electron microscope (SEM) imaging with image analysis software developed in Matlab.

A split ring with dimensions shown in Fig. 2.2 (a), (length $l = 200$ nm, width $w = 80$ nm, thickness $t = 30$ nm, and gap size $d = 80$ nm) is expected to exhibit a resonant response at $\lambda = 1500$ nm. It can be noted from Eq. (1.13) that the frequency of the resonance will directly depend on the physical dimensions of the split ring as 1/SRR size, and will further vary as gap width, arm width and thickness

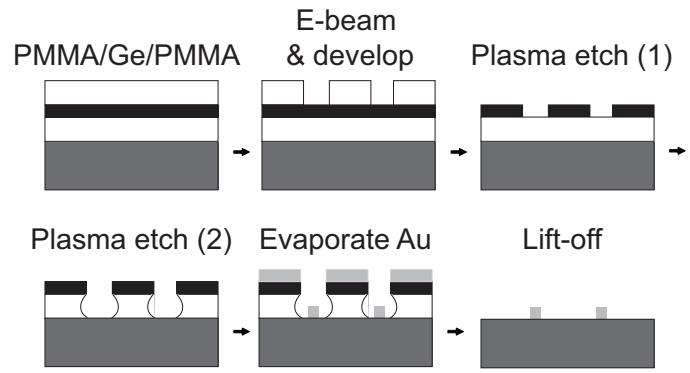

Figure 2.1: *A schematic of a step-by-step fabrication process of Au split rings on a glass substrate with electron beam lithography.*

are changed, due to changes in L and C. The electron beam dose determines the lateral dimensions of the structure, and depends on the e-beam current, beam step size, and beam dwell time. Furthermore, the dose, and hence size of the SRR, can be affected via proximity effects of the beam during writing of the nearest neighbor structures in arrays. Therefore, we have investigated the effects of size variation on the LC resonance shifts prior to studies dependent on lattice density.

We quantify the LC resonance by optical transmission measurements. The transmission was measured in a commercially available Witec confocal microscope set up. The set up consists of a movable stage on which the sample is mounted, used for navigation across the sample. A low NA lens (f=100 mm) is mounted in the illumination path as to ensure quasi-collimated illumination from the Ando fiber coupled halogen lamp. The transmitted intensity is collected with a 50x objective and the spectra are collected by a Princeton Instruments Si CCD spectrometer for visible wavelengths and InGaAs array for IR resonances. Fig. 2.2 (b) shows transmission through arrays of SRRs with lattice spacing $d = 500$ nm, exposed with different e-beam doses with dose scaling ranging from 1 to 1.5 times the nominal dose. Insets in Fig. 2.2(b) (from 1 to 5) show the variations in SRR dimensions. These are: vertical arm length l_1=170, 180, 195, 200, 200; horizontal arm length l_2=185, 190, 200, 200, 200; gap width $d = 100, 105, 90, 90, 85$, and gap depth $w =$ 65, 80, 80, 80, 80 nm ($\pm$ 5 nm error). At this lattice spacing, almost no coupling of SRRs in arrays is expected and therefore resonance shifts can only occur due to the geometrical parameters of the split rings. Fig. 2.2(b) shows that the transmission has two features. The feature at 1500 nm is the LC resonance, while the feature at 800 nm is a higher order resonance that we disregard in this work. Fig. 2.2(b) shows that only the center position of the transmission minimum at 1500 nm varies

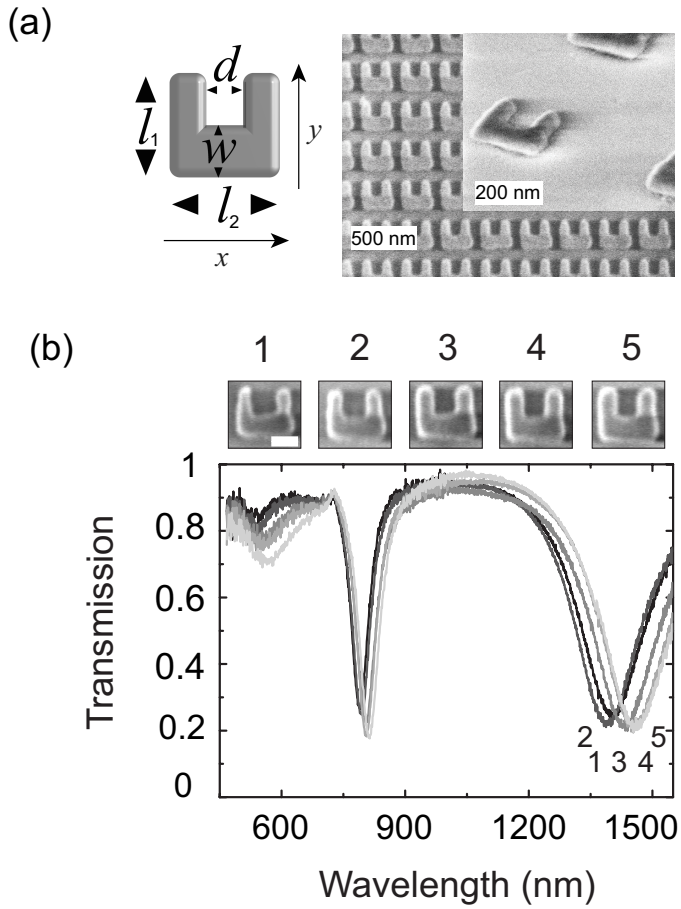

Figure 2.2: *(a) A sketch of a split ring with indicated lateral dimensions. We fabricated arrays of Au split rings on glass with periodicities $d_{x,y} = 300$ nm (SEM micrograph) and larger (inset). (b) Transmission spectra of split ring samples arranged in identical lattices but different per-split ring size show a geometry dependence of the LC resonance frequency. The SEM insets show a zoom in of split rings with lattice spacing $d_x = d_y = 500$ nm. The scale bar size is 100 nm.*

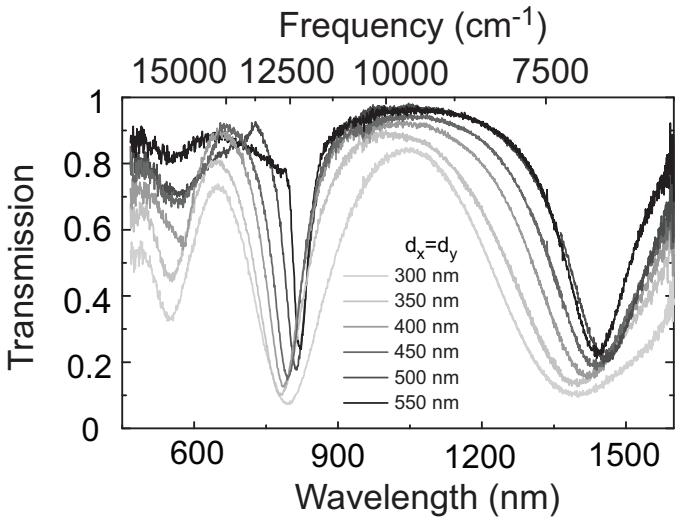

Figure 2.3: *Transmission spectra for square split ring arrays with periodicities $d_{x,y} = 300$ nm and larger (polarization along x). The magnetic resonance at 1.4 μm blueshifts and broadens with increasing density. Each split ring has l =200 nm, $w = 80$ nm, $d = 80$ nm and $t = 30$ nm ($\pm = 5$ nm).*

with varying SRR dimensions, while width and depth of the transmission minimum are negligibly affected. In general, reducing the lateral parameters l of SRRs results in shifting of the resonance towards visible frequencies. From our measurements, it can be seen that a 20% increase in l results in 50 nm resonance shift towards the IR, due to an inverse dependence of the resonance frequency on the SRR arm length. However, if l is increased, while d is decreased (1, 2), the resonance shifts towards the visible part of the spectrum, due to the square root dependence of the resonance on capacitor size.

Since the frequency of the resonance directly depends on the physical dimensions of a split ring, we took great care to produce SRRs of identical dimensions for our study on arrays of different densities, using image analysis of SEM micrographs (see Fig. 2.2) to overcome proximity effects by post-selecting samples to match a targeted size. Based on [4], our SRRs ($l_1 = l_2$ =200 nm, $t = 30$ nm, $d = 80$ nm, $w = 80$ nm) are expected to have an LC resonance at 1.4 μm. Although driven by the electric field [20, 21], we refer to the resonance as 'magnetic', consistent with literature [22, 23]. To resolve the coupling strength between SRRs along the x (along SRR base) and y (along SRR arms) directions separately, we varied the pitches d_x and d_y independently between 300 nm and 550 nm, staying below 550 nm to avoid grating diffraction in the range of the magnetic resonance.

We measured polarization-resolved normal incidence transmission using the set up reported in Ref. [14]. We illuminated a mm-sized area on the sample with a beam from a halogen lamp (5° opening angle) and used a 20 μm pinhole in an intermediate image plane to select the transmitted intensity from single 36×36 μm^2 SRR arrays, which we spectrally resolved by cooled Princeton Instruments Si CCD and InGaAs array spectrometers, and normalized to transmitted intensity through bare substrate.

2.3 Results

2.3.1 Transmission measurements

Fig. 2.3 shows x-polarized transmission spectra measured on a sample with square lattices ($d_x = d_y$) of $200 \times 200 \times 30$ nm SRRs with split width $d = 80$ nm. We observe the magnetic resonance at 1.4 μm only for polarization along x, as reported by [4, 5, 20, 21], as well as higher order plasmon resonances at 500 nm and 800 nm [4]. Incident light polarized along the long axis of the SRR , i.e., along y, excites plasmons that due to the length of the arms exhibit resonances in the visible part of the spectrum. In this chapter we focus on the magnetic resonance only. Tracing the minimum in transmission versus SRR density in Fig. 2.3, we find that the resonance blueshifts as SRRs are brought closer. A blueshift upon increased coupling is expected by analogy with plasmon hybridization [12, 13, 24], since the magnetic dipoles are all oriented perpendicular to the SRR plane, and hence transversely coupled. To study this coupling in detail, we fabricated samples with a large set of SRR arrays (split width $d = 100$ nm) where d_x and d_y are varied independently. We expect a blueshift with increasing density for all arrays since the magnetic dipoles are always transversely coupled. In Fig. 2.4(a) we plot the measured center frequency of the resonance versus SRR spacing for three sets of arrays. For square lattices $d_x = d_y$ we indeed observe a continuous blueshift, confirming the data for gap width $d = 80$ nm in Fig. 2.3(b). We also observe a blueshift when only d_y is varied ($d_x = 500$ nm). Remarkably, we measure a redshift when only d_x decreases and d_y is fixed at 500 nm. This result is surprising since redshifts imply longitudinal coupling, which is inconsistent with the orientation of the magnetic dipoles. The redshift can only be understood by noting that SRRs also have an electric polarizability in addition to a magnetic dipole [11, 20, 21]. The electric dipole moment points along the SRR base, hence allowing for longitudinal coupling in the plane of the sample.

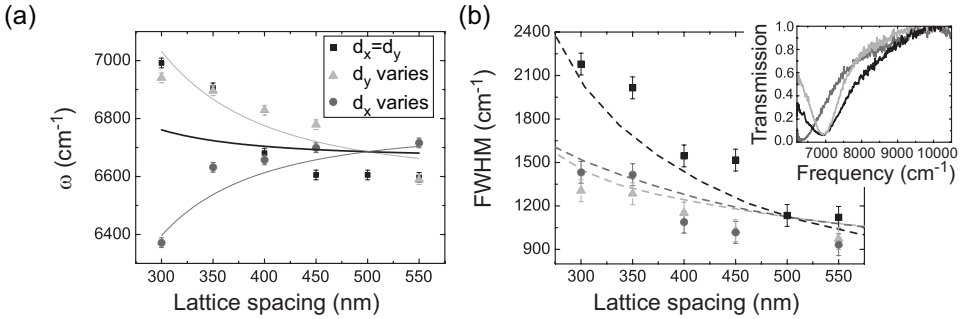

Figure 2.4: *(a) Frequency of the magnetic resonance versus lattice spacing. The frequency blueshifts when decreasing d_y whether $d_y = d_x$ (black squares) or not (light gray triangles, $d_x = 500$ nm), while it redshifts when decreasing d_x (dark gray circles, $d_y = 500$ nm). The inset shows raw spectra for $d_x = d_y = 300$ nm (black curve), $d_x = 500$ nm, $d_y = 300$ nm (light gray curve), $d_x = 300$ nm, $d_y = 500$ nm (dark gray curve). (b) FWHM of the magnetic resonance versus lattice spacing (color coding as in (a)). Curves are theory (electrostatic in (a), electrodynamic in (b)).*

2.3.2 Quasistatic model

We implement a model that takes into account simultaneous electric and magnetic dipole coupling, similar to the model for SRR stereodimers reported in [11]. In this model, all magnetic dipoles couple transversely while electric dipoles transversely couple along y and longitudinally along x. We limit ourselves to electrostatic and magnetostatic nearest-neighbor coupling, ignoring electro-dynamic effects, the air-glass interface, and multipole corrections. However, this model captures the main physics embodied in our observations. We will improve on this model in Chapters 3 and 4. For a system of coupled harmonic oscillators, the coupled resonances are set by the Lagrangian first formulated by Liu *et al.* [11]

$$\mathcal{L} = \sum_{i,j} \big[\frac{L}{2}(\dot{Q}_{i,j}^2 - \omega_0^2 Q_{i,j}^2) - \frac{M_h}{d_x^3}\dot{Q}_{i,j}\dot{Q}_{i+1,j} - \frac{M_h}{d_y^3}\dot{Q}_{i,j}\dot{Q}_{i,j+1} + 2\frac{M_e\omega_0^2}{d_x^3}Q_{i,j}Q_{i+1,j} - \frac{M_e\omega_0^2}{d_y^3}Q_{i,j}Q_{i,j+1}\big], \tag{2.1}$$

where L is the SRR inductance, $Q_{i,j}(\dot{Q}_{i,j})$ represents the charge (current) on the SRR at site (i, j), and where M_h and M_e quantify the mutual inductance and the electric dipole coupling with nearest neighbors only. Solving Eq. (2.1) for the

resonance frequency at normal incidence ($k_{||} = 0$) yields

$$\omega = \omega_0 \sqrt{\frac{1 - \frac{4\kappa_e}{d_x^3} + \frac{2\kappa_e}{d_y^3}}{1 - \frac{2\kappa_h}{d_x^3} - \frac{2\kappa_h}{d_y^3}}} \tag{2.2}$$

where ω_0 is the resonance frequency of a single SRR, and $\kappa_{e,h} = M_{e,h}/L$. Eq. (2.2) is similar to a prediction by Marqués et al. [19] for 3D SRR arrays. We fix $\kappa_e = 1.04{\cdot}10^{-21}$ m^3, i.e., the SRR electric polarizability, to match the resonant extinction cross section of 0.3 μm^2 measured by Husnik *et al.* [25], and we set $\kappa_h = 0.67\kappa_e$ as previously reported for a system of two vertically stacked SRRs by Liu *et al.* [11].

First, we examine predictions with either κ_e or κ_h set to 0. Fig. 2.5(a) shows the resonance ω versus $d_{x,y}$ assuming magnetic coupling only ($\kappa_e = 0$). The resonance blueshifts for decreasing $d_{x,y}$ in all cases due to transverse magnetic dipole coupling. Fig. 2.5(b) shows the resonance frequency for electric coupling only ($\kappa_h = 0$). The resonance redshifts with increasing density both for square arrays and strips of SRRs arranged side by side unless d_x is fixed at 500 nm. This result indicates that longitudinal coupling exceeds transverse coupling in square lattices of strictly in-plane dipoles. This behavior is indeed observed for the purely electric resonance at 800 nm, at least in the regime $\max(d_x, d_y) \leq 400$ nm where grating anomalies [26] (asymmetric shoulders at 750 nm in Fig. 2.3(b)) do not yet set in.

Neither model with solely electric or solely magnetic interaction is consistent with the measured shift of the 1.4 μm resonance, since we observe blueshifts in all cases except when d_x is varied and d_y is fixed. Fig. 2.5(c) shows the calculated ω taking into account both electric and magnetic interactions at κ_h=0.67κ_e. As in the data, the resonance only redshifts when decreasing the distance d_x at large d_y. In this case transverse electric coupling is weakest. The longitudinal electric coupling exceeds the sum of weak transverse electric and strong transverse magnetic coupling, leading to a net redshift. For a quantitative comparison with our data we plot the shifts in Fig. 2.5(c) together with the data in Fig. 2.4. The good quantitative agreement without any adjustable parameters confirms our interpretation that SRRs in metamaterial arrays show strong electric and magnetic dipole-dipole interactions. These interactions are best quantified in rectangular arrays, since in square arrays studied sofar [4, 5] partial cancelation obscures the magnetically induced blueshift. The data show that the ratio $\kappa_e/\kappa_h = 0.67$ reported for vertically stacked SRRs [11] is also relevant for dipole-dipole coupling in the xy-plane, allowing a direct identification of κ_e and κ_h with on-resonance electric and magnetic polarizabilities. It is remarkable that the magnetic polarizability α_H is of the same order as the electric polarizability α_E, as opposed to the normal ordering $\alpha_H \ll \alpha_E$ [27]. This conclusion is in accordance with recent estimates of Merlin [27], that SRRs have α_H comparable in magnitude to α_E provided $\mathrm{Im}\epsilon_{\mathrm{Au}} \gg \lambda/\ell$, where ℓ is the

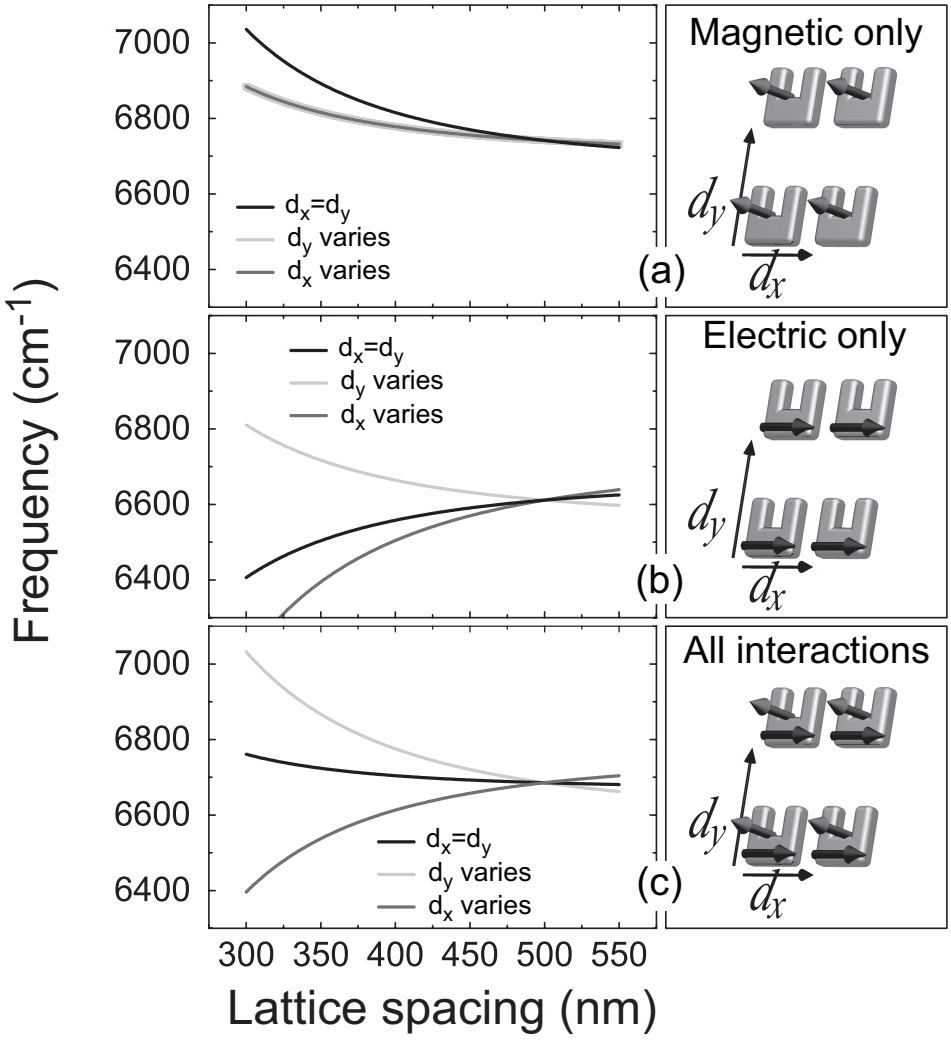

Figure 2.5: *Electrostatic calculation of the magnetic resonance frequency as a function of lattice spacing. Black curves: $d_x = d_y$. Light gray curves: d_y varies at fixed $d_x = 500$ nm. Dark gray curves: d_x varies at fixed $d_y = 500$ nm. For magnetic coupling only (a), resonances always blueshift with decreasing lattice spacing, while for electric coupling only (b), the behavior of the resonances for $d_x = d_y$ changes sign with respect to (c) (all couplings). Insets in (a), (b) and (c) are sketches of the electric and magnetic coupling between split rings. Curves in (c) are reproduced in Fig. 2.4.*

characteristic scatterer size. Given the dielectric constant of Au $\mathrm{Im}\epsilon_{\mathrm{Au}} \sim 10$, and the size $\lambda/\ell \sim 7$ of our SRRs, their LC resonances are indeed expected to be magnetic resonances with large α_H. Into the visible, $\mathrm{Im}\epsilon_{\mathrm{Au}}$ rapidly decreases, causing α_H to vanish [27], as argued independently in [9].

2.3.3 Width and depth of the resonance

A striking feature in our transmission data (*cf.* Fig. 2.3) in addition to the spectral shifts, is the large broadening of the resonance as the density of SRRs increases. In Fig. 2.4(b) we plot the measured full width at half minimum (FWHM) of the transmission minimum versus lattice spacing. For square lattices, the width more than doubles from 1000 to 2150 cm^{-1} as the pitch is reduced from 550 to 300 nm, while for both types of rectangular lattices (d_x or d_y fixed at 500 nm) the width increases from 950 to 1400 cm^{-1}. Such broadening was also noted by Rockstuhl *et al.* [5] for square arrays. Our extensive data on many rectangular and square arrays allow us to quantitatively identify the source of broadening. From the outset it is clear that the broadening is outside the scope of Eq. (2.1), since the (Ohmic) damping rate is almost independent of coupling in any electrostatic model. Instead, electrodynamical radiation damping, i.e., scattering loss into the far field must be taken into account. As all oscillators in our sub-diffraction lattices are driven in phase ($k_{||} = 0$), scattered light radiated by all oscillators interferes destructively for all angles, except along the transmitted and reflected direction. Since the magnetic dipoles are aligned along the incident beam, they do not radiate any amplitude into the $k_{||} = 0$ directions. Hence, all radiation damping is *solely* due to the induced *electric* dipoles. For a quantitative analysis we use an electrodynamical model for electric point dipoles with a Lorentzian resonance in α_E according to [13, 26], centered at 1.4 μm. We will improve on this model in Chapter 3 and 4. We use $\sigma_{\mathrm{ext}} = 4\pi k \mathrm{Im}\alpha$ with $k = 2\pi/\lambda$, using the Lorentzian electric polarizability $\alpha_0 = \omega_0^2\kappa_e/(\omega_0^2 - \omega^2 - i\omega\gamma)$ implicit in Eq. (2.2), and with radiation damping $1/\alpha = 1/\alpha_0 - i\frac{2}{3}k^3$ [13]. We take $\gamma = 1.2 \cdot 10^{14}$ s^{-1} for the Ohmic damping of Au from [28]. We evaluate Eqs. (8,9) in Ref. [26] to predict the array transmission. This dynamic model has no adjustable parameters, since the on-resonance polarizability is fixed to match the extinction cross section of single SRRs that was reported in [25]. We find a broadening of the collective transmission resonance that quantitatively reproduces the measured broadening with decreasing lattice spacing for all lattices (FWHM curves in Fig. 2.4). An important conclusion is that the large width of the magnetic response commonly observed for SRR arrays [1–5] is not due to intrinsic loss, but is quantitatively consistent with superradiant decay of the electric dipoles. The collective enhancement of the single SRR radiative linewidth, already suspected by [5], implies enhanced scattering and a reduction of the absorption of

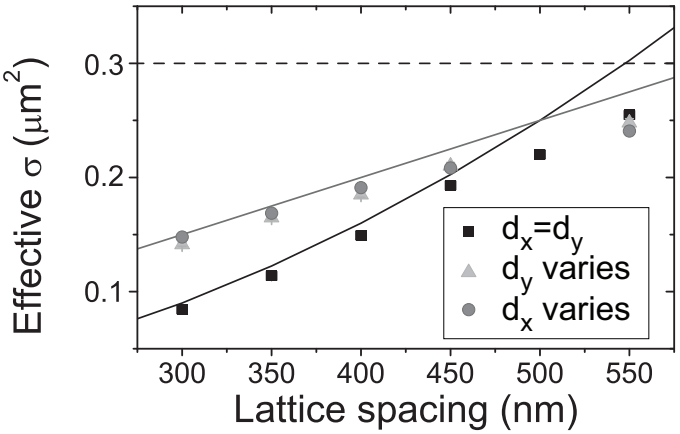

Figure 2.6: *Effective extinction cross section per split ring derived from on-resonance transmission. The black dashed line indicates the cross section of a single split ring (from [25]). The cross section per split ring is limited by the area $d_x d_y$ of the unit cell (black and gray lines).*

the array far below the albedo of single SRRs.

Finally we correlate the resonance broadening with the measured transmission T on resonance. Fig. 2.6 shows the effective extinction cross section derived from our measurements through $\sigma_{\text{eff}} = d_x d_y(1-T)$. For uncoupled scatterers we expect constant σ_{eff} equal to the extinction cross section $\sigma_{\text{ext}} = 0.3\ \mu\text{m}^2$ measured for a single SRR in [25] (dashed line in Fig. 2.6), as indeed almost found in our data for $d_x = d_y > 500$ nm. For $d < 500$ nm, we measure values for σ_{eff} far below σ_{ext} indicative of strong dipole-dipole coupling. The collective superradiant decay (Fig. 2.4(b)) which widens the resonance reduces the extinction per element to remain below the unit-cell area $d_x d_y$ (curves in Fig. 2.6).

2.4 Conclusions

In conclusion, we have measured large resonance shifts as a function of density in SRR arrays resonant at $\lambda = 1.4\ \mu$m. These shifts are due to strong near-field electric and magnetic dipole coupling that we analyzed in a quasistatic nearest neighbor model. Furthermore, we observe electrodynamic superradiant damping that causes resonance broadening and an effective reduction of the extinction cross section per SRR. Since the data show that the response of SRR arrays is not simply given by the product of the density and polarizability of single constituents, we conclude that a Lorentz-Lorenz analysis to explain effective media parame-

ters of metamaterials 'atomistically' may need to be re-assessed [29]. Indeed, our data has important repercussions: it calls for a shift away from the paradigm that the highest polarizability per constituent is required to obtain the strongest electric or magnetic response from arrays of electric or magnetic scatterers. Our experiments show that increasing the density of highly polarizable constituents to raise the effective medium response [4] is ineffective, since superradiant damping limits the achievable response. To strengthen ϵ or μ, we propose that one ideally finds constituents that have both a smaller footprint and a smaller polarizability per constituent. We stress that even if constituent coupling modifies ϵ and μ, we do not call into question reported effective medium parameters or the conceptual validity thereof per se. We propose that the effective medium parameters only loose their usefulness when constituent coupling is so strong that collective modes of differently shaped macroscopic objects carved from the same SRR array have very different resonance frequencies or widths. In this regime interesting physics comes into view, particularly regarding active devices. Specific examples are array antennas for spontaneous emission [15] and 'lasing spasers' [16], where the lowest-loss array mode will lase most easily.

Bibliography

[1] D. R. Smith, W. J. Padilla, D. C. Vier, S. C. Nemat-Nasser, and S. Schultz, Phys. Rev. Lett. **84**, 4184 (2000).

[2] W. J. Padilla, A. J. Taylor, C. Highstrete, M. Lee, and R. D. Averitt, Phys. Rev. Lett. **96**, 107401 (2006).

[3] S. Linden, C. Enkrich, M. Wegener, J. Zhou, T. Koschny, and C. M. Soukoulis, Science **306**, 1351 (2004).

[4] C. Enkrich, M. Wegener, S. Linden, S. Burger, L. Zschiedrich, F. Schmidt, J. F. Zhou, T. Koschny, and C. M. Soukoulis, Phys. Rev. Lett. **95**, 203901 (2005).

[5] C. Rockstuhl, T. Zentgraf, H. Guo, N. Liu, C. Etrich, I. Loa, K. Syassen, J. Kuhl, F. Lederer, and H. Giessen, Appl. Phys. B **84**, 219 (2006).

[6] A. N. Grigorenko, A. K. Geim, H. F. Gleeson, Y. Zhang, A. A. Firsov, I. Y. Khrushchev, and J. Petrovic, Nature **438**, 335 (2005).

[7] V. M. Shalaev, W. Cai, U. K. Chettiar, H.-K. Yuan, A. K. Sarychev, V. P. Drachev, and A. V. Kildishev, Opt. Lett. **30**, 3356 (2005).

[8] G. Dolling, M. Wegener, C. M. Soukoulis, and S. Linden, Opt. Lett. **32**, 53 (2007).

[9] M. W. Klein, C. Enkrich, M. Wegener, C. M. Soukoulis, and S. Linden, Opt. Lett. **31**, 1259 (2006).

[10] E. Shamonina, V. A. Kalinin, K. H. Ringhofer, and L. Solymar, J. Appl. Phys **92**, 6252 (2002).

[11] N. Liu, H. Liu, S. N. Zhu, and H. Giessen, Nature Photonics **3**, 157 (2009).

[12] M. L. Brongersma, J. W. Hartman, and H. A. Atwater, Phys. Rev. B **62**, R16356 (2000).

[13] A. F. Koenderink and A. Polman, Phys. Rev. B **74**, 033402 (2006).

[14] A. F. Koenderink, R. de Waele, J. C. Prangsma, and A. Polman, Phys. Rev. B **76**, 201403R (2007).

[15] J. Li and N. Engheta, Phys. Rev. B **74**, 115125 (2006).

[16] N. I. Zheludev, S. L. Prosvirnin, N. Papasimakis, and V. A. Fedotov, Nature Photonics **2**, 351 (2008).

[17] S. Zhang, Y.-S. Park, J. Li, X. Lu, W. Zhang, and X. Zhang, Phys. Rev. Lett. **102**, 023901 (2009).

[18] E. Plum, J. Zhou, J. Dong, V. A. Fedotov, T. Koschny, C. M. Soukoulis, N. I. Zheludev, Phys. Rev. B **79**, 035407 (2009).

[19] R. Marqués, F. Martin, and M. Sorolla, "*Metamaterials with Negative Parameters: Theory, Design, and Microwave Applications,*" (Wiley, Hoboken NJ, 2008).
[20] N. Katsarakis, T. Koschny, M. Kafesaki, E. N. Economou, and C. M. Soukoulis, Appl. Phys. Lett. **84**, 2943 (2004).
[21] T. Koschny, M. Kafesaki, E. N. Economou, and C. M. Soukoulis, Phys. Rev. Lett. **93**, 10 (2004).
[22] J. B. Pendry, Physics World **14**, 47 (2001); C. M. Soukoulis, S. Linden, and M. Wegener, Science **315**, 47 (2007).
[23] V. M. Shalaev, Nature Photonics **1**, 41 (2007).
[24] E. Prodan, C. Radloff, N. J. Halas, and P. Nordlander, Science **302**, 419 (2003).
[25] M. Husnik, M. W. Klein, N. Feth, M. König, J. Niegemann, K. Busch, S. Linden and M. Wegener, Nature Photonics **2**, 614 (2008).
[26] F. J. García de Abajo, Rev. Mod. Phys. **79**, 1267 (2007).
[27] R. Merlin, Proc. Natl. Acad. Sci. U.S.A. **106**, 6 (2009).
[28] P. B. Johnson and R. W. Christy, Phys. Rev. B. **6**, 4370 (1972).
[29] C. R. Simovski and S. A. Tretyakov, Phys. Rev. B **75**, 195111 (2007).

Chapter 3

Magnetoelectric point scatterering theory for metamaterial scatterers

We present a fully analytical point scattering model which can be applied to arbitrary anisotropic magnetoelectric dipole scatterers, including split ring resonators, chiral and anisotropic plasmonic scatterers. We have taken proper account of reciprocity and radiation damping for electric and magnetic scatterers with any general polarizability tensor, including magnetoelectric interactions. Our theory sheds new light on the magnitude of cross sections for scattering and extinction, and for instance on the emergence of pseudo-chirality in the optical response of geometrically non-chiral scatterers like split rings and split ring clusters. Specifically, we predict which observables in scattering experiments allow to fully quantify all components of the polarizability tensor of split rings, including their off-diagonal magnetoelectric response. Finally, we show that our model describes well the extinction of stereo-dimers of split rings, while providing a completely new interpretation of the coupling mechanisms underlying recent experiments.

3.1 Introduction

In order to understand the light-metamatter interaction in systems of strongly coupled magnetoelectric scatterers, it is important to understand how individual metamaterial building blocks are excited and how they scatter. So far, explanations of the observed phenomena have mainly rested on two pillars. On the one hand, data are compared to brute force finite-difference time-domain (FDTD) simulations of Maxwell's equations, usually showing good correspondence [1–9]. The FDTD method is essentially equivalent to performing a numerical experiment that still

requires further interpretation in order to understand how, e.g., split rings scatter or hybridize in coupled systems. There is general consensus that to lowest order, metamaterial interactions in lattices of scatterers like SRRs must be described by magnetoelectric point-dipole interactions. Hence, simple models with dipolar coupling terms are the second main interpretative tool to predict, e.g., frequency shifts due to electric and magnetic dipole-dipole interactions in lattices and oligomers. These models either take the form of dipole models in which electro-static and magneto-static polarizabilities are coupled to predict, e.g., ϵ and μ, and the existence of coupled excitations like magneto-inductive waves [10–16], or they take the form of Lagrangian equations of motion for current oscillation in coupled LC circuits [17–20], as used in Chapter 2. To rationalize this LC circuit intuition, several authors have analyzed current distributions obtained by FDTD simulations in order to retrieve the microscopic parameters (i.e., the polarizability) underlying such a dipolar interaction model, and in order to estimate multipolar corrections [5, 21–26].

While there is general consensus that to lowest order, metamaterial interactions must essentially be magnetoelectric point dipole interactions, we note that the dipolar circuit models that are adequate to explain many basic features of subwavelength clusters and metamaterial arrays, have significant limitations when applied to strong scatterers and larger clusters. This is a consequence of the fact that electric circuit theories lack the velocity of light c as a parameter, by assuming $c = \infty$ ($k = 0$) [17–20]. Such theories will be referred to in this work as 'quasi-static' or 'electro-static' and 'magneto-static'. Their validity ends when retardation or interference become important, quantitative cross sections are required or super- and subradiant radiative damping plays a role. For instance in the experiment of Chapter 2, Fig.2.4 (b) shows superradiant damping not contained in quasi-static models. A fair comparison of experiments with intuitive dipole requires a fully electrodynamic theory that (1) contains finite c, (2) satisfies energy conservation in the form of an appropriate optical theorem, and (3) can be used for dipoles with tensorial electric, magnetic, and magnetoelectric response. Indeed, actual metamaterial scatterers are very strongly bi-anisotropic, with large magnetoelectric cross coupling whereby magnetic fields induce strong electric dipoles and vice versa. We note that the theories existing sofar can be divided in two classes: on the one hand LC models and electro-static and magneto-static polarizability approaches [10–20] correctly deal with (3), but not with (1) and (2). On the other hand textbook electric point dipole scattering theories exist that correctly deal with (1) and (2), but not with magnetoelectric effects (3). Electric point dipole scattering theory is well known as a very effective means to describe random media, extraordinary transmission and plasmon particle arrays [27–29] and has been applied to metamaterial problems in cases without magnetoelectric effects [30, 31]. In this chapter we de-

rive an electrodynamic theory for general magnetoelectric scatterers that satisfies all three requirements. Essential ingredients for a consistent theory are generalized Onsager constraints [15, 32, 33] for the electrodynamic polarizability, and a magnetoelectric optical theorem first derived by Belov *et al.* [34]. While our theory sheds no light on the microscopic origin of the polarizability [35], a unique contribution is that we show how any quasi-static model [10–20] can be converted into an electrodynamically consistent scattering theory by a new tensorial method of radiation damping addition. Furthermore we predict how extinction measurements and measurements of radiation patterns (i.e., differential scattering cross section) can be used to quantify the polarizability tensor.

This chapter is structured in the following way: Firstly, in Section 3.2 we review in detail the general theory, taking into full account reciprocity, the optical theorem and radiation damping. In Section 3.3 we apply this theory to set up the polarizability of the archetypical metamaterial building block, a single SRR. In Section 3.4 we show which set of experiments can be used to retrieve the tensor polarizability $\boldsymbol{\alpha}$. We predict that magnetoelectric coupling directly implies circular dichroism in the extinction of single split rings, evidencing the utility of our theory to describe extrinsic chirality [8, 9, 36–41]. We will verify this in Chapter 5. Thirdly, we show in Section 3.5 that the theory can be simply applied to obtain quantitative scattering spectra of coupled systems. By way of example we examine the case of two coupled resonators in the stereodimer configuration reported by Liu *et al.* [18].

3.2 Magnetoelectric point scatterer

3.2.1 Dynamic polarizability

A paradigm in scattering theory is the point dipole scatterer [27–29, 42, 43] to model scattering by very small, but strongly scattering particles. In such a theory, each scatterer is approximated as an electric dipole with an electric dipole moment $\boldsymbol{p} = \alpha_{EE}\boldsymbol{E}$ that is proportional to the driving electric field $\boldsymbol{E}$. The proportionality constant is the polarizability α_{EE}. Generally, incident fields $\boldsymbol{E}$ and $\boldsymbol{H}$ induce a (complex) current distribution in an arbitrary scatterer. It is the express point of this chapter to assess what the scattering properties are of subwavelength scatterers with strong electric and magnetic dipole moments, as this represents the physics expected of metamaterial building blocks [17–20, 44]. Therefore we retain only electric and magnetic dipole terms, neglecting higher order multipoles. We derive a generalized point scattering theory for metamaterials that includes a magnetic dipole moment $\boldsymbol{m}$ on an equal footing with the electric dipole moment $\boldsymbol{p}$. By

definition, the electric and magnetic fields due to an induced $\boldsymbol{p}$ and $\boldsymbol{m}$ are equal to

$$\begin{pmatrix} \boldsymbol{E}_{\text{out}} \\ \boldsymbol{H}_{\text{out}} \end{pmatrix} = \boldsymbol{G}^0(\boldsymbol{r}, \boldsymbol{r}') \begin{pmatrix} \boldsymbol{p} \\ \boldsymbol{m} \end{pmatrix}, \tag{3.1}$$

with a dyadic Green tensor $\boldsymbol{G}^0$ that describes the field at position $\boldsymbol{r} = (x, y, z)$ due to a dipole at $\boldsymbol{r'} = (x', y', z')$. Throughout this chapter we suppress harmonic time dependence $e^{-i\omega t}$. We use a rationalized unit system that significantly simplifies all equations and is fully explained in Table 3.1. The 6×6 Green dyadic of free space can be divided in four 3×3 blocks

$$\boldsymbol{G}^0(\boldsymbol{r}, \boldsymbol{r}') = \begin{pmatrix} \boldsymbol{G}^0_{EE}(\boldsymbol{r}, \boldsymbol{r}') & \boldsymbol{G}^0_{EH}(\boldsymbol{r}, \boldsymbol{r}') \\ \boldsymbol{G}^0_{HE}(\boldsymbol{r}, \boldsymbol{r}') & \boldsymbol{G}^0_{HH}(\boldsymbol{r}, \boldsymbol{r}') \end{pmatrix} \tag{3.2}$$

The 3×3 diagonals correspond to the familiar known electric field Green dyadic [28, 29] and magnetic field Green dyadic of free space, which in our unit system (see Appendix) both equal

$$\boldsymbol{G}^0_{EE}(\boldsymbol{r}, \boldsymbol{r}') = \boldsymbol{G}^0_{HH}(\boldsymbol{r}, \boldsymbol{r}') = (\mathbb{I}k^2 + \nabla\nabla)\frac{e^{ik|\boldsymbol{r}-\boldsymbol{r}'|}}{|\boldsymbol{r}-\boldsymbol{r}'|}. \tag{3.3}$$

The off diagonal blocks correspond to the mixed dyadics that specify the electric field at $\boldsymbol{r}$ due to a magnetic dipole at $\boldsymbol{r'}$, and the magnetic field at $\boldsymbol{r}$ due to an electric dipole at $\boldsymbol{r'}$, respectively. Explicitly:

$$\begin{aligned} \boldsymbol{G}^0_{EH}(\boldsymbol{r}, \boldsymbol{r}') &= -\boldsymbol{G}^0_{HE}(\boldsymbol{r}, \boldsymbol{r}') \\ &= ik \begin{pmatrix} 0 & \partial_z & -\partial_y \\ -\partial_z & 0 & \partial_x \\ \partial_y & -\partial_x & 0 \end{pmatrix} \frac{e^{ik|\boldsymbol{r}-\boldsymbol{r}'|}}{|\boldsymbol{r}-\boldsymbol{r}'|}. \end{aligned} \tag{3.4}$$

The central starting point in this work, is that we assume that $\boldsymbol{p}$ and $\boldsymbol{m}$ can be induced by both the external electric and magnetic fields $\boldsymbol{E}$ and $\boldsymbol{H}$ according to the most general linear response

$$\begin{pmatrix} \boldsymbol{p} \\ \boldsymbol{m} \end{pmatrix} = \boldsymbol{\alpha} \begin{pmatrix} \boldsymbol{E}_{\text{in}} \\ \boldsymbol{H}_{\text{in}} \end{pmatrix}. \tag{3.5}$$

In Eq. (3.5), $\boldsymbol{\alpha}$ is a 6×6 polarizability tensor, which consists of four 3×3 blocks, each of which describes part of the dipole response to the electric or magnetic component of the incident light

$$\boldsymbol{\alpha} = \begin{pmatrix} \boldsymbol{\alpha}_{EE} & \boldsymbol{\alpha}_{EH} \\ \boldsymbol{\alpha}_{HE} & \boldsymbol{\alpha}_{HH} \end{pmatrix}. \tag{3.6}$$

This form and interpretation of the 6×6 polarizability in Eq. (3.6) is well known in the field of bi-isotropic and bi-anisotropic media [33]. In this field, many authors have analyzed the electro-static and magneto-static polarizability of Ω-particles, split ring resonators, bi-(an)isotropic spheres in the Rayleigh limit, and chiral scatterers like wire helices [10–15, 33]. In addition to the purely electric polarizability $\boldsymbol{\alpha}_{EE}$ known from plasmonics [45], the tensor also contains $\boldsymbol{\alpha}_{HH}$ that quantifies the magnetic dipole induced purely by a driving magnetic field. Finally, the off-diagonal blocks represent magnetoelectric coupling. The lower diagonal $\boldsymbol{\alpha}_{HE}$ quantifies the magnetic dipole induced by an incident electric field, and $\boldsymbol{\alpha}_{EH}$ the electric dipole induced by an incident magnetic field. Such magnetoelectric coupling is well known to occur in the constitutive tensors of metamaterials [46, 47]. However, the relative strength of magnetoelectric coupling in the polarizability, i.e., $\boldsymbol{\alpha}_{EH}$, and $\boldsymbol{\alpha}_{HE}$ have not been experimentally quantified for the archetypical building blocks of metamaterials, like split ring resonators.

An important distinction with earlier analyses of the 6×6 polarizability tensor in quasi-static models [10–15, 33], is that in any scattering theory $\boldsymbol{\alpha}$ is constrained by reciprocity and energy conservation. As we discuss below, energy conservation requires that the polarizability $\boldsymbol{\alpha}$ must depend on frequency ω and the velocity of light c. Hence, the polarizability that we discuss in this work is not a static polarizability, but is known as *dynamic* polarizability [27, 28] This dynamic polarizability is equivalent to the single scatterer t-matrix [28].

3.2.2 Onsager relation for dynamic polarizability

There are several constraints on $\boldsymbol{\alpha}$. In addition to any symmetry of the scatterer itself that may impose zeros in the polarizability tensor, these constraints are due to reciprocity and to energy conservation. We start by examining the constraints imposed by reciprocity. It is well known from the field of bi-anisotropic materials [33] that reciprocity imposes so-called Onsager constraints on the most general constitutive tensors relating $(\boldsymbol{D}, \boldsymbol{B})$ to $(\boldsymbol{E}, \boldsymbol{H})$. Several textbooks [15, 33] and García-García *et al.* [44] proposed that such Onsager constraints carry over directly to static polarizabilities. Chapter 7.1. in Ref. [15] lists Onsager relations for the static polarizability in the following form:

$$\boldsymbol{\alpha}_{EE} = \boldsymbol{\alpha}_{EE}^{T}, \quad \boldsymbol{\alpha}_{HH} = \boldsymbol{\alpha}_{HH}^{T}, \quad \text{and} \quad \boldsymbol{\alpha}_{EH} = -\boldsymbol{\alpha}_{HE}^{T}. \tag{3.7}$$

These textbooks [15, 33] derive the Onsager relations rigorously for constitutive tensors (ϵ, μ and cross terms) by solving the wave equation in homogeneous, bi-anisotropic space. To the best of our knowledge, the quoted Onsager relations for static polarizabilities are based on the assumption that Onsager relations derived for

effective medium tensors must hold also for microscopic constituent polarizabilities, as we could not find any independent proof in literature. Here we rigorously derive the Onsager relations Eq. (3.7) for the dynamic polarizability of electrodynamic magnetoelectric point scatterers, and thereby show that the general point dipoles proposed in this work can indeed be used as microscopic building blocks for an exact scattering theory that describes the formation of bi-anisotropic media from dense lattices of scatterers in the effective medium limit. Since the point scattering building blocks fulfill the Onsager constraints, they are indeed the natural building blocks to derive effective media constitutive tensors by homogenization that also satisfy the Onsager relations.

In this work we focus solely on scatterers made from reciprocal materials (typically gold and silver), as is commonly true for the metallic scatterers that constitute metamaterials. Since the materials that compose our scatterers are assumed to satisfy reciprocity microscopically, the polarizability tensor must also lead to a scattering theory that satisfies reciprocity. To derive reciprocity constraints on $\boldsymbol{\alpha}$, it is sufficient to examine the Green function in the presence of just one point scatterer at the origin. This Green function that quantifies the field at $\boldsymbol{r}_2$ due to a source at $\boldsymbol{r}_1$ in presence of a single scatterer at $\boldsymbol{r}_s$ can be written as [27, 28, 48]

$$\boldsymbol{G}(\boldsymbol{r}_1, \boldsymbol{r}_2) = \boldsymbol{G}^0(\boldsymbol{r}_1, \boldsymbol{r}_2) + \boldsymbol{G}^0(\boldsymbol{r}_2, \boldsymbol{r}_s)\boldsymbol{\alpha}\boldsymbol{G}^0(\boldsymbol{r}_s, \boldsymbol{r}_1), \tag{3.8}$$

Reciprocity requires for any Green function $\boldsymbol{G}$ (similarly split in four blocks) that

$$\begin{pmatrix} \boldsymbol{G}_{EE}(\boldsymbol{r}_2, \boldsymbol{r}_1) & \boldsymbol{G}_{EH}(\boldsymbol{r}_2, \boldsymbol{r}_1) \\ \boldsymbol{G}_{HE}(\boldsymbol{r}_2, \boldsymbol{r}_1) & \boldsymbol{G}_{HH}(\boldsymbol{r}_2, \boldsymbol{r}_1) \end{pmatrix} = \begin{pmatrix} \boldsymbol{G}_{EE}(\boldsymbol{r}_1, \boldsymbol{r}_2) & -\boldsymbol{G}_{EH}(\boldsymbol{r}_1, \boldsymbol{r}_2) \\ -\boldsymbol{G}_{HE}(\boldsymbol{r}_1, \boldsymbol{r}_2) & \boldsymbol{G}_{HH}(\boldsymbol{r}_1, \boldsymbol{r}_2) \end{pmatrix}^T \tag{3.9}$$

which is equivalent to noting that swapping source and detector leaves the detected field unchanged. An extra minus occurs for the off-diagonal terms, i.e., when swapping a magnetic (electric) detector with an electric (magnetic) source. It is easy to verify that Eq. (3.9) is indeed satisfied by the free space Green function $\boldsymbol{G}^0$.

Using this fact, we evaluate Eq. (3.9) for the Green function in Eq. (3.8) to find if reciprocity constrains $\boldsymbol{\alpha}$. Since reciprocity is clearly satisfied for the first term in Eq. (3.8), we now focus on the second term

$$\boldsymbol{G}^0(\boldsymbol{r}_2, \boldsymbol{r}_s)\boldsymbol{\alpha}\boldsymbol{G}^0(\boldsymbol{r}_s, \boldsymbol{r}_1) = \boldsymbol{G}^0(\boldsymbol{r}_1, \boldsymbol{r}_s)\boldsymbol{\alpha}\boldsymbol{G}^0(\boldsymbol{r}_s, \boldsymbol{r}_2). \tag{3.10}$$

Expanding the matrix products in Eq. (3.9) while making use of the reciprocity of the free Green function results in the Onsager relations for the dynamic polarizability that are listed in Eq. (3.7). These relations are identical in form to the Onsager relations for constitutive tensors [33], but are now derived on very different

grounds. Whereas for bi-anisotropic media, Onsager relations on constitutive tensors are derived by solving for the Green function of homogeneous bi-anisotropic space, our new proof for Onsager relations that constrain dynamic polarizabilities only uses reciprocity of the Green function of vacuum.

3.2.3 Tensorial magnetoelectric optical theorem

Energy conservation imposes an 'optical theorem' that constrains the dynamic polarizability such that (in absence of material absorption) extinction equals scattering. The optical theorem for scalar electric dipole scatterers has been amply discussed in literature, for instance in the work by Sipe and Van Kranendonk [49] on resonant dielectrics, as well as in various references dealing with multiple scattering theory of random media and plasmonics [27–29]. This same scalar optical theorem has also been applied in the context of metamaterials to scatterers with a magnetic response [30, 31] that is completely uncoupled from the electric response. Extension of the optical theorem to 6×6 tensorial scatterers, i.e., including magnetoelectric cross coupling, is not immediately trivial as one needs to re-evaluate the definition of extinction, and of the amount of power radiated into the far field. Such an extension to the general case is reported by Belov *et al.* in Ref. [34].

For completeness we summarize the derivation of this optical theorem reported by Belov *et al.* [34]. As in the scalar electric case [27–29, 49], the optical theorem is based on equating extinction to scattering. Here, extinction corresponds to the amount of work done per unit cycle by the incident field $\boldsymbol{E}_{\rm in}$ and $\boldsymbol{H}_{\rm in}$ to drive $\boldsymbol{p}$ and $\boldsymbol{m}$, which is equal to $W = \langle\langle \mathrm{Re}\boldsymbol{E}_{\rm in}\cdot\mathrm{Re}\frac{d\boldsymbol{p}}{dt} + \mathrm{Re}\boldsymbol{H}_{\rm in}\cdot\mathrm{Re}\frac{d\boldsymbol{m}}{dt}\rangle\rangle$. This evaluates to

$$W = \frac{2\pi}{Z}k\mathrm{Im}\left[\begin{pmatrix}\boldsymbol{E}_{\rm in} & \boldsymbol{H}_{\rm in}\end{pmatrix}^{*}\boldsymbol{\alpha}\begin{pmatrix}\boldsymbol{E}_{\rm in}\\ \boldsymbol{H}_{\rm in}\end{pmatrix}\right], \tag{3.11}$$

where $(\cdot)^*$ indicates complex conjugate. The work per cycle can also be converted into an extinction cross section by dividing out the incident intensity $|E|^2/(2Z)$ (where Z is the impedance of the surrounding medium)

$$\sigma_{\rm ext} = 2Z\frac{W}{|E|^2} \quad (\text{for scalar } \alpha: \quad \sigma_{\rm ext} = 4\pi k\mathrm{Im}\alpha).$$

The power per solid angle radiated by the induced dipoles in a direction specified by a unit vector $\hat{\boldsymbol{r}}$ is found by calculating the far-field Poynting vector from Eq. (3.1). It is composed of three terms.

$$\frac{dP}{d\Omega} = \frac{dP_p}{d\Omega} + \frac{dP_m}{d\Omega} + \frac{k^4}{2Z}\mathrm{Re}(\boldsymbol{p}\times\boldsymbol{m})\cdot\hat{\boldsymbol{r}}, \tag{3.12}$$

The first term in Eq. (3.12) represents the scattered radiation of just the electric dipole $\boldsymbol{p}$, which integrates to a total scattered power given by Larmor's formula

$P_p = \frac{4\pi}{3Z}k^4|\boldsymbol{p}|^2$. The second term in Eq. (3.12) represents the radiation pattern of just the magnetic dipole $\boldsymbol{m}$, again given by Larmor's formula. The third term, however, can completely change the radiation pattern, as it contains the interference between the fields of $\boldsymbol{p}$ and $\boldsymbol{m}$. Hence the relative phase between the induced $\boldsymbol{p}$ and $\boldsymbol{m}$ is important for the differential scattering cross section. To obtain the total scattered power, one should integrate Eq. (3.12) over all solid angle. The interference term integrates to 0, as it is an odd function of $\hat{\boldsymbol{r}}$. Therefore, despite the fact that interference makes radiation patterns of magnetoelectric scatterers non-trivial, Larmor's formula for the scattered power immediately generalizes to $P = \frac{4\pi}{3Z}k^4\left(|\boldsymbol{p}|^2 + |\boldsymbol{m}|^2\right)$. The optical theorem is obtained by equating scattered power P to the work W done by the incident field $(\boldsymbol{E}_{\text{in}}, \boldsymbol{H}_{\text{in}})$

$$\begin{aligned}\text{Im}\left[\begin{pmatrix} \boldsymbol{E}_{\text{in}} & \boldsymbol{H}_{\text{in}} \end{pmatrix}^* \boldsymbol{\alpha} \begin{pmatrix} \boldsymbol{E}_{\text{in}} \\ \boldsymbol{H}_{\text{in}} \end{pmatrix}\right] = \\ \frac{2}{3}k^3\left[\begin{pmatrix} \boldsymbol{E}_{\text{in}} & \boldsymbol{H}_{\text{in}} \end{pmatrix}^* \boldsymbol{\alpha}^{*T}\boldsymbol{\alpha} \begin{pmatrix} \boldsymbol{E}_{\text{in}} \\ \boldsymbol{H}_{\text{in}} \end{pmatrix}\right]\end{aligned} \tag{3.13}$$

The incident field can be eliminated by expanding $\text{Im}(.) = \frac{1}{2i}[(.) - (.)^*]$ to yield

$$\frac{1}{2i}\left[\boldsymbol{\alpha} - \boldsymbol{\alpha}^{*T}\right] = \frac{2}{3}k^3\boldsymbol{\alpha}^{*T}\boldsymbol{\alpha}. \tag{3.14}$$

This optical theorem clearly reduces to the well known scalar optical theorem $\text{Im}\alpha = 2/3k^3|\alpha|^2$ in case α is not a tensor, and can easily be converted in the Sipe-Van Kranendonk form

$$\frac{\boldsymbol{\alpha}^{-1} - (\boldsymbol{\alpha}^{*T})^{-1}}{2i} = \frac{2}{3}k^3\mathbb{I} \tag{3.15}$$

reported by Belov *et al.* [34], provided that $\boldsymbol{\alpha}$ is invertible.

3.2.4 Addition of radiation damping to general α tensor

The optical theorem (Eq. 3.14) in itself should be viewed as a condition that can be checked for any given polarizability tensor to verify if it leads to an energy conserving scattering theory. Given the large number of microscopic quasi-static models for metamaterial scatterers, it is unfortunate that the optical theorem in itself does not provide a recipe that specifies how to amend an electro-static polarizability to satisfy energy conservation. In this section we provide such a recipe. Such a method is well known for simple electric scatterers, where it is for instance known that an electro-static Rayleigh polarizability $\alpha_0 = 3V(\epsilon - 1)/(\epsilon + 2)$ for a small

sphere of dielectric constant ϵ that in itself violates the optical theorem [50], can be amended by 'addition of radiation damping'. Any electro-static scalar α_0 can be converted into a bona fide dynamic polarizability that satisfies the optical theorem by adding radiation damping [28, 29]

$$\frac{1}{\alpha} = \frac{1}{\alpha_0} - i\frac{2}{3}k^3. \tag{3.16}$$

Addition of radiation damping is key in any point dipole theory for, e.g., strongly interacting plasmon particles, and has been derived on independent grounds both from the optical theorem, and from size parameter expansions of dipolar scattering coefficients in Mie theory for spheroids [42, 51–54].

Here we derive a general method to add radiation damping to any electro- and magneto-static polarizability. This allows any polarizability that is derived from a circuit model to be generalized to be a building block in an electrodynamically consistent scattering theory. We start from Eq. (3.13), but now assume that $\boldsymbol{\alpha}$ can be diagonalized. This assumption is verified for split rings below. We call the eigenvectors $\boldsymbol{v}_i$, and denote the eigenvalues, which we will refer to as 'eigenpolarizabilities', with A_i. Expanding the incident field at the scatterer in the orthogonal eigenvectors

$$\begin{pmatrix} \boldsymbol{E}_{\text{in}} \\ \boldsymbol{H}_{\text{in}} \end{pmatrix} = \sum_i c_i \boldsymbol{v}_i, \tag{3.17}$$

and with $\boldsymbol{\alpha}\boldsymbol{v}_i = A_i\boldsymbol{v}_i$ and $\langle \boldsymbol{v}_i | \boldsymbol{v}_j \rangle = \delta_{ij}$, Eq. (3.13) reduces to

$$\frac{2}{3}k^3 \sum_{i=1}^{6} |c_i|^2 |A_i|^2 \geq \sum_{i=1}^{6} |c_i|^2 \text{Im} A_i, \tag{3.18}$$

with strict equality for lossless scatterers. Since this equation must be satisfied for any choice of incident wave (i.e., any combination of c_i), the generalized optical theorem for 6×6 polarizability tensors in Eq. (3.14) and Ref. [34] can also be expressed in terms of the eigenpolarizabilities as

$$\frac{2}{3}k^3 |A_i|^2 \geq \text{Im} A_i \qquad \forall i = 1 \ldots 6, \tag{3.19}$$

again with strict equality for lossless scatterers. Eq. (3.19) implies that the polarizability tensor represents an energy conserving scatterer, if and only if each of its 6 eigenpolarizabilities are chosen to satisfy the simple scalar optical theorem $\text{Im}\alpha = 2/3k^3|\alpha|^2$ derived for electric scatterers in Refs. [27–29, 49]. This new interpretation of the generalized optical theorem highlights the importance of two new quantities: the eigenpolarizabilities, and the corresponding eigenvectors of the

point scatterer polarizability. It is now evident, that we can simply apply the scalar recipe to each eigenpolarizability separately. A compact notation for this method is:

$$\boldsymbol{\alpha}^{-1} = \boldsymbol{\alpha}_0^{-1} - \frac{2}{3}k^3 i\mathbb{I}. \tag{3.20}$$

We note that this expression, which is identical to Eq. (3.16) upon replacement of $1/(\cdot)$ by matrix inversion, provides a unique relation to translate a magneto-/electro-static polarizability tensor $\boldsymbol{\alpha}_0$ derived from LC circuit theory, to the corresponding electrodynamic polarizability that satisfies the optical theorem. We can hence consistently assess how intuitive ideas based on a microscopic circuit model for electro-static and magneto-static dipoles lead to quantitative predictions for extinction, scattering, as well as resonance hybridization, diffraction and super/sub radiant damping in coupled systems, such as periodic systems, or arbitrary finite clusters.

In addition to its application to metamaterial scatterers discussed in the remainder of this chapter, the formalism derived here can be used also for many other problems of current interest. For instance, Alù and Engheta have recently resolved an interesting paradox first introduced by Kerker *et al.*, concerning the possibility of realizing zero-forward-scattering magneto-dielectric nanoparticles that appear to violate the optical theorem [55, 56]. Alú and Engheta used a size parameter expansion of the Mie coefficients of small magneto-dielectric spheres to show that magneto-dielectric spheres with electric and magnetic polarizabilities that are almost equal in magnitude but opposite in sign have a highly anisotropic scattering pattern, and violate the optical theorem unless one includes size expansion terms beyond the quasi-static limit. We note that all the essential physics of this problem can also be studied with ease using our formalism. It is easy to verify that a diagonal isotropic tensor with $\alpha_E = -\alpha_H$ indeed corresponds to a spherical scatterer with a highly anisotropic radiation pattern according to Eq. (3.12), with very small forward scattering. If radiation damping is added as in Eq. (3.20), the optical theorem is indeed satisfied, and forward scattering is low but not zero, in accordance with Ref. [55]. Firstly, this simple example shows that magnetoelectric point dipoles can have counterintuitive properties, such as highly anisotropic radiation patterns, very much unlike simple electric dipoles. Secondly, our formalism provides an easy analytical model that does not need a size parameter expansion of an exact solution, in order to study or design in how far paradoxes like the zero-forward scattering paradox extend to anisotropic particles that also have off diagonal, magnetoelectric elements.

3.3 Polarizability of split ring resonators

3.3.1 Symmetry

As an example of our general theory we consider the specific example of split ring resonators as studied in our experiments in Chapter 2. The quasi-static polarizability of split ring resonators was discussed in detail by Garcìa-Garcìa *et al.* [44], and also analyzed by Belov *et al.* [30], Shamonina *et al.* [11], Gorkunov *et al.* [13] and Marqués *et al.* [14]. We consider the LC resonance of an infinitely thin split ring in the xy plane, with split oriented along the x axis, as shown in Fig. 3.1(a). Such a split ring can only have an electric dipole moment along x and a magnetic dipole moment along z. As outlined in Ref. [44], the only nonzero tensor elements are α_{EE}^{xx}, α_{HH}^{zz} and the cross coupling terms α_{HE}^{zx} α_{EH}^{xz}.

$$\boldsymbol{\alpha}_{SRR} = \begin{pmatrix} \alpha_{EE}^{xx} & 0 & \dots & 0 & \alpha_{EH}^{xz} \\ 0 & & & & 0 \\ \vdots & & \ddots & & \vdots \\ 0 & & & & 0 \\ \alpha_{HE}^{zx} & 0 & \dots & 0 & \alpha_{HH}^{zz} \end{pmatrix}. \tag{3.21}$$

The symmetry constraints that set which elements of $\boldsymbol{\alpha}_{\mathrm{SRR}}$ are zero, are valid both for the electrodynamic and quasi-static polarizability of split rings.

3.3.2 Quasi-static RLC model

We now construct the electrodynamic polarizability by starting from a quasi-electro/magneto-static polarizability derived from a single resonant RLC equation of motion. Therefore we take a common resonant frequency dependence out of the tensor elements, writing

$$\boldsymbol{\alpha}_{\mathrm{SRR}}^{\mathrm{static}} = \alpha(\omega) \begin{pmatrix} \eta_E & 0 & \dots & 0 & i\eta_C \\ 0 & & & & 0 \\ \vdots & & \ddots & & \vdots \\ 0 & & & & 0 \\ -i\eta_C & 0 & \dots & 0 & \eta_H \end{pmatrix}, \tag{3.22}$$

where η_E, η_C and η_H are constant and $\alpha(\omega)$ is a Lorentzian prefactor

$$\alpha(\omega) = \frac{\omega_0^2 V}{\omega_0^2 - \omega^2 - i\omega\gamma}. \tag{3.23}$$

Here, ω_0 is the SRR resonance frequency $\omega_0 \approx \frac{1}{\sqrt{LC}}$, γ is the damping rate due to the Ohmic loss of gold and V is the physical particle volume. As in the plasmonic

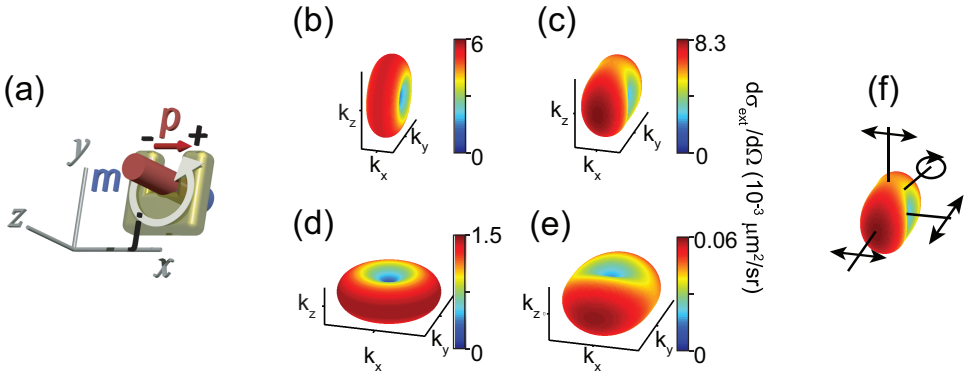

Figure 3.1: *Split ring radiation patterns corresponding to the polarizability tensor eigenvectors. Panel (a): (Sketch) A single split ring resonator can have an electric dipole moment $\boldsymbol{p}$ along the x-axis due to charging of the split. Circulating current j in the ring gives rise to a magnetic dipole moment $\boldsymbol{m}$ in the z-direction. Panels (b,c): Radiation patterns of the two eigenmodes of a split ring in the case of no off-diagonal magnetoelectric coupling ($\eta_E = 0.7, \eta_H = 0.3, \eta_C = 0$). The electric dipole moment oriented along the x-axis radiates most of its amplitude in the ky, kz plane, while the magnetic dipole oriented along the z-axis radiates mostly into the kx, ky plane. Panels (d,e): radiation patterns of the eigenvectors with magnetoelectric cross coupling ($\eta_C = 0.4$). Panel (f): indication of the polarization of the light radiated by the eigenvector with largest eigenvalue (panel (c)). Light is linearly polarized for wave vectors along the cartesian axes, but elliptically polarized in general. The direction of strongest circular dichroism in extinction and scattering is in the xz-plane.*

case, this approximation is coined 'quasi'-static, as it does contain frequency ω, but does not contain the velocity of light c. In this formulation, all the frequency dependence, and the units of $\boldsymbol{\alpha}_{\mathrm{SRR}}$ are contained in $\alpha(\omega)$. The parameters η_E, η_H and η_C are dimensionless. For a lossless split ring η_E, η_H and η_C are all real, and assumed positive on the basis of the anticipated in-phase response at very low frequencies [44]. The i multiplying η_C is needed to ensure lossless scattering (for $\gamma = 0$), and can be understood microscopically as reflecting the fact that any charge separation that is induced through a current lags the current by a quarter wave (and vice versa). In our model all Ohmic losses are introduced via γ.

3.3.3 Limit on magnetoelectric coupling

Having constructed a quasi-static polarizability in accordance with RLC circuit models proposed in earlier reports, we apply radiation damping according to Eq.

(3.20) to obtain a scatterer that has a correct energy balance [57]

$$\boldsymbol{\alpha}_{\mathrm{SRR}}^{-1} = (\boldsymbol{\alpha}_{\mathrm{SRR}}^{\mathrm{static}})^{-1} - \frac{2}{3}k^3\mathbb{I}. \tag{3.24}$$

So far we have not explicitly discussed absorption loss, except through the inclusion of the material damping constant γ in the quasi-static polarizability. Starting from a quasi-static polarizability with quasi-static eigenpolarizabilities A_i^{static}, the albedo for each eigenillumination $\boldsymbol{v}_i$ can be expressed as

$$a_i = \frac{1}{1 - \frac{3}{2k^3}\mathrm{Im}(\frac{1}{A_i^{\mathrm{static}}})}. \tag{3.25}$$

This albedo quantifies the fraction of energy absorbed in the scatterer compared to the total energy extinct by the scatterer when illuminated at eigenillumination. It follows that for any lossy scatterer the imaginary part of each eigenvalue A_i^{static} of the quasi-static polarizability tensor must be positive to ensure $0 \leq a \leq 1$. In the case of a tensorial $\boldsymbol{\alpha}$ with loss included as in Eq. (3.22) and Eq. (3.23), one needs to explicitly verify that each eigenvalue has positive imaginary part. The eigenvalues of Eq. (3.22) are $A_{\pm}^{\mathrm{static}} = \alpha(\omega)\lambda_{\pm}$ with $\lambda_{\pm} = 1/2(\eta_E + \eta_H \pm \sqrt{(\eta_E - \eta_H)^2 + 4\eta_C^2})$. Since $\mathrm{Im}\alpha(\omega) \geq 0$ and $\lambda_{\pm}$ are real, we find that both eigenvalues have positive imaginary part only if both λ_+ and λ_- are positive. Thus, loss sets an additional constraint on the polarizability tensor, and limits the magnetoelectric coupling to

$$|\eta_C| \leq \sqrt{\eta_E \eta_H}. \tag{3.26}$$

This result implies a very important limitation on magnetoelectric scatterers: it states that a magnetoelectric cross coupling (η_C) can only be generated if there is a sufficiently strong directly electric, and directly magnetic response. We note that this constraint is very similar to the constraint on the magnetoelectric cross coupling in constitutive tensors derived for homogeneous bi-anisotropic media in Ref. [33] that recently attracted attention in the framework of proposals for repulsive Casimir forces [58–61]. While our derivation was specific for split rings, we note that similar constraints hold for all magnetoelectric scatterers. In the presence of material loss, the magnetoelectric coupling terms are limited by the fact that all quasi-static eigenpolarizabilities must have positive imaginary part.

3.4 Predicted scattering properties of single split rings

In the remainder of the chapter we discuss some insights that the proposed magnetoelectric point scattering theory provides in how split rings scatter. In this section

we will consider the eigenmodes and the radiation patterns of a single SRR for $\boldsymbol{\alpha}$ given by Eq. (3.24). Next, we predict which set of experiments will provide full information on the elements of the polarizability tensor. We will show how measurable extinction cross sections can be translated back to retrieve SRR polarizabilities and magnetoelectric cross polarizabilities of a single SRR. Although the results we present are general, we use a specific set of parameters for all the figures presented in this chapter. These parameters are chosen to fit to the properties of split rings that are resonant at $\lambda = 1.5$ μm ($\omega_0/2\pi = 200$ THz) and that consist of 200 by 200 nm gold split rings with a thickness of 30 nm and a gap width of 90 nm. Thus we take $V = 200 \times 200 \times 30$ nm^3. We set the damping rate to be that of gold $\gamma = 1.25 \cdot 10^{14}$ s^{-1} as fitted to optical constants tabulated in in Ref. [62]. We use $\eta_E = 0.7$, $\eta_H = 0.3$ and $\eta_C = 0.4$. These parameters were chosen because (A) they reproduce quantitatively the extinction cross section under normal incidence along the z-axis measured by Husnik *et al.* [7], and (B) they fit well to our transmission data on arrays of different densities of split rings taken at normal incidence [17] and as a function of incidence angle [63]. The chosen values correspond to on-resonance polarizabilities $\alpha_{EE} = 4.6V$, $\alpha_{HH} = 2.1V$ and $\alpha_{EH} = 2.5V$, all well in excess of the physical SRR volume V as is typical for strong scatterers. Finally, we note that the calculated albedo fits well to the albedo $a = 0.5$ to 0.75 calculated by FDTD by Husnik *et al.* [7].

3.4.1 Radiation patterns and eigenvectors of the polarizability tensor

In Fig. 3.1, we consider the eigenstates of the split ring polarizability tensor presented in Eq. (3.24). We first assume that the cross coupling terms are absent, i.e., $\eta_C = 0$, in which case the polarizability tensor is diagonal, with eigenpolarizabilities $\alpha(\omega)\eta_E$ and $\alpha(\omega)\eta_H$. The corresponding orthogonal eigenmodes are $(p_x, m_z) = (1, 0)$ and $(p_x, m_z) = (0, 1)$. Fig. 3.1 (b) and (c) show radiation patterns of the two eigenmodes. Fig. 3.1(b) shows the radiation pattern of the purely electric eigenmode $(p_x, m_z) = (1, 0)$ and Fig. 3.1(c) shows the radiation pattern of the purely magnetic eigenmode $(p_x, m_z) = (0, 1)$. Note that both $\boldsymbol{p}_x$ and $\boldsymbol{m}_z$ radiate as simple dipoles with a $\sin^2\theta$ far field radiation pattern [64]. The two eigenmodes can be selectively excited by impinging with a plane wave incident along the z-axis with x-polarized E-field (electric eigenmode), or with a plane wave incident along the x-axis with y-polarization (z-polarized H-field, magnetic eigenmode). The extinction cross section of a single split ring at these two incidence conditions is set by $\sigma_{\text{ext}} = 4\pi k \text{Im}(\alpha_{EE})$ and $\sigma_{\text{ext}} = 4\pi k \text{Im}(\alpha_{HH})$.

Next, we consider extinction and eigenmodes for arbitrary values of the cross coupling. It is easy to see that the extinction cross section at the two special illumination conditions (incident along z, x-polarized, and incident along x, with

y-polarization, respectively) remain equal to $\sigma_{\text{ext}} = 4\pi k \text{Im}(\alpha_{EE})$ and $\sigma_{\text{ext}} = 4\pi k \text{Im}(\alpha_{HH})$. However, for nonzero η_C, these incidence conditions and polarizabilities do not correspond anymore to the eigenvalues and eigenvectors of the polarizability tensor, which now have mixed magnetoelectric character. In the extreme case of strongest magnetoelectric coupling ($\eta_C = \sqrt{\eta_E \eta_H}$), the eigenvectors reduce to $(p_x, m_z) = (1, i\sqrt{\eta_E/\eta_H})$ and $(p_x, m_z) = (1, -i\sqrt{\eta_H/\eta_E})$. The associated far-field radiation patterns of these eigenvectors correspond to coherent superpositions of the radiation pattern of an x-oriented electric dipole, and a z-oriented magnetic dipole, with a quarter wave phase difference. Fig. 3.1(d,e) show the on-resonance radiation pattern, assuming $\eta_E = 0.7$, $\eta_H = 0.3$ and η_C =0.4 . Note that these parameters are close to the limit of strongest possible magnetoelectric coupling. Fig. 3.1(d,e) reveal that the radiation pattern of each eigenmode is non-dipolar. Rather than a $\sin^2\theta$ donut-shaped pattern, an elongated radiation pattern occurs, with maximum extent in the y-direction. The polarization in the far field is linear for directions along the cartesian axis, but is generally elliptical.

3.4.2 Extinction cross sections to measure polarizability

Fig. 3.2 shows the extinction cross section predicted by our point scattering model of a single split ring for different incidence conditions. In Fig. 3.2(a), the incident wave vector is swept from the z-direction to the y-direction, while maintaining x-polarized light. For this set of incidence conditions the resulting extinction cross sections only depend on α_{EE} and α_{HH}, and are entirely independent of the off-diagonal coupling strength α_{EH}. The cross section increases from $\sigma_{\text{ext}} = 4\pi k \text{Im}\alpha_{EE}$ as the split ring is only driven by the incident E_x field when light is incident along z, to $\sigma_{\text{ext}} = 4\pi k(\text{Im}\alpha_{EE} + \text{Im}\alpha_{HH})$, as the split ring is driven by the incident E_x field plus the incident H_z field. When the wavevector is rotated to the the x-axis, the extinction cross section diminishes to $4\pi k \text{Im}\alpha_{HH}$, as the split ring is only driven by H_z. The chosen values $\eta_E = 0.7, \eta_H = 0.3$ and $\eta_C = 0.4$ that we also used for Fig. 3.1(d,e) yield extinction cross sections $\sigma_{\text{ext}} = 4\pi k \text{Im}\alpha_{EE} = 0.29\ \mu\text{m}^2$ and $\sigma_{\text{ext}} = 4\pi k \text{Im}\alpha_{HH} = 0.13\ \mu\text{m}^2$. The predicted $\sigma_{\text{ext}} = 4\pi k \text{Im}\alpha_{EE} = 0.29\ \mu\text{m}^2$ is consistent with the measurement ($\sigma_{\text{ext}} = 0.3\ \mu\text{m}^2$) reported by Husnik *et al.* [7]. It is important to note that measurements along cartesian incidence directions and with linear cartesian polarizations yield only the diagonal elements of the polarizability tensor. Indeed, the proposed measurements form a redundant set of measurements of α_{EE}, α_{HH}, and $(\alpha_{EE} + \alpha_{HH})$, but do not provide any insight into the magnetoelectric cross coupling in the electrodynamic polarizability tensor [65].

In order to measure the eigenpolarizabilities, it is necessary to selectively address the eigenvectors of the polarizability tensor. As noted above, the eigen-

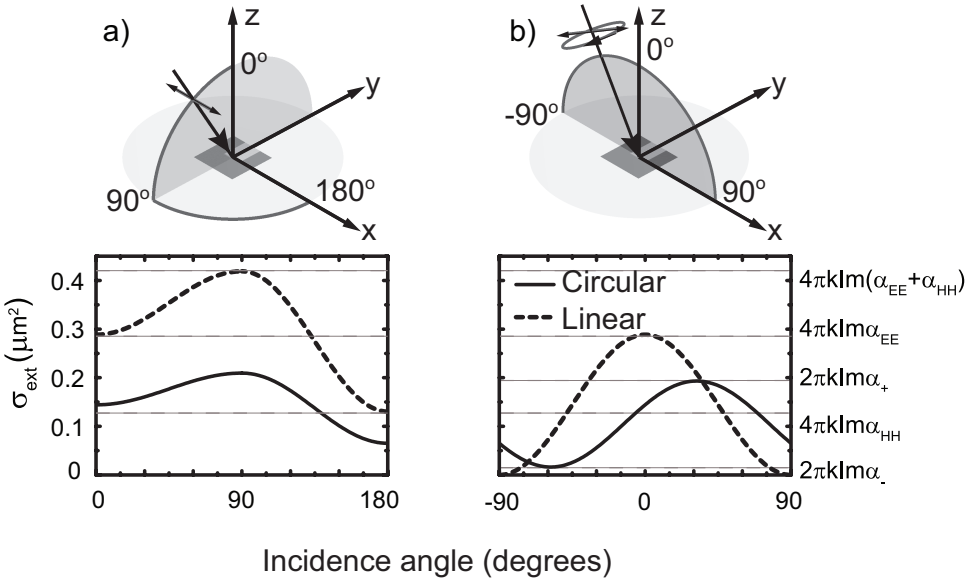

Figure 3.2: *We calculate extinction cross section $\sigma_{\rm ext}$ as a function of illumination angle and polarization. In panel (a), we sweep the incident wave vector over a total angular range of $180°$, over a trajectory (see panel (a), top) starting from the z-axis (labelled $0°$) to the $-y$-axis (labelled $90°$) , and then through the xy-plane to the x-axis (full $180°$). The dashed line represents $\sigma_{\rm ext}$ for linearly polarized incident illumination, where in (a) the polarization is kept in the xy plane as shown (i.e., polarization is along x for the first 90 degrees of the trajectory, rotating continuously to polarization vecor along y in the second part of the trajectory). The solid curve represents extinction for right handed circularly polarized illumination, which for the incidence conditions in (a) is half the extinction seen for linearly polarized light. For the trajectory of incident wave vectors in panel (a), $\sigma_{\rm ext}$ at normal incidence to the split ring is a measure for only α_{EE} as E_x is the only driving field. Increasing the angle to $90°$ both polarizations E_x and H_z excite the dipoles in the split ring, so $\sigma_{\rm ext}$ is a measure for the sum of the terms on the diagonal of the polarizability tensor $(\alpha_{EE} + \alpha_{HH})$. Changing the incidence condition to 180° removes the E_x component of the field, leaving only H_z of the incident light to drive the split ring. Hence $\sigma_{\rm ext}$ at 180° in panel (a) is a measure for purely α_{HH}. In panel (b) we sweep the incident wave vector from the $-x$-axis (labeled -90°) via the z-axis (again labeled 0°) to the $+x$-axis (labeled 90°). The color- and linetype coding is as in panel (a). However, now we constrain the linear polarization to have no y-component. Panel (b) $\sigma_{\rm ext}$ shows that as a function of the incident angle in the xz-plane for right-handed circular polarization minima and maxima in $\sigma_{\rm ext}$ occur as a function of angle, which are a measure for the eigenpolarizabilities α_- and α_+, respectively. Both sets of measurements in panel (a) and (b) together provide information on all the components of the polarizability tensor, α_{EE}, α_{HH}, and α_{EH}.*

vectors in the case of strong magnetoelectric coupling $\eta_C \approx \sqrt{\eta_E \eta_H}$ tend to $(p_x, m_z) = (1, i\sqrt{\eta_E/\eta_H})$ and $(1, -i\sqrt{\eta_H/\eta_E})$. These eigenvectors require simultaneous driving by E_x and H_z, with a quarter wave phase difference. We note that such fields can be generated by circularly polarized light with incident wave vector constrained to the xz-plane. Indeed, at maximally strong magnetoelectric coupling and $\eta_E = \eta_H$, circularly polarized light incident at 45° from the z-axis would selectively excite exactly one eigenmode. Therefore, we expect angle-resolved extinction measurements for oppositely handed circularly polarized beams to reveal the eigenpolarizabilities. Fig. 3.2(b) plots the extinction cross section for right handed circular polarization, as a function of angle of incidence in the z-plane, for illumination tuned to the LC resonance frequency. Naturally, at normal incidence the extinction is exactly half the extinction obtained for linear polarization, as a consequence of the fact that E_y does not interact with the split ring at all. Strikingly, the extinction cross section is predicted to behave asymmetrically as a function of incidence angle. The extinction increases when going to positive angle and decreases when going to negative angle. Changing handedness is equivalent to swapping positive and negative angles. A detailed analysis shows that the maximum in extinction corresponds to the largest eigenvalue of the polarizability tensor ($\sigma_{\text{ext}} = 2\pi k \text{Im}\alpha_+$), while the minimum in extinction corresponds to the smallest eigenvalue ($\sigma_{\text{ext}} = 2\pi k \text{Im}\alpha_-$). Therefore, circularly polarized measurements reveal the eigenvalues of the polarizability tensor. Combining such circularly polarized extinction measurements with the measurements under cartesian incidence in Fig. 3.2(a), therefore allows to extract all components of the polarizability tensor. In addition to the contrast in extinction, the angle at which the maximum circular dichroism occurs is a second, independent measure for the magnetoelectric coupling strength. The measurements in Fig. 3.2(a) and (b) together hence provide full, even redundant, information on η_E, η_H and η_C.

3.4.3 Pseudo-chirality

The results plotted in Fig. 3.2(b) show that magnetoelectric coupling in the 6×6 polarizability tensor directly implies pseudo-chirality. Pseudo-chirality refers to the objects ability to exhibit optical activity under specific conditions while the object itself is geometrically achiral. This concept will be discussed in Chapter 5. It is exhilarating that this interesting phenomenon first reported by [9, 39] for the transmission of arrays of scatterers is naturally present in the theory. However, while previous analysis of pseudo-chirality focused on transmission through periodic arrays, we predict that circular dichroism already appears in the extinction cross section of a single split ring, with a strength set by how close the magnetoelectric coupling strength is to its limit $\sqrt{\eta_E, \eta_H}$. Here we use the term 'circular dichroism

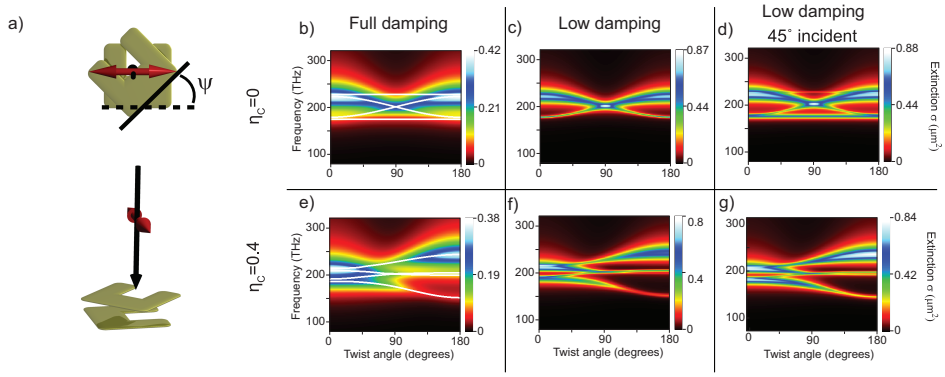

Figure 3.3: *Extinction cross sections σ_{ext} versus frequency and twist angle for a split ring stereodimer structure. Panel (a) shows the geometry (top view and side view) in which two split rings are vertically stacked. The upper split ring is rotated around the z-axis by the twist angle ψ. We calculate extinction for light impinging from the z-direction with polarization along x, i.e., along the base of the lower split ring in (b,c,e,f). In (d,g) we use 45° incidence in the xz-plane, so that the H-field of the excitation light directly couples also to the magnetic polarizability. Panels (b), (c) and (d) show extinction assuming no cross coupling term ($\eta_C = 0$) while (e), (f) and (g) show extinction assuming strong magnetoelectric coupling ($\eta_C = 0.4$). Panels (b) and (e) assume the damping rate of gold $\gamma = 1.25 \times 10^{14}\ s^{-1}$. To more clearly bring out the four mode structure, we reduce the damping ten-fold for the calculations in (c,d,f,g). There are four modes present in the system. White lines in (b,e) indicate the frequencies of the modes, as taken from the resonances in the low-damping case, i.e., the resonances in panels (d,g).*

in extinction' not to refer to differential absorption of left and right circular polarization as in usual circular dichroism, but to differential extinction. Indeed, the circular dichroism in extinction is a difference in extinction cross section for left and right circularly polarized light that occurs independently of whether there is material loss, as opposed to, e.g., asymmetric transmission phenomena through arrays, that are claimed to require dissipation [39]. For maximally magnetoelectrically coupled systems, the smallest eigenvalue is identically zero, implying that such a scatterer is transparent for one circular polarization, and achieves its strongest scattering for the opposite handedness. We expect that our 6×6 polarizability tensor can be successfully used to describe all sub-λ pseudo-chiral scatterers reported today [9, 36, 39, 66], as well as clusters and periodic arrays thereof, which we focus on in Chapter 5.

3.5 A coupled system: Split ring dimers

So far, this chapter has focused purely on the scattering properties of single magnetoelectric point scatterers. In the remainder of the chapter we illustrate that our method can be easily used to analyze multiple scattering by magnetoelectric scattering clusters. In order to calculate the response of a system of coupled magnetoelectric dipoles, we generalize the general self-consistent equation that describes scattering of clusters of electric dipoles $\boldsymbol{p}$ as reviewed in [29]. Assuming a system of N magnetoelectric point scatterers situated at positions $\boldsymbol{r}_1 \ldots \boldsymbol{r}_N$, the response upon illumination by an incident field $(\boldsymbol{E}_{\mathrm{in}}(\mathbf{r}), \boldsymbol{H}_{\mathrm{in}}(\mathbf{r}))$ is determined by a set of $6N$ self consistent equations for the induced dipole moments in each scatterer. The dipole moment induced in scatterer n with polarizability tensor $\boldsymbol{\alpha}_n$ is

$$\begin{pmatrix} \boldsymbol{p}_n \\ \boldsymbol{m}_n \end{pmatrix} = \boldsymbol{\alpha}_n \left[\begin{pmatrix} \boldsymbol{E}_{\mathrm{in}}(\mathbf{r}_n) \\ \boldsymbol{H}_{\mathrm{in}}(\mathbf{r}_n) \end{pmatrix} + \sum_{\substack{q=1\ldots N \\ q\neq n}} \boldsymbol{G}^0(\boldsymbol{r}_n, \boldsymbol{r}_q) \begin{pmatrix} \boldsymbol{p}_q \\ \boldsymbol{m}_q \end{pmatrix} \right] \tag{3.27}$$

Using this equation we can attempt to reinterpret recent measurements that evidence significant coupling in split rings in 2D arrays, as well as in oligomers [17–20]. Here we focus on the extinction of a dimer of split rings in socalled 'stereodimer'configuration, first studied by Liu *et al.* [18]. Fig. 3.3 shows such a 'stereodimer', consisting of two SRRs in vacuum ($V = 200 \times 200 \times 30$ nm^3, resonant at a wavelength around 1500 nm), both parallel to the xy plane, vertically stacked with a small height difference of 150 nm. The upper SRR is rotated by a twist angle ψ around the z-axis. On the basis of the report by Liu *et al.* [18], we expect two resonance peaks with an angle dependent splitting, which can be explained in an LC model as the summed effect of electric dipole-dipole coupling and magnetic dipole-dipole coupling.

We calculate the extinction versus twist angle and wavelength of an incident beam incident from the $+z$ direction, with x-polarization. This beam directly excites $\boldsymbol{p}_x$ in both rings, which also drive each other. We first analyze the experiment assuming that there is no magnetoelectric coupling term (setting η_C =0, although we keep η_E =0.7 and $\eta_H = 0.3$). As Fig. 3.3(b) shows, the extinction shows a single strong resonance that is blueshifted relative to the single SRR resonance at 220 THz. As a function of twist angle, this broad resonance redshifts to 200 THz at a twist of 90°, and shifts back to 220 THz at a twist of 180°. There is no sign of a second resonance, which might be hidden below the strong resonance. To bring out the second resonance more clearly, we reduce the loss in Fig. 3.3(b), to a 10 times lower value $\gamma = 1.25 \cdot 10^{13}$ s^{-1} for gold in Fig. (c) and (d). For this almost absorption-free system, Fig. 3.3(c) indeed shows two resonances in extinction. The

blue shifted resonance is now observed to cross with a narrow red shifted resonance. The crossing is symmetric around 90° and is consistent with the hybridization of an electric dipole fixed along x, with a second one above it twisted by an amount ψ. The two branches have a very different width and strength, consistent with the fact that a symmetric configuration of dipoles couples more strongly to external fields (blue shifted resonance), than an antisymmetric 'dark' configuration (red shifted resonance).

To verify whether the two resonances observed in Fig. 3.3(a) are all resonances in the system, we change the angle of incidence to 45° in the xz plane, so that the exciting field has an H_z component to drive the split rings, in addition to an E_x component. Fig. 3.3(d) shows that in this case four resonances occur in extinction. In addition to the two curved bands excited by E_x, there are also two non-dispersive bands with a twist independent splitting. Obviously, these bands are due to the coupling of two magnetic dipoles in symmetric (broad and intense band) and antisymmetric head-to-tail configuration. The existence of four instead of two modes is a new insight compared to LC circuit models [18, 21], but is logical in view of the fact that split rings have both a magnetic and an electric response, which are decoupled under the assumption $\eta_C = 0$.

Next we analyze the extinction in presence of magnetoelectric coupling, setting $\eta_C = 0.4$. Again, we first examine the extinction in presence of realistic loss ($\gamma = 1.25 \cdot 10^{14}$ s^{-1}) for gold in Fig. 3.3(e). As also predicted by FDTD simulations by Liu *et al.* [18], there appear to be two bands. The blue-shifted band is again very broad, but now has a frequency shift away from the single SRR resonance that is significantly larger for twist angle 180° than for 0°. These effects were explained by Liu *et al.* as due to an additive (subtractive) correction to the dominant electric hybridization at twist angle 180° (0°) that occurs due to magnetic dipole coupling. A surprise is that the diagram is not symmetric anymore around 90° twist as in the case of zero magnetic coupling. Instead, the extinction appears to show an anticrossing at twist angle 60°. These features were also predicted by FDTD simulations by Liu *et al.* [18]. However, the presence of an anticrossing at twist angle $\psi = 60^\circ$ could not be interpreted by Liu *et al.* [18] within an LC static circuit model, except by invoking higher order multipolar corrections. Here we see that a purely dipolar model may also explain all features of the experiment provided that magnetoelectric coupling is accounted for. While we do not claim that multipolar effects are not present in actual experiments, it is an important insight that split ring polarizabilities with magnetoelectric coupling terms may provide much richer physics then expected from quasi-static circuit theory. A main advantage of point dipole theory is that the underlying mode structure does not need to be recouped from FDTD simulations, but is easily resolved by repeating a calculation of extinction cross sections with low loss (as done in Fig. 3.3), or by analyzing the poles of

the coupling matrix in Eq. (3.27) that relates $(\boldsymbol{p}, \boldsymbol{m})$ to $(\boldsymbol{E}_{\mathrm{in}}, \boldsymbol{H}_{\mathrm{in}})$. The computational effort for N split rings is equivalent to diagonalizing or inverting a $6N \times 6N$ matrix.

To more clearly bring out all the resonances we artificially reduce the damping $\gamma = 1.25 \cdot 10^{13}$ s^{-1} to ten times less than the damping of gold, and plot the response of the system under normal incidence (f) and $45°$ incidence (g) in Fig. 3.3 (f,g). The anticrossing at twist angle $\psi = 60°$ appears to be due to the coupling of four modes, as opposed to the intuition from LC circuit theory that only two resonances anticross. The existence of four, rather than two modes in a split ring dimer appears surprising and is a second indication of the rich physics of magnetoelectric scatterers. Intuition from LC circuits is that although the subspace of driving fields is two dimensional (E_x and H_z), nonetheless only one mode per split ring exists. The usual reasoning in LC models is that the relation between electric and magnetic dipole moments is completely fixed and independent of driving, since the loop current and accumulated charge are directly related. Such a constraint is not general: in electrodynamic multipole expansions, magnetic polarizabilities are determined independently from the electric ones. The intuition from LC theory that there is only one mode per scatterer is only retrieved in our model right at the limit of strongest magnetoelectric coupling $\eta_C = \sqrt{\eta_E \eta_H}$, since in that case one eigenpolarizability is identically zero. We note that the values $\eta_E = 0.7, \eta_H = 0.3, \eta_C = 0.4$ used in this chapter (that we fitted to our angle-resolved transmission experiments on 200×200 nm Au split rings on glass) are close to the limit of strong magnetoelectric coupling. In Chapter 5 we focus on why physical scatterers are exactly at the limit of strongest magnetoelectric coupling $\eta_C = \sqrt{\eta_E \eta_H}$ and what the implications thereof are for optical activity of such scatterers.

3.6 Conclusion

In conclusion, we have developed a new multiple scattering theory by means of which we can calculate scattering and extinction for any magnetoelectric scatterer with known polarizability tensor, as well as for arbitrary finite clusters. As opposed to LC circuit models, our new model obeys energy conservation, contains all interference effects, and allows quantitative prediction of absolute cross sections, spectral linewidths and lineshapes. Since the electrodynamic polarizability tensor can be directly constructed from quasi-static circuit theory, we expect that our model is readily applicable to many current experiments using chiral and nonchiral metamaterial building blocks for which quasi-static models have been proposed.

Our model does not give any insight into whether the response of a given structure is truly dipolar or not. Also, our model does not provide any insight or quantitative predictions based on microscopic considerations for the magnitude of the

polarizability. For such microscopic considerations, based on, e.g., current density distributions derived from full wave simulations, we refer to [5, 22–26]. Rather, our model allows one to verify if specific data or microscopic calculations are consistent at all with point dipole interactions, allowing to verify or falsify common intuitive explanations in literature that have sofar been based on quasi-static considerations. Also, our model allows one to assess if a single polarizability tensor indeed can describe a range of different experiments with, e.g., split ring clusters, as should be expected from a consistent model. Finally, our model is the simplest electrodynamical model to consistently describe how metamaterials and photonic crystals are formed from magnetoelectric scatterers. A first step is to confirm the parameters used in this work for η_E, η_H and η_C by targeted experiments. While the value for η_E used in this work is consistent with the extinction cross section measured by Husnik *et al.* [7], we propose that the new insight that magnetoelectric coupling is far stronger than the magnetic polarizability be confirmed by off-normal circularly polarized extinction measurements as proposed in Section 3.4, which is the topic of Chapter 5.

The most important property of our theory is that a polarizability tensor validated for a single scatterer can readily be used to predict all quantitative scattering properties of composite lattices and antennas. We hence expect that new insights can be obtained in effective medium constants of metamaterial arrays. Our analytical model not only facilitates design, but will also for the first time allow to determine rigorously whether, even in the ideal case (no loss, no multipole corrections), metamaterial building blocks can give rise to a desired ϵ and μ, despite the large importance of electrodynamic corrections [17, 47, 67]. In addition to generating new insights for metamaterials, our theory also opens new design routes for gratings and antennas with unprecedented polarization properties. As an example, in this chapter we analyzed the four mode anticrossing due to magnetoelectric coupling in stereo-dimers. This analysis is easily extended to magnetoelectric Yagi-Uda antennas, diffractive gratings of chiral building blocks, and magneto-inductive waveguides that may provide new ways to control the propagation and emission of light [43, 68, 69].

Appendix: Unit system

Throughout this chapter we used units that significantly simplify notation throughout, as they maximize the interchangeability of electric and magnetic fields. Conversion to SI units is summarized in Table 3.1. For the conversion in Table 3.1, we use ϵ for the host dielectric constant, c for the velocity of light, and Z for the impedance of the background medium. In this unit system, a plane wave has $|\boldsymbol{E}|/|\boldsymbol{H}| = 1$, and intensity $I = |\boldsymbol{E}|^2/(2Z)$, since the Poynting vector is

Quantity	Symbol	Relation to SI
Electric field	$\boldsymbol{E}$	$\boldsymbol{E}_{\mathrm{SI}}$
Magnetic field	$\boldsymbol{H}$	$Z\boldsymbol{H}_{\mathrm{SI}}$
Electric dipole moment	$\boldsymbol{p}$	$\boldsymbol{p}_{\mathrm{SI}}/(4\pi\epsilon)$
Magnetic dipole moment	$\boldsymbol{m}$	$\boldsymbol{m}_{\mathrm{SI}}(Z/(4\pi))$
Electric-electric polarizability	$\boldsymbol{\alpha}_{EE}$	$\boldsymbol{\alpha}^{\mathrm{SI}}_{EE}/(4\pi\epsilon)$
Magnetic-magnetic polarizability	$\boldsymbol{\alpha}_{HH}$	$\boldsymbol{\alpha}^{\mathrm{SI}}_{HH}/(4\pi)$
Electric-magnetic polarizability	$\boldsymbol{\alpha}_{EH}$	$\boldsymbol{\alpha}^{\mathrm{SI}}_{EH}(c/(4\pi))$
Magnetic-electric polarizability	$\boldsymbol{\alpha}_{HE}$	$\boldsymbol{\alpha}^{\mathrm{SI}}_{HE}(Z/(4\pi))$
Electric-electric Green tensor	$\boldsymbol{G}_{EE}$	$4\pi\epsilon\boldsymbol{G}^{\mathrm{SI}}_{EE}$
Magnetic-magnetic Green tensor	$\boldsymbol{G}_{HH}$	$4\pi\boldsymbol{G}^{\mathrm{SI}}_{EE}$
Electric-electric Green tensor	$\boldsymbol{G}_{EH}$	$4\pi/Z\,\boldsymbol{G}^{\mathrm{SI}}_{EE}$
Magnetic-magnetic Green tensor	$\boldsymbol{G}_{HE}$	$4\pi/c\,\boldsymbol{G}^{\mathrm{SI}}_{EE}$

Table 3.1: *Conversion between SI units and the unit system used throughout this chapter.*

$\boldsymbol{S} = 1/(2Z)\mathrm{Re}(\boldsymbol{E}^* \times \boldsymbol{H})$. In these units, the cycle-averaged work done by an electric field $\boldsymbol{E}$ to drive an oscillating $\boldsymbol{p}$ equals $W = 2\pi k/Z\mathrm{Im}(\boldsymbol{E}\cdot\boldsymbol{p})$. The magnetic counterpart is $W = 2\pi k/Z\mathrm{Im}(\boldsymbol{H}\cdot\boldsymbol{m})$

Bibliography

[1] D. R. Smith, W. J. Padilla, D. C. Vier, S. C. Nemat-Nasser, and S. Schultz, Phys. Rev. Lett. **84**, 4184 (2000).

[2] W. J. Padilla, A. J. Taylor, C. Highstrete, M. Lee, and R. D. Averitt, Phys. Rev. Lett. **96**, 107401 (2006).

[3] S. Linden, C. Enkrich, M. Wegener, J. Zhou, T. Koschny, and C. M. Soukoulis, Science **306**, 1351 (2004).

[4] C. Enkrich, M. Wegener, S. Linden, S. Burger, L. Zschiedrich, F. Schmidt, J. F. Zhou, T. Koschny, and C. M. Soukoulis, Phys. Rev. Lett. **95**, 203901 (2005).

[5] C. Rockstuhl, F. Lederer, C. Etrich, T. Zentgraf, J. Kuhl, and H. Giessen, Opt. Expr. **14**, 8827 (2006).

[6] M. W. Klein, C. Enkrich, M. Wegener, C. M. Soukoulis, and S. Linden, Opt. Lett. **31**, 1259 (2006).

[7] M. Husnik, M. W. Klein, N. Feth, M. König, J. Niegemann, K. Busch, S. Linden and M. Wegener, Nature Photonics **2**, 614 (2008).

[8] J. K. Gansel, M. Thiel, M. S. Rill, M. Decker, K. Bade, V. Saile, G. von Freymann, S. Linden, and M. Wegener, Science **325**, 1513 (2009).

[9] E. Plum, J. Zhou, J. Dong, V. A. Fedotov, T. Koschny, C. M. Soukoulis, and N. I. Zheludev, Phys. Rev. B **79**, 035407 (2009).

[10] S. A. Tretyakov, A. H. Sihvola, A. A. Sochava, C. R. Simovski, J. of Electromag. Waves and Appl. **12**, 481 (1998).

[11] E. Shamonina, V. A. Kalinin, K. H. Ringhofer, and L. Solymar, J. Appl. Phys. **92**, 6252 (2002).

[12] M. G. Silveirinha, Phys. Rev. B **76**, 245117 (2007).

[13] M. Gorkunov, M. Lapine, E. Shamonina, K. H. Ringhofer, Eur. Phys. J. B **28**, 262 (2002).

[14] R. Marqués, F. Medina, R. Rafii-El-Idrissi, Phys. Rev. B **65**, 144440 (2002).

[15] A.N. Serdyukov, I.V. Semchenko, S.A. Tretyakov, A. Sihvola, *Electromagnetics of bi-anisotropic materials: Theory and applications*, Amsterdam: Gordon and Breach Science Publishers, 2001.

[16] J. D. Baena, L. Jelinek, R. Marqués, and M. Silveirinha, Phys. Rev. A **78**, 013842 (2008).

[17] I. Sersic, M. Frimmer, E. Verhagen and A. F. Koenderink, Phys. Rev. Lett. **103**, 213902 (2009).

[18] N. Liu, H. Liu, S. Zhu and H. Giessen, Nature Photonics **3**, 157 (2009).
[19] N. Feth, M. König, M. Husnik, K. Stannigel, J. Niegemann, K. Busch, M. Wegener, and S. Linden, Opt. Express **18**, 6545 (2010).
[20] H. Guo, N. Liu, L. Fu, T. P. Meyrath, T. Zentgraf, H. Schweizer, and H. Giessen, Opt. Expr. **15**, 12095 (2007).
[21] H. Liu, J. X. Cao, S. N. Zhu, N. Liu, R. Ameling and H. Giessen, Phys. Rev. B **81**, 241403(R) (2010).
[22] C. Rockstuhl, T. Zentgraf, E. Pshenay-Severin, J. Petschulat, A. Chipouline, J. Kuhl, T. Pertsch, H. Giessen, and F. Lederer, Opt. Express **15**, 8871 (2007).
[23] J. Zhou, Th. Koschny, and C. M Soukoulis, Opt. Express **15**, 17881 (2007).
[24] J. Petschulat, J. Yang, C. Menzel, C. Rockstuhl, A. Chipouline, P. Lalanne, A. Tennermann, F. Lederer, and T. Pertsch, Opt. Express **18**, 14454 (2010).
[25] T. D. Corrigan, P. W. Kolb, A. B. Sushkov, H. D. Drew, D. C. Schmadel, and R. J. Phaneuf, Opt. Expr. **16**, 19850 (2008).
[26] A. Pors, M. Willatzen, O. Albrektsen, and S. I. Bozhevolnyi, J. Opt. Soc. Am. B **27**, 1680 (2010).
[27] A. Lagendijk and B. A. van Tiggelen, Phys. Rep. **270**, 143 (1996).
[28] P. de Vries, D. V. van Coevorden and A. Lagendijk, Rev. Mod. Phys. **70**, 2 (1998).
[29] F. J. García de Abajo, Rev. Mod. Phys. **79**, 1267 (2007).
[30] P. A. Belov and C. R. Simovski, Phys. Rev. E **72**, 026615 (2005).
[31] J. Li and J. B. Pendry, eprint arxiv:cond-mat/0701332v1 (2007).
[32] L. D. Landau and E. M. Lifshitz, *Electrodynamics of Continuous Media*, Pergamon, Oxford (1960).
[33] I. V. Lindell, A. H. Sihvola, S. A. Tretyakov, and A. J. Viitanen, *Electromagnetic Waves in Chiral and Bi-Isotropic Media*, Artech House, Norwood MA (1994).
[34] P. A. Belov, S. I. Maslovski, K. R. Simovski, and S. A. Tretyakov, Techn. Phys. Lett. **29**, 718 (2003) (translated from Russian).
[35] R. Merlin, Proc. Nat. Acad. Sci. **106**, 1693 (2009).
[36] E. Plum, X.-X. Liu, V. A. Fedotov, Y. Chen, D. P. Tsai, and N. I. Zheludev, Phys. Rev. Lett. **102**, 113902 (2009).
[37] S. Zhang, Y.-S. Park, J. Li, X. Lu, W. Zhang, and X. Zhang, Phys. Rev. Lett. **102**, 023901 (2009).
[38] B. Wang, J. Zhou, T. Koschny, M. Kafesaki, and C. M. Soukoulis, J. Opt. A: Pure Appl. Opt **11**, 114003 (2009).
[39] E. Plum, V. A. Fedotov, and N. I. Zheludev, J. Opt. A: Pure Appl. Opt. **11**, 074009 (2009).
[40] M. Decker, M. W. Klein, M. Wegener, S. Linden, Opt. Lett. **32**, 856 (2007).
[41] M. Decker, R. Zhao, C. M. Soukoulis, S. Linden, M. Wegener, Opt. Lett. **35**,

1593 (2010).
[42] W. H. Weber and G. W. Ford, Phys. Rev. B. **70**, 125429 (2004).
[43] A. F. Koenderink and A. Polman, Phys. Rev. B **74**, 033402 (2006).
[44] J. Garcìa-Garcìa, F. Martìn, J. D. Baena, R. Marqués and L. Jelinek, J. Appl. Phys. **98**, 033103 (2005).
[45] C. F. Bohren and D. R. Huffman, *Absorption and Scattering of Light by Small Particles*, John Wiley & Sons, New York (1983).
[46] N. Katsarakis, T. Koschny, M. Kafesaki, E. N. Economou, and C. M. Soukoulis, Appl. Phys. Lett. **84**, 2943 (2004).
[47] C. Rockstuhl, T. Zentgraf, H. Guo, N. Liu, C. Etrich, I. Loa, K. Syassen, J. Kuhl, F. Lederer, and H. Giessen, Appl. Phys. B **84**, 219 (2006).
[48] Note that the above equation should strictly be written with $\boldsymbol{\alpha}$ replaced by the t-matrix, which is directly proportional to the dynamic polarizability $\boldsymbol{\alpha}$ for point scatterers [27].
[49] J. E. Sipe and J. Van Kranendonk, Phys. Rev. A **9**, 1806 (1974).
[50] H. C. van de Hulst, *Light Scattering by Small Particles* (Dover, New York, 1981).
[51] M. Meier and A. Wokaun, Opt. Lett. **8**, 581 (1983).
[52] K. T. Carron, W. Fluhr, A. Wokaun and H. W. Lehmann, J. Opt. Soc Am. B **3**, 420 (1986).
[53] K. L. Kelly, E. Coronado, L. L. Zhao and G. C. Schatz, J. Phys. Chem. B **107**, 668 (2003).
[54] A. Wokaun, J. P. Gordon and P. F. Liao, Phys. Rev. Lett. **48**, 1574 (1982).
[55] A. Alù and N. Engheta, J. Nanophot. **4**, 041590 (2010).
[56] M. Kerker, D. S. Wang, and C. L. Gilles, J. Opt. Soc. Am **73**, 765 (1983).
[57] The fact that $\boldsymbol{\alpha}_{\mathrm{SRR}}^{\mathrm{static}}$ is not invertible is easily overcome by noting that the radiation damping theorem should be applied only to its non-trivial subspace, e.g., by replacing the zeroes on the diagonal with infinitesimals.
[58] M. G. Silveirinha, Phys. Rev. B **82**, 085101 (2010).
[59] R. Zhao, J. Zhou, Th. Koschny, E. N. Economou, and C. M. Soukoulis, Phys. Rev. Lett. **103**, 103602 (2009).
[60] M. G. Silveirinha and S. I. Maslovski, Phys. Rev. Lett. **105**, 189301 (2010).
[61] R. Zhao, J. Zhou, Th. Koschny, E. N. Economou, and C. M. Soukoulis, Phys. Rev. Lett. **105**, 189302 (2010).
[62] P. B. Johnson and R. W. Christy, Phys. Rev. B **6**, 4370 (1972).
[63] A. Kwadrin, I. Sersic, and A. F. Koenderink, *in preparation*.
[64] J. D. Jackson, *Classical Electrodynamics (3rd ed.)*, John Wiley & Sons, New York (1999).
[65] Note that the diagonal elements of the electrodynamic polarizability do contain contributions due to off-diagonal elements in the electro-static tensor. The

radiation damping correction in Eq. (3.24) mixes η_C onto the diagonal.
[66] E. Plum, V. A. Fedotov, and N. I. Zheludev, Appl. Phys. Lett. **93**, 191911 (2008).
[67] C. Menzel, T. Paul, C. Rockstuhl, T. Pertsch, S. Tretyakov, and F. Lederer, Phys. Rev. B **81**, 035320 (2010).
[68] A. F. Koenderink, Nano Lett. **9**, 4228 (2009).
[69] H. Liu, D. A. Genov, D. M. Wu, Y. M. Liu, J. M. Steele, C. Sun, S. N. Zhu, and X. Zhang, Phys. Rev. Lett. **97**, 243902 (2006).

Chapter 4

Response of periodic arrays: experiment versus lattice sum dipole predictions

We implement the magnetoelectric polarizability tensor derived in the previous chapter as a building block for an electrodynamic model that describes the collective response of scatterers in periodic arrays. This model rigorously accounts for dipole coupling in arbitrary periodic lattices by generalizing Ewald lattice sums [1] to deal with the lattice response to both E and H. We reinterpret the transmission measurements in Chapter 2 on split ring arrays with different lattice spacings and explain the resonance shifts and width in terms of the lattice response. We find excellent correspondence between the data and the new theory.

4.1 Introduction

Scattering experiments on metamaterials are frequently done using periodic planar arrays of magnetoelectric scatterers with sub-diffraction lattice spacings. The chain of reasoning from measurement to effective media parameters generally leads from measured intensity reflection and transmission coefficients that are used to validate brute force FDTD simulations, which in turn lead to parameter retrieval on basis of calculated amplitude reflection and transmission coefficients [2–8]. Very recently several groups reported non-trivial coupling phenomena between split rings, depending on their density, their local lattice coordination and their relative orientation [9–16]. Essentially, the physics is determined by dipole-dipole coupling between split rings. Since split rings have cross sections far in excess of the lattice unit cell in typical metamaterials the coupling is very strong. Also, since split ring polarizabilities are comparable to the unitary limit, their coupling is essentially

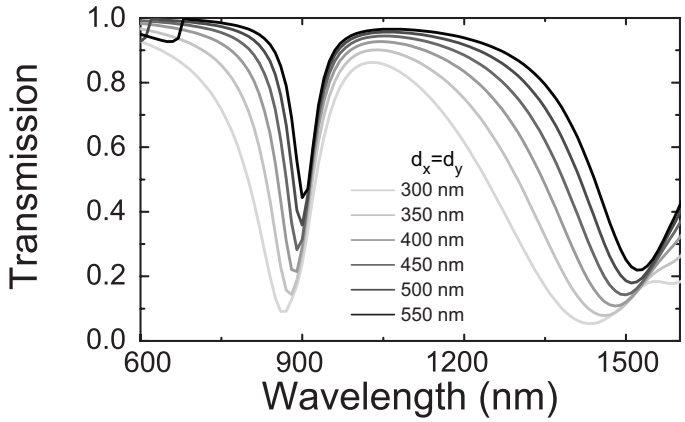

Figure 4.1: *Calculated transmission spectra for square split ring arrays with varying lattice spacing. The magnetic resonance at 1.5 μm blueshifts and broadens with increasing density.*

electrodynamic. In other words, coupling is not only via near field d^{-3} interactions, but also strongly via radiation into the far field. Indeed, lattice transmission data reported in Chapter 2 show strong superradiant broadening effects at high densities.

In Chapter 3, we have derived how the polarizability tensor $\boldsymbol{\alpha}$ can be approximated for a single SRR. In order to make successful predictions for measurements on arrays, apart from knowing the polarizability α of individual scatterers, one needs to understand the collective behavior of the lattice. Here, we expand our electrodynamic model of Chapter 3 to calculate reflection and transmission coefficients of magnetoelectric scatterers arranged in a periodic lattice. The collective response of lattices of scatterers with a scalar electric polarizability has previously been derived in [1]. Therefore, the aim of this chapter is not to derive a new theory, but to validate the electrodynamic picture of SRR response in arrays from the already existing theory, but with a tensorial $\boldsymbol{\alpha}$ [17]. Technicalities of the theory can be found in [1, 18, 19].

4.2 Lattice sum theory

In this work we consider the response to plane wave illumination of a 2D periodic lattice of point scatterers, which is defined by a set of lattice vectors $\mathbf{R}_{mn} = m\mathbf{a}_1 + n\mathbf{a}_2$, or equivalently a set of reciprocal lattice vectors $\mathbf{g}_{mn} = m\mathbf{b}_1 + n\mathbf{b}_2$, where m and n are integers, and $\mathbf{a}_{1,2}$ and $\mathbf{b}_{1,2}$ are real space and reciprocal space basis vectors, respectively. The response of a particle at position $\mathbf{R}_{mn}$ is selfconsistently

set by the incident field, plus the field of all other dipoles in the lattice according to

$$\begin{pmatrix} \boldsymbol{p}_{mn} \\ \boldsymbol{m}_{mn} \end{pmatrix} = \boldsymbol{\alpha} \left[\begin{pmatrix} \boldsymbol{E}_{\mathrm{in}}(\mathbf{R}_{mn}) \\ \boldsymbol{H}_{\mathrm{in}}(\mathbf{R}_{mn}) \end{pmatrix} + \sum_{m' \neq m, n' \neq n} \mathbf{G}^0(\mathbf{R}_{mn} - \mathbf{R}_{m'n'}) \begin{pmatrix} \boldsymbol{p}_{m'n'} \\ \boldsymbol{m}_{m'n'} \end{pmatrix} \right]. \tag{4.1}$$

For plane wave incidence with wave vector $\mathbf{k}_{||}$, using translation invariance of the lattice, we can substitute a Bloch wave form $(\boldsymbol{p}_{mn}, \boldsymbol{m}_{mn})^T = e^{i\mathbf{k}_{||}\cdot\mathbf{R}_{mn}}(\boldsymbol{p}_{00}, \boldsymbol{m}_{00})^T$ to obtain

$$\begin{pmatrix} \boldsymbol{p}_{00} \\ \boldsymbol{m}_{00} \end{pmatrix} = [\boldsymbol{\alpha}^{-1} - \mathcal{G}^{\neq}(\mathbf{k}_{||}, 0)]^{-1} \begin{pmatrix} \boldsymbol{E}_{\mathrm{in}}(\mathbf{R}_{00}) \\ \boldsymbol{H}_{\mathrm{in}}(\mathbf{R}_{00}) \end{pmatrix}. \tag{4.2}$$

Here, $\mathcal{G}^{\neq}(\mathbf{k}_{||}, 0)$ is a summation of the free space 6×6 dyadic Green function $\mathbf{G}^0$ over all positions on the 2D periodic real space lattice barring the origin

$$\mathcal{G}^{\neq}(\mathbf{k}_{||}, \mathbf{r}) = \sum_{m,n \neq 0} \mathbf{G}^0(\mathbf{R}_{mn} - \mathbf{r}) e^{i\mathbf{k}_{||}\cdot\mathbf{R}_{mn}}. \tag{4.3}$$

We will refer to the summation without exclusion of $m = n = 0$ as $\mathcal{G}(\mathbf{k}_{||}, \mathbf{r})$. The combination of Eq. (4.2) and (4.3) is the lattice sum formulation that has previously been reported in [1] for scalar Green function lattice sums where it was implemented using Ewald's technique [18]. We are not aware of any reported implementation of lattice sums for the 6×6 dyadic Green function $\mathbf{G}^0$. The key difficulty sits in the fact that the sum in Eq. (4.3) is poorly convergent since $\mathbf{G}^0$ decays only as $1/R$, whereas the number of terms with radius $R < R_{\mathrm{cutoff}}$ grows as R^2_{cutoff}. Ewald summation is the technique to deal with these difficulties. We refer to the excellent review by C. M. Linton [18] for an explanation of the technique for scalar Green functions. The dyadic case is obtained simply by pulling the derivatives in Eq. (3.3) and (3.4) that relate scalar and dyadic summand into the sum.

Once $\boldsymbol{p}$ and $\boldsymbol{m}$ are calculated via Ewald summation, we would like to find far field reflection and transmission. To find the reflected and transmitted waves, we note that for an observation point $\mathbf{r}$ in the far field, the Green function due to a source at $\mathbf{r}'$ can be written as

$$\mathbf{G}^0(\mathbf{r} - \mathbf{r}') = k^2 \frac{\exp(ik|\mathbf{r} - \mathbf{r}'|)}{|\mathbf{r} - \mathbf{r}'|} \mathbf{M} \tag{4.4}$$

where $\mathbf{M}$ is a dimensionless matrix with elements of order unity that only depends on the direction, not the length of $\mathbf{r} - \mathbf{r}'$. For a simple electric dipole, $\mathbf{M} \cdot \boldsymbol{p}$

quantifies $\hat{\boldsymbol{p}} - (\hat{\boldsymbol{p}} \cdot \hat{\boldsymbol{r}})\hat{\boldsymbol{r}}$, where $\hat{\boldsymbol{r}}$ is the unit vector along $(\mathbf{r} - \mathbf{R}_{m,n})$ the observation vector. Taking the scattered field intensity as the sum over all lattice points

$$\begin{pmatrix} \mathbf{E}(\mathbf{r}) \\ \mathbf{H}(\mathbf{r}) \end{pmatrix} = \sum_{n,m} k^2 \frac{\exp(ik|\mathbf{r} - \mathbf{R}_{nm}|)}{|\mathbf{r} - \mathbf{R}_{nm}|} e^{i\mathbf{k}_{||} \cdot \mathbf{R}_{n,m}} \mathbf{M}_{n,m} \begin{pmatrix} \mathbf{p}_{00} \\ \mathbf{m}_{00} \end{pmatrix} \tag{4.5}$$

we make the usual far-field expansion assumption that the orientational factor $\mathbf{M}$ does not vary with n, m and we substitute

$$\frac{\exp(ik|\mathbf{r} - \mathbf{R}_{m,n}|)}{|\mathbf{r} - \mathbf{r}'|} = \frac{i}{2\pi} \int d\mathbf{q} \frac{\exp(i\mathbf{q} \cdot (\mathbf{r}_{||} - \mathbf{R}_{m,n}) + k_z z)}{k_z} \tag{4.6}$$

with $k_z = \sqrt{k^2 - |\mathbf{q}|^2}$ and where integration is over parallel wave vector $\boldsymbol{q}$. Using the completeness relation of the lattice,

$$\sum_{m,n} e^{i\mathbf{k}_{||} \cdot \mathbf{R}_{mn}} = \frac{2\pi^2}{\mathcal{A}} \sum_{m,n} \delta(\mathbf{k}_{||} - \mathbf{g}_{mn}), \tag{4.7}$$

where $\mathcal{A}$ is the area of the unit cell, one might recast the summation to reciprocal space. As a consequence, one retrieves diffracted orders in the far field of the form

$$\begin{pmatrix} \mathbf{E}(\mathbf{r}) \\ \mathbf{H}(\mathbf{r}) \end{pmatrix} = \sum_{\mathbf{g}, |\mathbf{k}^{\mathbf{g}}| \leq k} \begin{pmatrix} \mathbf{E}^{\mathbf{g}} \\ \mathbf{H}^{\mathbf{g}} \end{pmatrix} e^{i\mathbf{k}^{\mathbf{g}} \cdot \mathbf{r}} \tag{4.8}$$

where the diffracted wave vectors are $\mathbf{k}^{\mathbf{g}} = (\mathbf{k}_{||} + \mathbf{g}, \pm\sqrt{k^2 - |\mathbf{k}_{||} + \mathbf{g}|^2}) = k(\cos\phi \sin\theta, \sin\phi \sin\theta, \cos\theta)$. The far fields associated with each order are

$$\begin{pmatrix} \mathbf{E}^{\mathbf{g}} \\ \mathbf{H}^{\mathbf{g}} \end{pmatrix} = \frac{2\pi i k}{\mathcal{A} \cos\theta} \mathbf{M}(\theta, \phi) \begin{pmatrix} \mathbf{p}_0 \\ \mathbf{m}_0 \end{pmatrix} \tag{4.9}$$

Where the orientation matrix $M(\theta, \phi)$ is the orientation dependent matrix from [20] (Chapter 15). Since these are only scattered fields, one still needs to add the incident field to obtain the zero-order transmitted beam. Dividing with the incident field, one obtains the transmission and reflection coefficients that are related via $t = 1 + r$. The transmission coefficient for x-polarized incidence and detection, for instance, is then simply given by

$$t_{xx} = 1 + \frac{2\pi i k}{\mathcal{A} \cos\theta} (\mathbf{M}(\theta, \phi)[\boldsymbol{\alpha}^{-1} - \mathcal{G}^{\neq}(\mathbf{k}_{||}, 0)]^{-1})_{xx}. \tag{4.10}$$

4.3 Results

We have calculated transmission for many sets of parameters for $\boldsymbol{\alpha}$, to test whether the lattice sum model can mimic the response measured for $200\times200\times30$ nm SRRs in square and rectangular arrays that we reported in Chapter 2. As an example, we show transmission for square lattices in Fig. 4.1, with the same lattice spacings used in Chapter 2. Fig. 4.1 shows two clear dips in the transmission spectra for all lattice spacings. The dip at $\lambda = 1.5$ μm is the previously discussed LC resonance, while the second dip at $\lambda = 900$ nm is a higher order resonance attributed to the plasmons excited along the bottom arm of the SRR [9]. Here, we have used $2\pi c/\omega_0 = 1.6$ μm, $\gamma = 8.3 \times 10^{13}$ s^{-1}, $\alpha_E = 3.6V$, $\alpha_H = 1.6V$ and $\alpha_C = 2.1V$ for the LC resonance [21]. To mimic the higher order resonance, we have inserted $2\pi c/\omega_1 = 0.96$ μm, $\alpha_E = 1V$, $\alpha_H = 0.5V$ and $\alpha_C = 0.4V$, where $V = 0.0012$ μm^3. We assume the lattice to be embedded in a medium with refractive index $n = 1.23$, i.e., the average of the air and glass index on either side of the SRRs. Fig. 4.1 shows that the lattice sum model can indeed qualitatively reproduce all salient features also observed in the experimental data. These features include a blue shift of the LC resonance with increasing density, as well as significant broadening. A shoulder appears on the red side of the LC resonance for the highest density. Such resonance splitting would be expected on basis of the fact that the LC resonance of split rings has two, not one eigenpolarizabilities. This edge is not evident in the data, and would require further study with a spectrometer that extends further into the IR. Finally, we note that the exact shape of the higher order resonance depends on the assumed surrounding refractive index: this resonance overlaps with a grating diffraction resonance into the glass, and not into the air. Fair account of this would require a model that can deal with the interface.

In order to determine which, if any, set of polarizability parameters best describe the data, we have performed transmission calculations for both rectangular and square lattices, for a large set of parameters α_E, α_H, and α_C. In this scan of parameter space, we have kept the resonance frequency and damping constant fixed, $2\pi c/\omega_0 = 1.6$ μm and $\gamma = 8.3 \times 10^{13}$ s^{-1}. Since our scatterers are found at an air-glass interface, we assume the lattice to be in a homogeneous medium of index $n = 1.23$. We extract both the center frequencies and the linewidth of the transmission resonance, and define the set of parameters α_E α_H, and α_C that best matches our data, as those that best fit center frequency and linewidth simultaneously. Fig. 4.2 shows center frequency and linewidth as measured in Chapter 2, together with the dependence associated with the set of parameters that best fit the data. We find that the data cannot be fitted reasonably at all with parameters outside the range $0.5V < \alpha_{E,H,C} < 3.9V$. Only within this range do our calculations reasonably reproduce the extinction cross section σ_{ext} reported by Husnik *et al.* [22].

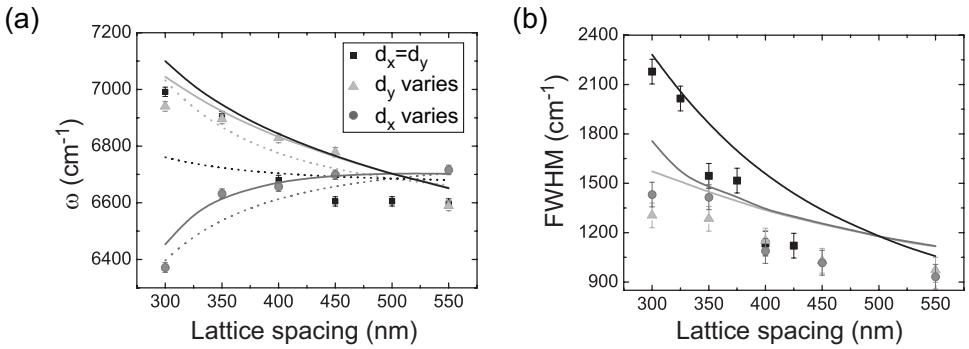

Figure 4.2: *(a) Frequency of the magnetic resonance versus lattice spacing. The frequency blueshifts when decreasing d_y whether $d_y = d_x$ (black squares) or not (light gray triangles, $d_x = 500$ nm), while it redshifts when decreasing d_x (dark gray circles, $d_y = 500$ nm). (b) Linewidth of the magnetic resonance versus lattice spacing (color coding as in (a)). Dashed lines in (a) are electrostatic theory, while full lines in (a) and (b) are electrodynamic theory based on lattice sums.*

The best fitting parameters are $\alpha_E = 3.6V$, $\alpha_H = 1.6V$, and $\alpha_C = 2.1V$ with estimated errors of $\Delta\alpha_E = \pm 0.8V$, $\Delta\alpha_H = \pm 0.5V$, and $\Delta\alpha_C = \pm 0.4V$. Parameter values in the order of particle volume V indicate that split rings are strong scatterers on resonance. Fig. 4.2(a) shows the density dependence of the center frequency predicted by the lattice sum model together with the values extracted from experiment, and with the static model represented as dashed lines. The lattice sum calculation notably reproduces the strong resonance redshift for side-side coupled split rings, as well as the strong blueshift for both square arrays and the top-bottom coupled structures. A notable difference with the quasistatic model in Chapter 2 is the strong blueshift with increasing density for the square lattice that is observed also in the data, but not so clearly in the static model. A calculation of resonance frequency and FWHM with zero magnetoelectric cross coupling is shown in Fig. 4.3 (a) and (b) (dotted line). The lattice sum calculation now shows a very different behavior for square lattices, as the blueshift now disappears. The normal incidence linearly polarized transmission spectra hence point to a significant magnetoelectric cross coupling term $\alpha_C \gg 0$ which we will quantify directly in experiments reported in Chapter 5. Fig. 4.2 (b) shows the FWHM versus lattice spacing as measured and calculated with the lattice sum model. Since the Ohmic damping does not depend on the coupling in the electrostatic model, the FWHM broadening with decreasing lattice spacing can only be explained by the radiation damping in an electrodynamic picture, which the lattice sum model fully takes into account.

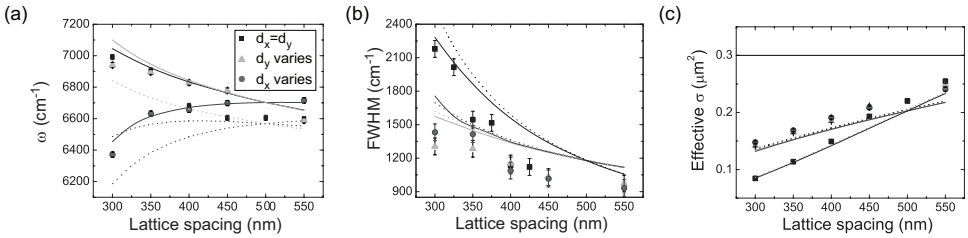

Figure 4.3: *(a), (b), and (c) are the comparison between the data and lattice sum calculations of the center frequency, resonance linewidth and the effective extinction cross section per split ring derived from on resonance transmission with and without the magnetoelectric cross coupling term. The full lines are lattice sum calculations with* $\alpha_E = 3.6V$*,* $\alpha_H = 1.6V$ *,* $\alpha_C = 2.1V$*, dotted lines with* $\alpha_E = 3.6V$*,* $\alpha_H = 1.6V$ *and without the cross coupling term. The black dashed line in (c) indicates the cross section of a single split ring (from [22]).*

So far we have used only the resonance shift and the resonance width, to quantify the polarizability tensor. An interesting question is if the *same* parameters also satisfactorily explain other parameters measurable in the experiment. In Fig. 4.3 (c) we plot the effective extinction cross section per split ring as a function of lattice spacing with magnetoelectric coupling (full line) and without (dotted line). While the trend of a marked increase of effective cross section with reduced density is evident, the effective extinction cross section is generally underestimated. We have found no set of α's that quite fits all three quantities center frequency, width and σ_{eff} simultaneously.The fact that no set of parameters can be found that simultaneously fit the center frequency, width, and cross section, is likely due to the asymmetric dielectric environment. The presence of an interface can significantly redistribute scattered light and can furthermore alter the local density of states (LDOS) of scatterers and thereby their extinction [23]. This is an interesting outlook with which we hope to further expand the lattice sum theory in the future.

4.4 Conclusion

We have shown how a point dipole lattice sum calculation can be implemented for point scatterers arranged in a 2D periodic array. We have extended the theory to apply to any magnetoelectric scatterer, and as such, explain the frequency shifts and superradiant broadening of the resonance peak with lattice spacing as seen in transmission measurements. We conclude that the polarizability of split rings is large compared to particle volume, quantifying the intuition that split rings are strong scatterers. Moreover our lattice sum calculation shows that the strong blueshift of the resonance for square lattices points at strong magnetoelectric cross coupling.

Indeed, it appears that driving with an electric field is more effective in setting up a large magnetic dipole moment, than direct magnetic driving. We pursue a more direct experimental method to quantify this observation in Chapter 5.

We envision that the model we have proposed in this chapter can be further improved and extended to deal with interesting questions. Firstly, the renormalization of the polarizability and the far field response due to the presence of an interface would be required to improve quantitative matching with data. Moreover, one can envision designing magnetoelectric gratings that have diffractive orders overlapping with the LC resonance. Such gratings could have interesting chiral properties, due to the inherent optical activity that the magnetoelectric coupling in split rings entail. Also, we envision that the theory can be extended to deal with finite stacks of 2D lattices. Such an approach would allow one to build a fully electrodynamically coupled model system to examine if and how ϵ and μ emerge as a metamaterial grows from a surface to a bulk material.

Finally, we compare our theory with a recent model by Decker *et al.* [24] that explains resonance frequency shifts and linewidth broadening from data obtained by oblique incidence excitations of SRR arrays by accounting for long-range interaction effects between the split rings. These are described in a Lagrangian static model modified to account for a finite size of the lattice via a phase lag between adjacent split rings in an array [24, 25]. Both theories explain the response of an array for both far-field and near-field interactions, and account for a phase gradient over the array (Bloch waveform, Eq. (4.2)). However, it is not obvious if the model by Decker *et al.* satisfies the optical theorem. Violation of energy conservation can fundamentally only be avoided if radiative damping is chosen self consistenly according to Eq. (3.20). Our theory rigorously satisfies the optical theorem by introducing the radiative damping term in the polarizability. Further radiative damping is contained in the rigorous electrodynamic lattice sums which explains the superradiant broadening of the resonance. In contrast, the theory of Decker *et al.* only takes into account radiation of electric dipole moments in the plane of the array, while magnetic dipole moments are neglected. This is an important point since in this thesis we show that magnetic dipole moments have significant polarizabilities comparable to the particle volume. A consistent model should equally account for radiation by electric and magnetic dipoles. For normal incidence experiments on nondiffractive samples, the far field radiated by magnetic dipoles cancels. However, our model can deal with any incidence angle, and any diffraction case.

Bibliography

[1] F. J. García de Abajo, Rev. Mod. Phys. **79**, 1267 (2007).

[2] D. R. Smith, W. J. Padilla, D. C. Vier, S. C. Nemat-Nasser, and S. Schultz, Phys. Rev. Lett. **84**, 4184 (2000).

[3] W. J. Padilla, A. J. Taylor, C. Highstrete, M. Lee, and R. D. Averitt, Phys. Rev. Lett. **96**, 107401 (2006).

[4] S. Linden, C. Enkrich, M. Wegener, J. Zhou, T. Koschny, and C. M. Soukoulis, Science **306**, 1351 (2004).

[5] D. R. Smith, S. Schultz, P. Markoš, and C. M. Soukoulis, Phys. Rev. B **65**, 195104 (2002).

[6] T. Koschny, P. Markoš, D. R. Smith, and C. M. Soukoulis, Phys. Rev. E **68**, 065602 (2003).

[7] N. Katsarakis, T. Koschny, M. Kafesaki, E. N. Economou, and C. M. Soukoulis, Appl. Phys. Lett. **84**, 2943 (2004).

[8] C. Rockstuhl, F. Lederer, C. Etrich, T. Zentgraf, J. Kuhl, and H. Giessen, Opt. Expr. **14**, 8827 (2006).

[9] C. Enkrich, M. Wegener, S. Linden, S. Burger, L. Zschiedrich, F. Schmidt, J. F. Zhou, T. Koschny, and C. M. Soukoulis, Phys. Rev. Lett. **95**, 203901 (2005).

[10] H. Guo, N. Liu, L. Fu, T. P. Meyrath, T. Zentgraf, H. Schweizer, and H. Giessen, Opt. Expr. **15**, 12095 (2007).

[11] M. G. Silveirinha, Phys. Rev. B **76**, 245117 (2007).

[12] M. G. Silveirinha and P. A. Belov, Phys. Rev. B. **77**, 233104 (2008).

[13] N. Liu, H. Liu, S. N. Zhu, and H. Giessen, Nature Photonics **3**, 157 (2009).

[14] I. Sersic, M. Frimmer, E. Verhagen and A. F. Koenderink, Phys. Rev. Lett. **103**, 213902 (2009).

[15] N. Feth, M. Knig, M. Husnik, K. Stannigel, J. Niegemann, K. Busch, M. Wegener, and S. Linden, Opt. Expr. **18**, 6545 (2010).

[16] D. A. Powell, K. Hannam, I. Shadrivov, and Y. S. Kivshar, Phys. Rev. B **83**, 235420 (2011).

[17] The implementation of the $6N \times 6N$ dyadic Ewald summation required for the lattice sum theory to describe the response of arrays of magnetoelectric scatterers has been done by A.F.K.

[18] C. M. Linton, SIAM Rev. **52**, 630 (2010).

[19] A. Kwadrin, I. Sersic, and A. F. Koenderink, *in preparation*.

[20] L. Novotny and B. Hecht, *Principles of Nano-Optics*, Cambridge University Press, UK (2006).

[21] Evidently, the polarizabilities $\alpha_{E,H,C}$ are complex quantities, since we are dealing with resonant scatterers that furthermore contain radiation damping. Quoted values for extracted parameters are for the absolute value on resonance throughout this chapter.

[22] M. Husnik, M. W. Klein, N. Feth, M. König, J. Niegemann, K. Busch, S. Linden and M. Wegener, Nature Photonics **2**, 614 (2008).

[23] B. C. Buchler, T. Kalkbrenner, C. Hettich, and V. Sandoghdar, Phys. Rev. Lett. **95**, 063003 (2005)).

[24] M. Decker, N. Feth, C. M. Soukoulis, S. Linden, and M. Wegener, Phys. Rev. B **84**, 085416 (2011).

[25] M. Decker, S. Burger, S. Linden, and M. Wegener, Phys. Rev. B **80**, 193102 (2009).

Chapter 5

Ubiquity of optical activity in planar metamaterial scatterers

Recently it was discovered that periodic lattices of metamaterial scatterers show optical activity, even if the scatterers or lattice show no 2D or 3D chirality, if the illumination breaks symmetry. In this chapter we demonstrate that such 'pseudo-chirality' is intrinsic to any single planar metamaterial scatterer and in fact has a well-defined value at a universal bound. We argue that in any circuit model, a nonzero electric and magnetic polarizability derived from a single resonance automatically imply strong bianisotropy, i.e., magnetoelectric cross polarizability at the universal bound set by energy conservation. We confirm our claim by extracting polarizability tensors and cross sections for handed excitation from transmission measurements on near-infrared split ring arrays, and electrodynamic simulations for diverse metamaterial scatterers.

5.1 Introduction

Many historical debates on how to describe the effective electrodynamic response of media composed of subwavelength building blocks currently acquire new relevance in nano-optics. On the one hand, the drive for arbitrary ϵ and μ is generated by the idea that light fields can be arbitrarily reshaped by conformal transformations, provided we can create arbitrary constitutive tensors [1–3]. On the other hand, a convergence with plasmonics has led to the realization that subwavelength scatterers mimic and even greatly enhance rich scattering phenomena known from molecular matter [4, 5]. For example, resonantly induced optical magnetism in 2D and 3D chiral metal nano-objects have been reported to result in giant circular birefringence, optical rotatory power, broadband optical activity, and circular

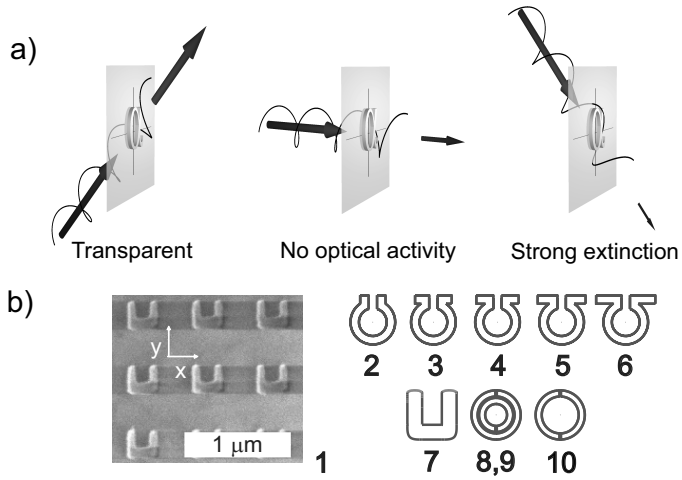

Figure 5.1: *(a) Any scatterer α with nonzero electric and magnetic polarizability shows oblique incidence optical activity, with transparency for one handedness of incident light at off-angles, and maximum extinction when the incident beam is rotated by 90°. At normal incidence, the scatterer shows no optical activity. (b) Common planar scatterers for which we verify optical activity and bianisotropy: (1) scanning electron micrograph of 230×230×30 nm Au SRRs. Structures (2)-(6): Ω particles of varying arm length. Structure (7) model for SRR in (1). Structure (8,9,10): double split ring and double gap ring [24].*

dichroism in frequency ranges from microwave, mid-IR, near IR to even visible frequencies [6–14]. The fact that strong optical activity is easily attained using chiral subwavelength scatterers is promising for many applications such as broadband optical components, as well as providing excellent candidates for achieving negative refraction [15], or repulsive Casimir forces [16]. Moreover, the promise of enhancing detection of molecular chirality via enhanced chirality in the excitation field, is expected to be of large importance for, e.g., discrimination of enantiomers in biology or medicine [17–20].

A question of essential importance is how to control the optical activity of a single building block, i.e., have independent control over the degree of magnetic response, electric response and magnetoelectric cross coupling or 'bianisotropy' whereby incident electric (magnetic) fields cause a magnetic (electric) material polarization in a single building block [21]. For instance, in attempts to reach negative indices, researchers soon found that the archetypical SRR has a magnetoelectric response that is undesirable, yet difficult to remove without also losing the magnetic response [22]. Completely opposite to the desire to remove this bianisotropy, it has also been realized that all applications exploiting optical activity benefit from

strong magnetoelectric coupling. Currently it is unclear if there exists any universal bound to which optical activity can be benchmarked, or conversely, if it is at all possible to avoid bianisotropy without also losing the magnetic response [23]. In this chapter, we discuss precisely such a universal bound for magnetoelectric coupling for single scatterers, disentangled from any lattice properties. We claim that Onsager's relations constrain optical activity to always be at this maximum bound for any dipole scatterer based on planar circuit designs, independent of geometrical chirality. Our claim is supported by measurements on SRRs at telecom wavelengths and rigorous full wave calculations [24] in which we retrieve cross sections and polarizabilities for various metamaterial scatterers (see Fig. 5.1(a,b)).

The central quantity in this chapter is the polarizability tensor that quantifies the magnetic response, electric response and magnetoelectric cross coupling (bianisotropy) intrinsic to a single metamaterial building block according to [21, 23]:

$$\begin{pmatrix} \mathbf{p} \\ \mathbf{m} \end{pmatrix} = \begin{pmatrix} \alpha_E & i\alpha_C \\ -i\alpha_C^T & \alpha_H \end{pmatrix} \begin{pmatrix} \mathbf{E} \\ \mathbf{H} \end{pmatrix} \tag{5.1}$$

For molecules, optical activity is due to weak cross coupling, i.e., a perturbative $\alpha_C E \approx 10^{-3}\alpha_E E$, while $\alpha_H \approx 0$. In contrast, the paradigm of metamaterials is that a single scatterer acquires a magnetic dipole moment $\boldsymbol{m}$ at least comparable to the electric moment $\boldsymbol{p}$, with α_E, α_H, and possibly α_C of the same order, which all derive from a single resonance [25].

5.2 Methods

In order to quantify the polarizability for the canonical SRR, we performed transmission measurements as well as full-wave calculations. For the experiments we fabricated Au SRRs resonant at telecom wavelengths arranged in square arrays on glass substrates by e-beam lithography [26, 27] and lift-off using ZEP520 resist. Fig. 5.1(b) shows a SEM image of a SRR array with 530 nm lattice spacing, which is so dilute that coupling between SRRs is small [27], as seen in Chapters 2 and 4, yet so dense that no grating diffraction occurs. Each SRR measures $230 \times 230 \times 30$ nm, with a gap between the arms that is 100 nm wide and 145 nm deep. We record transmission by illuminating the sample with a narrow band of frequencies at a time, selected from a supercontinuum laser (Fianium), using an acousto-optical tunable filter (Crystal Technologies) with a bandwidth of 1-2 nm [28]. The beam is chopped for lock-in detection on an InGaAs photodiode. We polarize the incident beam using a broadband quarter-wave plate, to provide circularly polarized excitation. We weakly focus the beam onto the sample (f=100 mm). Light is collected with a low NA collection lens (f=20 mm), and passed through a telescope and pinhole to ensure spatial selection from within a 200×200 μm^2 e-beam write field, as

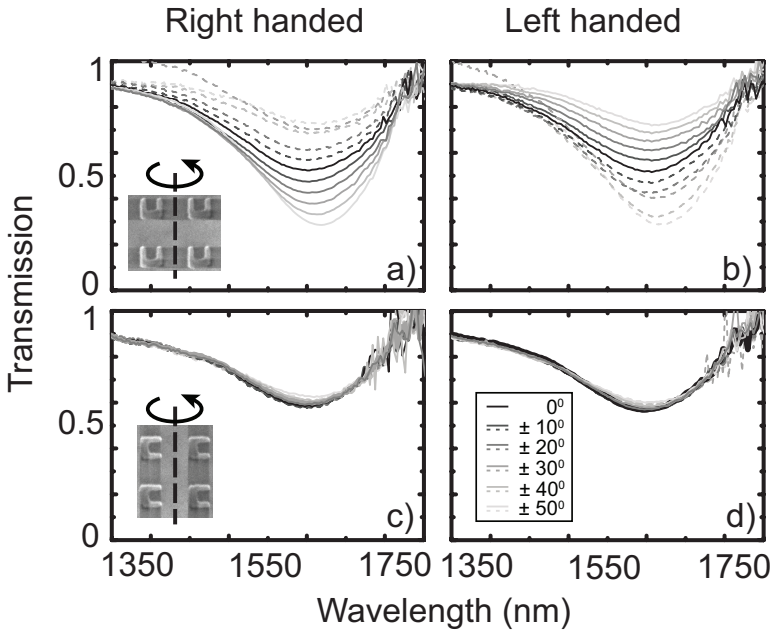

Figure 5.2: *Transmission spectra from a periodic square array of* 230×230 *nm split rings with* $d = 530$ *nm. The spectra were taken as a function of angle of incidence, where dashed curves denote negative angles, and solid curves positive angles with respect to the sample normal. (a,c) and (b,d) are transmission spectra shown for right- and left-handed circularly polarized illumination. Inset in (a) and (c) shows the the sample rotation axis for (a,b) and (c,d), respectively, taking the incident* k*-vector as pointing through the paper.*

monitored by an InGaAs camera. A motorized rotation stage allows transmission measurements versus incident angle relative to the sample normal.

Fig. 5.2 shows transmission versus wavelength for left and right handed circularly polarized incident light, for incidence angles from -50° to +50°. Fig. 5.2 (a) shows data when the angle is varied from normal incidence by rotating the SRRs around their mirror axis y. At normal incidence, the magnetic LC resonance is evident around 1600 nm wavelength as a minimum in transmission. As opposed to the deep minima reported in Chapter 2 for linear, x-polarized transmission (E along the gap) of dense arrays, the transmission dip is shallow since our lattice is dilute and the LC resonance is associated only with E_x and H_z, and completely transparent for E_y. As the incidence angle is moved away from the normal, the excitation also offers H_z as a driving field, a quarter wave out of phase with E_x. A very clear asymmetry around the normal develops. For right-handed light the transmission minimum becomes continuously shallower towards negative angles, and the sample is nearly transparent for $-50°$. In contrast, the transmission minimum significantly deepens from 28% to 75% when going to large positive angles. The asymmetric behavior with incidence angle is mirrored for opposite handedness (Fig. 5.2(b)), consistent with oblique incidence optical activity. For linear polarization the transmission is symmetric around normal incidence (not shown).

5.3 Results

The fact that optical activity is symmetry-allowed even for lattices containing 2D non-chiral objects aligned with the lattice symmetry, was already reported by Plum *et al.* [29], who coined this 'extrinsic 3D chirality', as well as Persoons *et al.* [4, 5] who previously observed a handedness in nonlinear experiments on surfaces of achiral molecules that were asymmetrically illuminated. In contrast to symmetry arguments that only distinguish between allowed and forbidden effects without quantifying the strength of optical activity, it is the express aim of this chapter to ascertain what the single element polarizability is that leads to the strong optical activity. We exclude the array structure factor as the cause of handed behavior [30], as the optical activity disappears when we rotate the SRRs by 90° in the sample plane (Fig. 5.2 (c) and (d)). We hence conclude that the single SRR polarizability must contain the strong 'pseudo-chiralilty' that is expressed as huge circular dichroism contrast in the extinction cross section, despite SRRs being neither 2D nor 3D chiral. Qualitatively, the LC description of a single SRR indeed contains optical activity under oblique incidence. Charge motion is set by $\dot{q} = (i\omega L + R + 1/i\omega C)^{-1}[i\omega\mu_0 A H_z + E_x t]$, where L is the inductance, C the capacitance, R the Ohmic resistance, t the capacitor plate gap and A the enclosed area. Full transparency despite the presence of suitable driving E_x along the gap

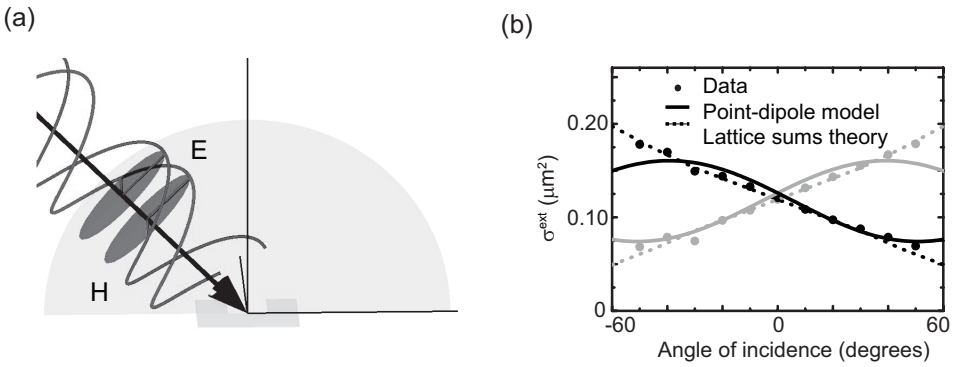

Figure 5.3: *(a) A schematic representing circularly polarized light under oblique incidence. The gray lines represent E_x and H_z fields that are quarter wave out of phase. (b) Circles: effective extinction per SRR from transmission data color coded for two handedness. Solid line: single scatterer extinction cross section expected in a dipole model. Dashed line: lattice sum calculation for a square array with pitch d=530 nm of magnetoelectric dipoles.*

and H_z through the split ring occurs when $i\omega\mu_0 AH_z = -E_x t$. Conversely, optimum driving of a SRR benefits from an opposite quarter wave phase difference between E_x and H_z so that $[i\omega\mu_0 AH_z + E_x t]$ has maximum magnitude. Circular polarization at oblique incidence provides the required quarter wave phase difference between E_x and H_z, as shown in Fig. 5.3 (a). Alternative to explanation via H_z and E_x, one could explain the handed behavior in Fig. 5.2 (a) and (b) as a response to $\partial_x E_y$, since rotation introduces a phase gradient between the two vertical arms that reverses with handedness, and with the sign of the rotation angle. In Fig. 5.2 (c) and (d), no such gradient exists, so no optical activity is observed. The explanations are equivalent since $H = \nabla \times E$.

We quantify the asymmetry in extinction from the data as in Chapter 2, i.e., by analyzing the effective extinction cross section per SRR defined as $\sigma = (1 - T_{R,L})d^2$, where d is the lattice spacing and $T_{R,L}$ is the minimum in transmission for right and left handed circularly polarized light [27]. Fig. 5.3 (b) shows that this *effective* extinction cross section varies between 0.07 and 0.16 μm^2 as the angle is swept from $\pm 50^\circ$ to $\mp 50^\circ$ (mirrored dependence for opposite handedness). For a single magnetoelectric dipole scatterer Ref. [23] and Chapter 3 predict that the extinction cross section generally depends on angle θ as

$$\sigma_{R,L}(\theta) = \sigma_- + (\sigma_+ - \sigma_-)[1 + \cos(2(\theta \pm \theta_0))]/2. \tag{5.2}$$

Measurements on a single object would provide the electrodynamic [31] α_E through the normal incidence extinction $\sigma_{R,L}(0) = 2\pi k \mathrm{Im}\alpha_E$, while the maximum and

minimum attained extinction $\sigma_\pm$ encode electrodynamic polarizability eigenvalues via $\sigma_\pm = \pi k \mathrm{Im}(\alpha_E + \alpha_H \pm \sqrt{(\alpha_E - \alpha_H)^2 + 4\alpha_C^2})$. Such a fit of the single object extinction to the measured effective extinction would provide $\alpha_E = 4.1V$, $\alpha_H = 3.6V$ and $\alpha_C = 1.4V$ expressed in units of the geometrical volume of the SRR ($V = 0.0012\ \mu\mathrm{m}^3$) [32]. Since the response of SRRs in arrays is modified by lattice coherences, as seen in Chapter 4, this parameter extraction using a single-object expression for extinction does not provide the most accurate estimate. To improve on the parameter extraction, we calculate lattice transmission by rigorous electrodynamic lattice sums involving all multiple-scattering interactions between SRRs [33]. Consistent with our data, the calculated transmission shows strong optical activity under oblique incidence. We extract $\alpha_E = 6.4V$, $\alpha_H = 0.9V$, $\alpha_C = 2.1V$ at λ=1600 nm from a comparison to data, highlighting that the response of SRR arrays is consistent with remarkably strong maximum magnetoelectric cross coupling.

In Chapter 3 [23] we analyzed how electrodynamic scatterers with arbitrary polarizabilities of the form in Eq. (5.1) scatter. In that work, we realized that once one applies the optical theorem to a planar scatterer (in-plane $\boldsymbol{p}$, out-of-plane $\boldsymbol{m}$), $\bar{\alpha}_C \leq \sqrt{\bar{\alpha}_E \bar{\alpha}_H}$ appears as the maximum value that $\bar{\alpha}_C$ – the cross coupling after taking a common resonant frequency factor out of Eq. (5.1) [25] – can possibly attain to avoid violation of energy conservation. Here we claim that *any* planar circuit-derived scatterer is necessarily exactly at this upper bound, i.e., at maximum cross coupling, at least in the static limit. To prove this assertion we analyze a generic model for the polarizability of a planar scatterer under two general assumptions: (1) a linear response and (2) that an electric and magnetic dipole response originate from the *same* equation of motion for charge q moving through the scatterer. Linear response implies $q = C_E(\omega)E + C_H(\omega)H$, where E (H) is in the plane (perpendicular to the plane) of the scatterer. Since $\boldsymbol{p}$ and $\boldsymbol{m}$ both derive from the same charge motion, $p_x = A_p q$ and $m_z = A_m \dot{q} = i\omega A_m(\omega) q$, where A_p and A_m are geometry-dependent constants. One now finds the electrostatic circuit polarizability as

$$\boldsymbol{\alpha}_0 = \begin{pmatrix} A_p C_E(\omega) & A_p C_H(\omega) \\ i\omega A_m C_E(\omega) & i\omega A_m C_H(\omega) \end{pmatrix}. \tag{5.3}$$

For reciprocal materials, Onsager's relations constrain α_E and α_H to be symmetric, as well as requiring $A_p C_H(\omega) = -i\omega A_m C_E(\omega)$. Taking out a common frequency factor $\mathcal{L}(\omega) \propto C_E(\omega)$ that describes the circuit resonance, one finds that α_0 always take the form [25]

$$\boldsymbol{\alpha}_0 = \mathcal{L}(\omega) \begin{pmatrix} \bar{\alpha}_E & i\omega\sqrt{\bar{\alpha}_E \bar{\alpha}_H} \\ -i\omega\sqrt{\bar{\alpha}_E \bar{\alpha}_H} & \omega^2 \bar{\alpha}_H \end{pmatrix}. \tag{5.4}$$

The surprise is that Onsager constraints *leave no freedom* to choose the off-diagonal

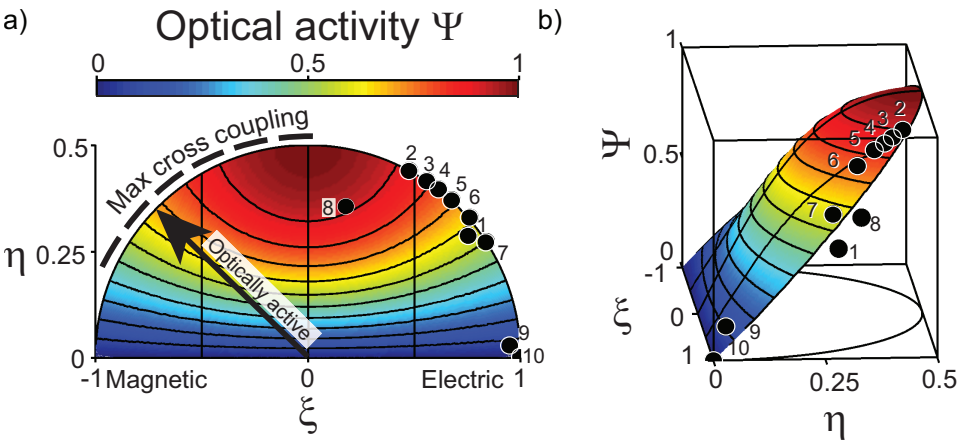

Figure 5.4: *Master diagrams summarizing optical activity and bi-anisotropy mapped as a function of* $\xi = (\alpha_E - \alpha_H)/((\alpha_E + \alpha_H)$ *and* $\eta = (\alpha_C)/((\alpha_E + \alpha_H)$*. All structures we tested (data-points, numbered as in Fig. 5.1(b)) are close to the locus of maximum cross coupling (ellipse), except (8). The color scale shows optical activity contrast* Ψ*, in the dipole approximation (color scale) and for tested structures (dots). Panel (b) is a 3D representation of (a).*

coupling $\bar{\alpha}_C$. Hence, any scatterer that can be described as a planar circuit element is cross coupled, with cross coupling $\bar{\alpha}_C = \sqrt{\bar{\alpha}_E \bar{\alpha}_H}$. Combining this finding with our result from Chapter 3 [23] we conclude that *any* planar circuit-derived scatterer is not just cross coupled, but that this coupling is at the maximum cross coupling limit derived in Chapter 3. Maximum cross coupling means one vanishing eigenpolarizability $\alpha_- = 0$, hence complete transparency of the scatterer for one handedness under oblique incidence, which means huge optical activity contrast.

Based on our experiment, we can now assess whether the strong cross coupling in real scatterers is indeed close to the predicted maximum. From the polarizability we extracted from the very strong circular polarization contrast in extinction observed for split rings in Fig. 5.3 we indeed find almost maximum cross coupling, since $\alpha_C \approx 0.88\sqrt{\alpha_E \alpha_H}$. Furthermore, we use full-wave simulations to examine the polarizability, and pseudo-chirality in extinction of many scatterers. We use 3D Surface Integral Equation (SIE) calculations [24], to obtain full-wave solutions for archetypical metamaterial scatterers including SRRs, Omega particles with straight legs of different length, double SRRs and double-gap rings as shown in Fig. 5.1(b). We use tabulated optical constants for gold [31], and the following dimensions: inner/outer radii in μm 0.74/1.19 (2-6), 1.6/2.5 and 2.7/3.6 (8), 2.7/3.6 (10), with a gap of 450 nm resp 200 nm for structures (2-6) resp. (10). For scatterers (2-6)

we increased the outer arm length from 0 to 900 nm. Scatterer thickness is 30 nm throughout. The respective resonance wavelength of the scatterers in μm are 1.600, 15.40, 16.06, 16.41, 16.80, 17.58, 1.544, 62.50, 23.25, and 16.50 for structures (1-10). Note that resonances (8,9) are two resonances in one structure. We calculate scattering cross sections and polarizability tensors independently from each other. To extract the polarizability, we excite the same scatterer with six linearly independent illumination conditions, obtained as counter-propagating linearly polarized beams set in (out of) phase to yield just electric (magnetic) Cartesian excitation. We project the calculated scattered E field evaluated on a spherical surface concentric with and in the near field around the scatterer on vector spherical harmonics to retrieve $\boldsymbol{p}$ and $\boldsymbol{m}$ [34]. As a consistency check on the polarizability retrieved by matrix inversion we verify that the Onsager constraints are satisfied, which are not a priori assumptions in the retrieval [35]. We summarize results for all scatterers in a 'master plot' that allows comparison independent of scatterer size. The scatterers are shown in Fig. 5.1 (b). As a first dimensionless variable we use $\xi = (\alpha_E - \alpha_H)/(\alpha_E + \alpha_H)$, which equals ± 1 for purely electric (magnetic) scatterers, and 0 for equal electric and magnetic polarizability. As a dimensionless second variable we take the normalized cross coupling $\eta = \alpha_C/(\alpha_E + \alpha_H)$. The locus of maximum cross coupling is the ellipse $\eta = \sqrt{1-\xi^2}/2$. Fig. 5.4 shows that most metamaterial scatterers we analyzed have ξ well away from 1, indicating significant magnetic polarizability. Furthermore all particles are essentially on the locus of maximum cross coupling, confirming our claim that bianisotropy is ubiquitous.

As third axis for the master plot we use a measure for optical activity in scattering. All scatterers we simulated show an angular dependence of the scattering cross section of the form in Eq. (5.2). The dimensionless parameter $\Psi = |\sigma_R - \sigma_L|/(\sigma_R + \sigma_L)$ evaluated at 45° incidence angle quantifies the maximum attained difference in extinction $|\sigma_R - \sigma_L|$ (maximal always at 45°) normalized to (twice) the angle-averaged extinction cross section $\sigma_+ + \sigma_-$. Fig. 5.4 shows Ψ versus ξ and η as predicted by point scattering theory. Evidently, optical activity is expected to be absent for zero cross coupling, and to increase monotonically as cross coupling increases. Very strong contrast in extinction per-building block is expected along most of the locus of maximum cross coupling, vanishing only for purely electric, and purely magnetic dipole scatterers ($\xi = \pm 1$). The full-wave simulations show that all the commonly used metamaterial scatterers exhibit strong optical activity in surprisingly good agreement with the dipole model given that the circuit approximation, and the neglect of multipoles and retardation in Eq. (5.4) are very coarse assumptions. Freedom to deviate significantly from the dipole model requires multiple overlapping resonances in a single scatterer. Indeed, the most noted deviations occur for the object (8,9) which has two hybridized resonances of

separate parts.

5.4 Conclusions

To conclude, we have shown that planar metamaterial scatterers that rely on a single resonance to generate a simultaneous electric and magnetic response are maximally bianisotropic and strongly optically active, whether they exhibit geometrical chirality or not. Earlier findings based on symmetry arguments proposed that extrinsic 3D chirality requires loss [29]. We find that optical activity is in fact ubiquitous for planar magnetoelectric scatterers, irrespective of absorption. The cancelation of optical activity for zero absorption noted by [29] does not occur in $\boldsymbol{\alpha}$ but occurs in special cases where observables are subject to additional symmetries, such as wave vector conservation in non-diffracting periodic systems. Our findings have important implications for controlling bianisotropy independently of ϵ and μ in metamaterials, since they imply that it is fundamentally impossible to independently control bianisotropy for single resonant objects. The only route to avoid bianisotropy in lattices of resonators is to use heterogeneous lattices that contain distinct, or multi-resonant elements (e.g., double-split rings in Fig. 5.4) to independently generate ϵ and μ, or to use lattices of effectively larger 'super-cells' with rotated copies of the same building block to cancel off-diagonal coupling. Of course, larger supercells jeopardize the metamaterial objective of creating non-diffractive arrays. Our results are promising for enhancing far-field or near-field chirality [19] in scattering applications where it is desired. In general, since maximum cross coupling is ubiquitous, optical activity is a very robust phenomenon that is easily extended to, e.g., finite clusters, random assemblies, or multi-element antennas. For instance, we predict that one can create chiral variants of the plasmon Yagi-Uda antenna to generate or selectively enhance circularly polarized single emitters. Enhanced chirality in the near field will promote discrimination between enantiomers on the single molecule level using the fact that chiral fluorophores have enantioselective absorption cross sections. Also, near-field chirality can result in enantioselective resonance shifts for non-fluorescent species [18–21].

Bibliography

[1] J. B. Pendry, D. Schurig, and D. R. Smith, Science **312**, 1780 (2006).

[2] U. Leonhardt, Science **312**, 1777 (2006).

[3] D. Schurig, J. J. Mock, B. J. Justice, S. A. Cummer, J. B. Pendry, A. F. Starr, and D. R. Smith, Science **314**, 977 (2006).

[4] T. Verbiest, M. Kauranen, Y. Van Rompaey, and A. Persoons, Phys. Rev. Lett. **77**, 1456 (1996).

[5] T. Verbiest, M. Kauranen, and A. Persoons, Phys. Rev. Lett. **82**, 3601 (1999).

[6] J. Zhou, J. Dong, B. Wang, T. Koschny, M. Kafesaki, and C. M. Soukoulis, Phys. Rev. B. **79**, 121104 (2009).

[7] Z. Li, R. Zhao, T. Koschny, M. Kafesaki, K. B. Alici, E. Colak, H. Caglayan, E. Ozbay, and C. M. Soukoulis, Appl. Phys. Lett. **97**, 081901 (2010).

[8] V. K. Valev, N. Srnisdorn, A. V. Silhanek, B. De Clercq, W. Gillijns, M. Ameloot, V. V. Moshchalkov, and T. Verbiest, Nano Lett. **9**, 3945 (2009).

[9] Y. Gorodetsky, N. Shitrit, I. Bretner, V. Kleiner, and E. Hasmanm, Nano Lett. **9**, 3016 (2009).

[10] A. Drezet, C. Genet, J.-Y. Laluet, and T. W. Ebbesen, Opt. Express **16**, 12559 (2008).

[11] S. Zhang, Y.-S. Park, J. Li, X. Lu, W. Zhang, and X. Zhang, Phys. Rev. Lett. **102**, 023901 (2009).

[12] M. Decker, R. Zhao, C. M. Soukoulis, S. Linden and M. Wegener, Opt. Lett. **35**, 1593 (2010).

[13] E. Plum, J. Zhou, J. Dong, V. A. Fedotov, T. Koschny, C. M. Soukoulis, and N. I. Zheludev, Phys. Rev. B. **79**, 035407 (2009).

[14] J. K. Gansel, M. Thiel, M. S. Rill, M. Decker, K. Bade, V. Saile, G. von Freymann, S. Linden, and M. Wegener, Science **325**, 1513 (2009).

[15] J. B. Pendry, Science **306** 1353 (2004).

[16] R. Zhao, J. Zhou, Th. Koschny, E. N. Economou and C. M. Soukoulis, Phys. Rev. Lett. **103**, 103602 (2009).

[17] Z. Fan and A. O. Govorov, Nano Lett. **10**, 2580 (2010).

[18] E. Hendry, T. Carpy, J. Johnston, M. Popland, R. V. Mikhaylovskiy, A. J. Lapthorn, S. M. Kelly, L. D. Barron, N. Gadegaard, and M. Kadodwala, Nature Nanotech. **5**, 783 (2010).

[19] Y. Tang and A. E. Cohen, Phys. Rev. Lett. **104**, 163901 (2010).

[20] Y. Tang and A. E. Cohen, Science **332**, 333 (2011).

[21] I. V. Lindell, A. H. Sihvola, S. A. Tretyakov, and A. J. Viitanen, *Electromagnetic Waves in Chiral and Bi Isotropic Media* (Artech House, Norwood, MA, 1994).

[22] N. Katsarakis, T. Koschny, M. Kafesaki, E. N. Economou, and C. M. Soukoulis, Appl. Phys. Lett. **84**, 2943 (2004).

[23] I. Sersic, C. Tuambilangana, T. Kampfrath and A. F. Koenderink, Phys. Rev. B **83**, 245102 (2011).

[24] A. M. Kern and O. J. F. Martin, J. Opt. Soc. Am. A **26**, 732 (2009).

[25] In the static limit α_E, α_H and α_C are real in $\mathcal{A}$ and Ohmic loss appears in $\mathcal{L}$ in Eq. (5.4). The addition of radiation damping sets α_E, α_H and α_C to be complex quantities even in absence of Ohmic damping [23].

[26] C. Enkrich, M. Wegener, S. Linden, S. Burger, L. Zschiedrich, F. Schmidt, J. F. Zhou, Th. Koschny, and C. M. Soukoulis, Phys. Rev. Lett. **95**, 203901 (2005).

[27] I. Sersic, M. Frimmer, E. Verhagen and A. F. Koenderink, Phys. Rev. Lett. **103**, 213902 (2009).

[28] I. Sersic, C. Tuambilangana and A. F. Koenderink, New J. Phys. **13**, 083019 (2011).

[29] E. Plum, V. A. Fedotov, and N. I. Zheludev, J. Opt. **13**, 024006 (2011).

[30] B. Gompf, J. Braun, T. Weiss, H. Giessen, U. Hübner and M. Dressel, Phys. Rev. Lett. **106**, 185501 (2011).

[31] We define a dynamic α by adding radiation damping $\mathrm{inv}(\alpha) = \mathrm{inv}(\alpha_0) - i(2/3)k^3\mathbb{I}$ to a static α_0 [23] with Lorentzian resonance $\mathcal{L}(\omega)$ centered at 1600 nm, and with damping rate of gold $\gamma = 1.25{\cdot}10^{14}s^{-1}$ from *Handbook of Optical Constants of Solids*, edited by E. D. Palik (Adacemic, Orlando, FL, 1985).

[32] Evidently, the polarizabilities $\alpha_{E,H,C}$ are complex quantities, since we are dealing with resonant scatterers that furthermore contain radiation damping. Quoted values for extracted parameters are for the absolute value on resonance throughout this chapter.

[33] F. J. García de Abajo, Rev. Mod. Phys. **79**, 1267 (2007).

[34] S. Mühlig, C. Menzel, C. Rockstuhl, and F. Lederer, Metamaterials **5**, 64 (2011).

[35] Implementing the Surface Integral Equation method was part of the work performed by Felipe Bernal Arango in the group Resonant Nanophotonics.

Chapter 6

Fourier microscopy of single plasmonic scatterers

We report an experimental technique for quantifying the angular distribution of light scattered by single plasmonic and metamaterial nanoscatterers, based on Fourier microscopy in a dark field confocal set up. This set up is a necessary tool for quantifying the scattering properties of single plasmonic and metamaterial building blocks, as well as small coupled clusters of such building blocks, which are expected to be the main ingredients of nano-antennas, light harvesting structures and transformation optics. We present a set of measurements on Au nanowires of different lengths and show how the radiation pattern of single Au nanowires evolve with wire length and as a function of driving polarization and wave vector.

6.1 Introduction

In order to build functional devices and materials from plasmonic and metamaterial scatterers, it is important to quantify how single building blocks scatter into the far field [1–6]. Such a quantification requires to not only determine the magnitude of their scattering, absorption and extinction cross section [3], but also to measure the distribution of light scattered into each direction [7, 8]. Measurements of angular distributions of light are highly challenging as signal levels from single nano-objects are low. Therefore, one often resorts to studying arrays of identical nano-objects. However, in scattering experiments on arrays one typically faces the problem that the radiation patterns of collections of scatterers are dominated by grating diffraction orders (periodic arrays), or speckle (random arrays). Separating this 'structure factor' from the angle-dependent radiation pattern of single

objects in such measurements is challenging since it is difficult to create a featureless structure factor. Recently, Fourier microscopy, or 'backaperture imaging', has been utilized by several groups as a method to measure angle-dependent radiation patterns. This method is based on collecting the light radiated by a single nanostructure using a standard high NA objective, and the realization that the objective back aperture contains k-space information of the electromagnetic field. Fourier microscopy was first applied to measure the radiation pattern of single molecule emitters, thereby allowing to determine their orientation [9, 10]. This method was also used recently [7, 11] to measure the directivity of emission for molecules coupled to a Yagi-Uda antenna and plasmon nano-apertures.

Surprisingly, the application of Fourier microscopy to scattering experiments is much less widespread [12–15]. For the geometry of metal particles on transparent substrates that is possibly of biggest interest in the fields of plasmonics and metamaterials, Fourier microscopy is most difficult to implement due to issues with background light. The only implementation that we are aware of [16] is limited to a very small subset of collection angles, namely only those angles above the total internal reflection angle in glass. Shegai *et al.* [8] have applied back aperture imaging to study radiation from the endpoints of nanowires. However, in their work light can only be collected from parts of a bigger structure, as the focused illumination applied to one part of a structure to excite it needs to be removed by spatial filtering. So far, however, the possibility of recording angle resolved scattering data over a full objective NA for single nano-objects on simple transparent substrates has not been reported. In this chapter we present an optical set up that can record radiation patterns for such subwavelength objects upon excitation with a well defined incident wave vector and polarization. In this way, it is possible to for the first time quantify how, e.g., single elements in plasmon antennas and metamaterials scatter. We present a set of measurements on radiation patterns of Au nanowires of different lengths. We demonstrate that while ultrashort Au nanobars radiate as a single point dipole, longer single nanowires can be understood as a collective oscillation of a line array of dipoles.

6.2 Experimental setup

Our homebuilt experimental set up is sketched in Fig. 6.1 (a). A basic design constraint that we impose is that the driving field has a well defined wave vector and polarization. Therefore, we opt for an input beam with a large focus, i.e. 30 μm spot size, that has a relative wave vector spread $|\mathbf{\Delta k}|/|\mathbf{k}| \leq 0.02$. Since any typical plasmonic scatterer has a cross section that is at most 10 times its geometrical cross section (0.1 μm^2), just 10^{-4} of the incident power is scattered in total per object. In a Fourier microscope this is not all collected by a single detector ele-

ment (as in an imaging microscope), but is spread over a detector array with 10^4 channels. Hence, each angular detection channels receives only about one photon per 10^8 incident photons, making a very bright source and excellent background suppression in the set up a necessity. Therefore, we have used a supercontinuum light source (Fianium), which has a spectrum in the range from 450 nm to 1750 nm, in combination with an acousto-optical tunable filter (AOTF) for frequency selection. The combination of Fianium and AOTF provides at least 0.1 mW in a 5 nm bandpass windows centered at any wavelength in the visible or near-infrared. Since scattering does not differ in frequency from the input beam, as in fluorescence experiments, it is not possible to differentiate the signal from the background signal by means of frequency filtering. Therefore, we have utilized dark field microscopy in total internal reflection (TIR) mode to excite our structures.

The samples are placed on the front facet of a glass prism with index matching immersion oil (Sigma 56822, n=1.516) between the glass substrate and the prism, as schematically depicted in figure 6.1 (b). The incident beam impinges on the sample at an incidence angle θ_I that is greater than the critical angle θ_C needed for TIR. Our structures are hence excited by an evanescent wave that has a wave vector component along the prism equal to the parallel wave vector of the incoming light ($\mathbf{k}_{||}$), and with some evanescent decay from the interface, set by $k_z = \sqrt{|\mathbf{k}_{||}|^2 - (\omega/c)^2}$. The scattered light is collected by a high NA 100x Olympus objective (NA=0.95), meaning that we collect scattered parallel wave vectors in the range $-0.95\frac{\omega}{c} \leq |\mathbf{k}_{||}| \leq 0.95\frac{\omega}{c}$. The microscope objective is mounted on a Newport ultralign micrometer stage for fine focusing and positioning, which is set at the end of an optical rail. This rail furthermore contains a set of two telescope lenses in order to create an intermediate real space image plane. We use this plane to select light from just one single nano-object, by placing a pinhole mounted on a flip mount. In our setup, we use a telescope lens with f = 50 mm, which implies a magnification of 27x. Therefore one could use commercially available 50 to 120 μm pinholes for spatial selection. In general, care must be taken that pinholes are small enough to exclude adjacent objects, yet large enough that Airy diffraction rings from the pinhole do not dominate the Fourier image. Moreover, we have found it necessary to deal with the fact that commercial pinholes are not circular, and the fact that the abrupt edges of binary pinholes always diffract. Therefore, we use Gaussian graded pinholes defined by digitally transferring 16-bit black and white tiff-file definitions of gaussian circular grayscale patterns in photographic black and white slide film by laser writing (www.colorslide.com). These pinholes have a smooth, apodized transmission in Fourier space. In order to block residual transmission through the nominally non-transmitting part of the film away from the pinhole (for which we estimate an optical density of 3), we glue the apodized

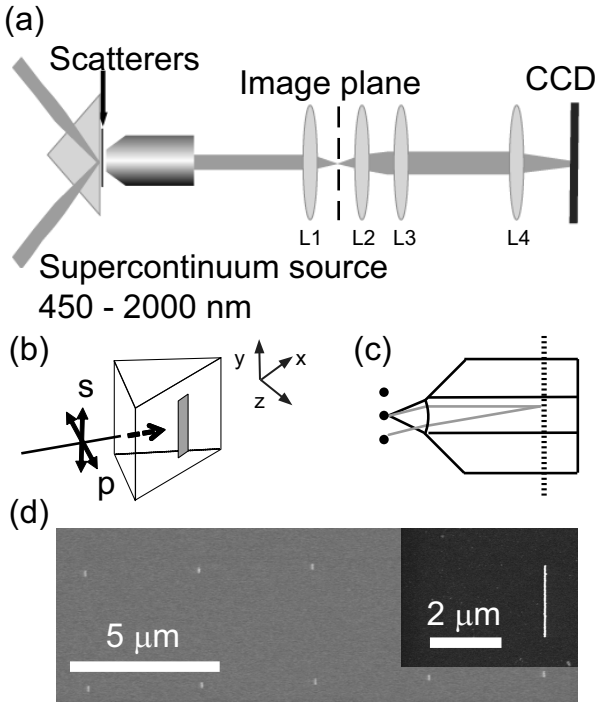

Figure 6.1: *(a) A schematic of the Fourier microscope set up. The set up consist of a high NA objective (NA=0.95), a set of telescope lenses L1 and L2 with equal focal lengths (f=50 mm), a Fourier lens L3 (f=200 mm) and a tube lens L4 (f=200 mm) that focuses the image on a silicon Charge Couple Device (CCD). To select a single scatterer, we place a pinhole in the image plane between L1 and L2. (b) A schematic representing the position of a nanowire on the prism front facet with a long axis oriented parallel to the y-axis, excited with s or p polarized incident light. (c) Ray diagram demonstrating the front and back aperture image planes. The light scattered by nano-objects is collected by the objective which forms a collimated beam (black lines). Each point in the back aperture of the objective (dashed black line) corresponds to a different wave vector (gray lines) scattered by any nano-object. (d) SEM image of an array of 200 nm long, 50 nm wide and 30 nm thick nanobars arranged in a periodic lattice with 4 μm lattice spacing. The inset shows an SEM zoom in of a 2 μm long, 50 nm wide and 30 nm thick Au nanowire.*

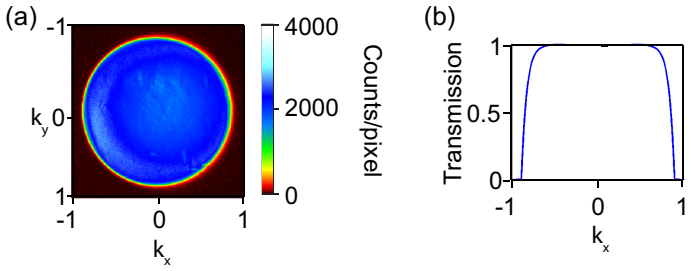

Figure 6.2: *(a) Fourier space image of a uniform layer of 100 nm dye-doped fluorescent beads excited with unpolarized incident light at 480 nm. The total exposure time is 0.4 s. (b) The blue line is the transmission function extracted from the measurements in (a).*

pinholes onto a stainless steel thin film with a mechanically drilled 300 μm hole. When used as a simple imaging microscope, the set up contains as only additional element a tube lens ($f = 200$ mm) that images the pinhole plane on a CoolSnap EZ Silicon CCD camera. In order to retrieve the radiation pattern of a single nano-object, i.e. the k-space image, we place a flippable Fourier lens between telescope and tube lens, at a distance $4f_{\text{telescope}} + f_{\text{Fourier}}$ from the back focal plane of the objective to focus the CCD camera on the microscope back aperture, rather than on the sample plane (i.e., at infinity in our infinity corrected microscope). Figure 6.1 (c) shows a ray tracing image of the light collected by the objective in real (black lines) and k-space (grey lines). Independent of the position of the object, each radiation angle is focused onto a unique location in the back aperture of the objective (dashed black line).

We calibrated the objective transmission function as a function of collection angle by measuring the intensity distribution in the back aperture from fluorescence emitted by dye-doped fluorescent beads (Invitrogen Fluospheres F8800) [17]. We have deposited a uniform layer of 100 nm beads by spincoating a 5% concentrated solution. The dye molecules have an emission peak at 535 nm. A set of band pass filters was used in the incoming beam (tuned to 480 nm) and the detection beam in order to selectively collect only the fluorescent light coming from the layer of dye molecules. The isotropic emission collected by our objective is shown in figure 6.2 (a). It has a non-uniform intensity distribution in Fourier space firstly because equidistant angles are not equidistant in the $\mathbf{k}_{||}$ space that our CCD images, and secondly because of the angle dependent apodization function $T(k_{||})$ of the objective. For an angularly isotropic emission we expect the collected intensity to

vary as

$$I(k_{||}) = \frac{P}{\cos(\arcsin(k_{||}))} T(k_{||}), \tag{6.1}$$

where $k_{||} = |\mathbf{k}_{||}|/k_0$. In our measurements, the objective transmission function $T(k_{||})$ is angle independent for angles between $0 \leq |\sin\theta| \leq 0.6$, rolling off to 50% of its peak value at $\sin\theta = 0.86$, as shown in figure 6.2 (b). Since the objective is specified for near infrared applications, we expect that the transmission edge, which essentially reaches zero already at an NA of 0.89, moves to larger angles for longer wavelengths, where the NA is specificied as 0.95 by the objective manufacturer [17]. The relation between pixel on the CCD camera and wave vector emitted in the object plane is easily calibrated by using the Fourier microscope without spatial filter. Since we use periodic structures, the collected pattern consists of grating diffraction orders that are equidistant in $k_{||}$-space. Indeed, in accord with the Abbe sine condition by which the objective is designed, we retrieve equidistant lattices of dots in $k_{||}$-space on the CCD camera, the spacing of which serves as calibration. In our set up, the full NA of the objective corresponds to a diameter of approximately 300 pixels on the camera.

6.3 Results and discussion

6.3.1 Fourier microscopy of an array of ultrashort gold nanobars

In order to demonstrate the potential of Fourier microscopy of single nano-objects, we have fabricated samples with Au nanobars of different lengths. The shortest bars that we fabricated (200 nm long, 50 nm wide, 30 nm high) are sub-wavelength (Fig. 6.1), and hence expected to have only weakly directional scattering patterns. In contrast, the longest bars (4 μm long, 50 nm wide, 30 nm high) are so long that they are expected to have several plasmon guided mode Fabry-Perot resonances and potentially quite directional scattering patterns [18–20]. The inset of Fig. 6.1 (d) shows a SEM image of a single 2 μm long and 50 nm thick nanowire. The nanobars were fabricated by defining lines in e-beam lithography in ZEP-520 resist, employing thermal evaporation of Au, and subsequently lift-off in 1-methyl-2-pyrrolidinone (NMP). The nanowires are arranged in periodic square arrays with lattice spacing equal to 20 times the nanowire length, as shown in Fig. 6.1 (d). The pitch is large enough to avoid any coupling between objects, yet small enough so that we can easily find fields of objects in widefield or darkfield microscopy. Fig. 6.3 (a), (b), and (c) show Fourier images of a periodic array of 200 nm Au nanowires with 4 μm lattice spacing, without spatial filtering, excited by p-polarized light (a) and polarization analyzed along (b) and across (c) the nanobar length. The white edge around the intensity distribution depicts the measured NA

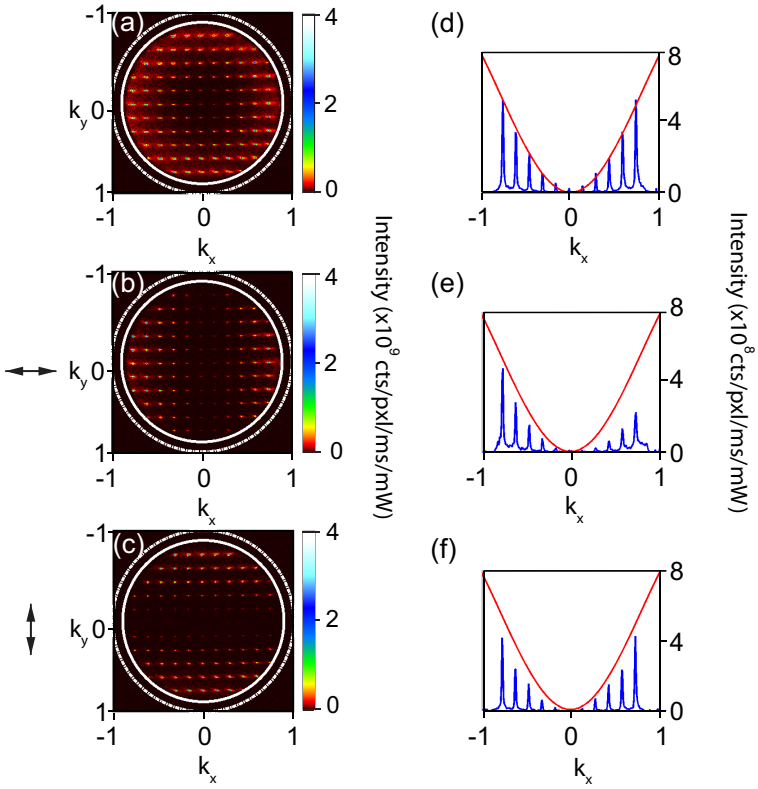

Figure 6.3: *(a) Fourier space image of a periodic square array of 200 nm long, 50 nm wide and 30 nm thick Au nanobars with 4 μm lattice spacing excited with p-polarized incident light at 600 nm with 20 μW. The total exposure time is 10 ms. (b), (c) Radiation patterns under the same illumination conditions as in (a) and polarization analyzed across (b) and along (c) the nanobar length, as denoted by the black arrows. (d), (e), (f) Fitted $\sin^2$ (red line) to cross sections along the central column ((a), (c)) and row ((b)) of grating orders in our measurements in (a), (b) and (c), respectively, with a scaling factor of 11×10^8 and an offset of 3×10^6 counts per pixel, per mW incident power and per ms exposure time.*

of our objective (full white line), corresponding to all wave vectors up to 89 % of the maximum wave vector in free space (dashed white line), while the center of the image corresponds to $k_{||}$=0. The Fourier space is clearly dominated by grating orders, as expected for a periodic array.

Interestingly, not all grating diffraction orders are equally intense. We expect [2] that the Fourier space scattering of a periodic array of scatterers is the product of the radiation pattern of each single scatterer and the structure factor of the array that is a set of δ-peaks at the vectors $\mathbf{k}_{||} + \mathbf{G}$ (where $\mathbf{G}$ is any of the reciprocal lattice vectors, Eq. (4.9)). In other words, the radiation pattern of an array makes up a sparse sampling of the single object radiation pattern. In this data we recognize that the central orders near $k_{||} = 0$ are much weaker than the orders at larger angles, as seen from cross sections through our data along k_x in figure 6.3 (d), (e), and (f) (blue lines). For this data set, we have used excitation with p-polarized light, obtained by placing a polarizer in the incident beam. For p-polarized driving we expect that each nanobar obtains a large, out of plane dipole moment. For out-of-plane dipoles we expect that the single building block radiation pattern is strong at large angles and weak near $k_{||} = 0$, since the radiation pattern of a single dipole is given by $P \sim \sin^2\theta = k_{||}^2$. We demonstrate this behavior by fitting the $\sin^2$ to the cross sections in figure 6.3 (d), (e) and (f) (red lines). The fact that the grating diffraction orders represent a discrete sampling of this single block radiation pattern is further confirmed by a polarization analysis, realized by placing a second polarizer immediately after the microscope objective. The grating diffraction orders reveal a radial polarization around the intensity node at $k_{||} = 0$, consistent with the radial polarization expected for a single out-of-plane dipole moment.

6.3.2 Fourier microscopy of single scatterers

The measurements in Fig. 6.3 (a) and (b) show that Fourier microscopy of arrays of nano-objects is strongly limited by the fact that angle-dependent scattering strength is sampled only at a sparse set of points, set by the grating diffraction orders. We will now present measurements that show that it is possible to even measure radiation patterns of single sub-wavelength plasmonic scatterers with our Fourier microscope. To this end we flip the spatial selection filter into the image plane between lens L1 and L2 in the telescope (Fig. 6.1), to select a single scatterer. When the spatial selection filter is in place, the grating orders disappear and we can observe the full structure of the radiation pattern. In Fig. 6.4 (a) and (b) we show radiation patterns (measured without a polarizer in the collection path) of 2 μm and 1 μm Au bars that are perpendicular to the scattering plane of the incident, p-polarized light. In this configuration, the incident beam excites the entire object in phase ($k_{||} = 0$), since the extent of the nanowires as measured along the incident wave vector is only

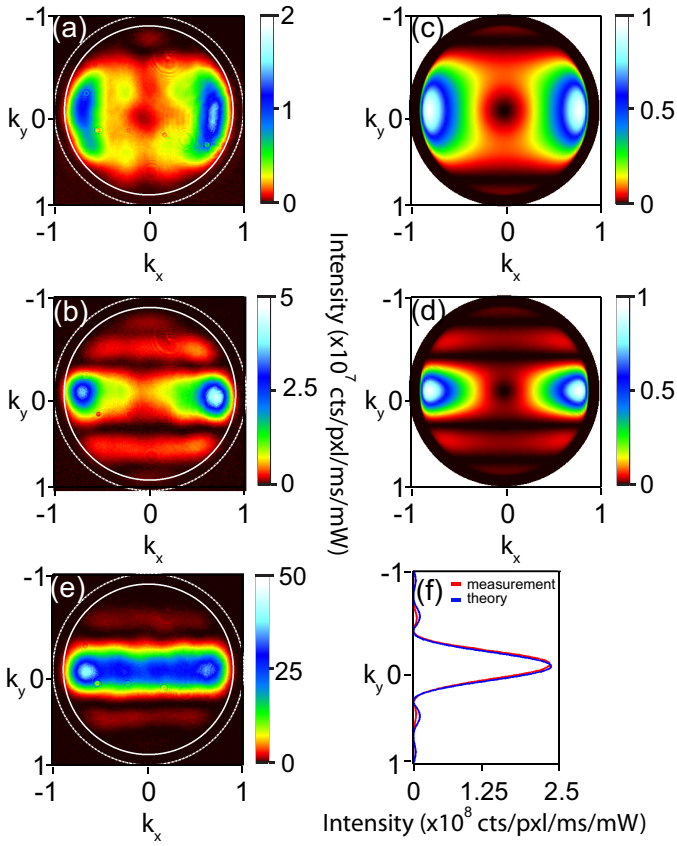

Figure 6.4: *(a) Fourier space image of a 1 μm long, 50 nm wide and 30 nm thick Au nanowire excited by p-polarized incident light. (b) Fourier space image of a 2 μm long, 50 nm wide and 30 nm thick Au nanowire excited by a p-polarized incident light. (c) and (d) are calculated radiation patterns of 2 μm and 1 μm long Au nanowires multiplied by the transmission function, respectively. (e) Fourier space image of a 2 μm long, 50 nm wide and 30 nm thick Au nanobar excited with s-polarized incident light. The nanobars are excited at 725 nm and 200 μW. The total exposure time is 1 s in (a), 100 ms in (b), and 10 ms in (e). (f) An average cross-cut of (e) along k_y (red curve) agrees well with the calculated sinc^2 behavior (blue line).*

50 nm (the wire width). The images reveal low to no intensities in Fourier space around $k_{||} = 0$, with most of the intensity concentrated at high angles, specifically at high k_x, yet small k_y. Furthermore, upon comparison of the radiation pattern of the 2 μm and 1 μm wire, we observe that while both radiation patterns are confined to a narrow range of wave vectors near $k_y = 0$, this confinement is roughly two times greater for the longer wire. The measurements further show secondary maxima around the main lobe centered at $k_y = 0$. An increasing concentration of scattered radiation around a central direction with wire length was also noted by Shegai *et al.* [8], demonstrating stronger directionality for wires with a higher geometrical aspect ratio. Complementary measurements for s-polarized driving on a 2 μm Au bar (Fig. 6.4 (e)) also show strong directionality when dipole moments are excited along the bar. Again the radiation pattern is confined to a narrow region around $k_y = 0$. A striking difference with p-polarized driving, however, is that intensity is more uniformly distributed along the k_x-axis, with no apparent reduction of intensity at $k_{||} = 0$. This set of measurements clearly shows the main advantage of our Fourier microscope, i.e., the ability to map the full back aperture of our objective for light scattered by a single nano-object. For instance, the striking difference in radiation pattern depending on polarization of the driving would not have been noticed in set ups [7, 8, 16] that collect only large wave vectors beyond total internal reflection.

In order to understand the radiation patterns of our nanowires, we implement a simple model. We hypothesize that the radiation pattern of wires can be simply described as that of a set of point dipoles arranged in a line over the length of the wire. For this case, we expect that different volume elements along the length L of the wire are all excited in phase, and with equal incident amplitude and are all polarized along the optical axis of the setup. Due to the slight phase differences accumulated for waves traveling to a given observation point in the far field from different positions on the wire, the radiation pattern of a line of dipoles is modified by the form factor of the wire, obtained by integrating over the wire. In the theory of microscopic imaging with high NA aplanatic lenses that satisfy the Abbe sine rule, it is well known that the back aperture field can be found directly from the field on a reference sphere of radius f, where f is the objective focal distance [21, 22]. If we divide the wire into area elements $\mathrm{d}x\mathrm{d}y$, the field on the reference sphere will be

$$\mathbf{E}(\theta,\phi) \sim \frac{\mathbf{E}_{\mathrm{dip}}^{\mathrm{far}}(\theta,\phi)}{f} \int_{\text{wire area}} e^{-ik_0 R_f(\theta,\phi,x,y)} \mathrm{d}x\mathrm{d}y, \tag{6.2}$$

where $\mathbf{E}_{\mathrm{dip}}^{\mathrm{far}}(\theta,\phi)/f$ is the electric field amplitude given by the radiation pattern of a single dipole. For a case where $f \gg L$, the distance from the radiator to reference sphere $R_f(\theta,\phi,x,y)$ simplifies to $R_f = f - \frac{\mathbf{k}_{||}}{k_0} \cdot \mathbf{r}_{||}$, where $\mathbf{k}_{||} =$

$k_0(\cos\phi\sin\theta, \sin\phi\sin\theta, \cos\theta)$, and where $\mathbf{r}_{||} = (x, y, 0)$. For a wire of length L oriented along the y-axis, and of infinitesimally small width, the integral simplifies to

$$\mathbf{E}(\mathbf{k}_{||}) = \mathbf{E}^{\text{far}}_{\text{dip}}(\mathbf{k}_{||})\frac{e^{ik_0 f}}{f}\int_{-L/2}^{L/2} e^{-ik_y y}\mathrm{d}y \propto \mathbf{E}^{\text{far}}_{\text{dip}}(\mathbf{k}_{||})\text{sinc}(k^y_{||}L/2), \tag{6.3}$$

This calculation is analogous to calculating Fraunhofer diffraction of a slit, but now is applied to nanoscale scatterers with wide radiation patterns that are far from paraxial. Our calculation predicts that the polarization content and intensity is directly inherited from the radiation pattern of a single point dipole multiplied by a sinc function that applies irrespective of incident or collected polarization. The calculation in essence predicts that the radiation pattern of a nanowire is that of a single dipole multiplied by a sinc^2 function that ensures that the longer the wire is, the stronger the radiation is confined to the plane transverse to the wire. The excellent correspondence between the data in Fig. 6.4 and the calculation not only concerns the width of the central lobe, set by the sinc^2 function, but also the appearance of a minimum in scattered intensity at the center of the pattern that is proportional to $|\mathbf{E}^{\text{far}}_{\text{dip}}(\mathbf{k}_{||})|^2$. In addition, the calculation also correctly predicts the location of side lobes in the k_y direction. For completeness we provide a cross-cut through data and theory, obtained by integrating data in Fig. 6.4(e) along k_x. Data (red line) and theory (blue line) in Fig. 6.4 (f) are in excellent agreement. The absence of a hole in the radiation pattern in Fig. 6.4(e) is furthermore consistent with the fact that $|\mathbf{E}^{\text{far}}_{\text{dip}}(\mathbf{k}_{||})|^2$ has no central minimum for in-plane oriented dipole moments.

As noted above, our calculation predicts that the polarization content of the scattered light is directly inherited from the radiation pattern of a single point dipole. To verify this prediction, we place a polarizer directly behind the microscope objective to analyze the polarization of the scattered light, as reported in Fig. 6.5 for p-polarized excitation. Since the single-dipole riadation pattern is radially polarized, analyzing the polarization of the 2 μm nanowire radiation pattern along k_x only retrieves the main lobe of the sinc^2 function. For cross polarization, i.e., polarization along the wire, the field $\mathbf{E}_y(\mathbf{k}_{||})$ has a node at $k_y = 0$. As a consequence the main lobe is crossed by a nodal line and is strongly suppressed so that it becomes comparable in brightness to the low intensity side lobes at larger k_y. Our measurements with the polarization analyzer (Fig. 6.5 (a) and (b)) show very good agreement with the calculations (Fig. 6.5 (e) and (f)). We have also polarization analyzed Au nanowires that are perpendicular to the scattering plane, but with s-polarized incident light. Fig. 6.5 (c) and (d) show measured radiation patterns that are polarization analyzed along (c) and across (d) the nanowire length. Again, the

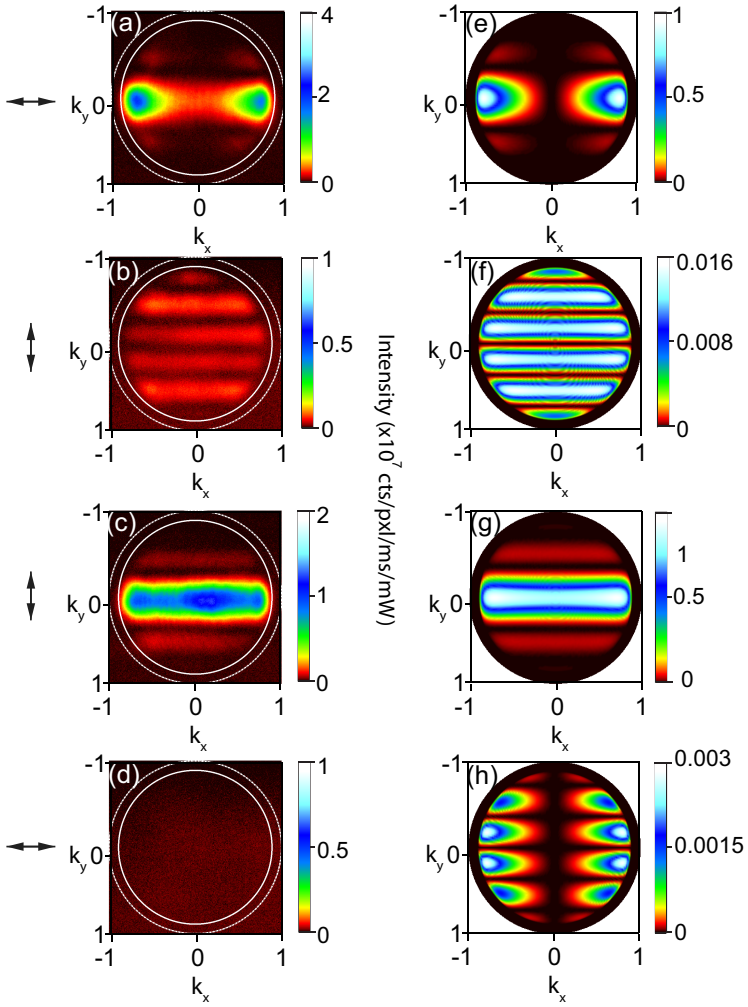

Figure 6.5: *(a), (b) Polarization analyzed radiation patterns of 2 μm long, 50 nm wide and 30 nm thick Au nanowires excited by a p-polarized incident light at 650 nm with 200 μW along (a) and across (b) the nanowire length, as denoted by the black arrows. The exposure time in (a) is 300 ms and in (b) 1 s. (c), (d) Polarization analyzed radiation patterns for the same nanowire excited by an s-polarized incident light at 650 nm and 200 μW along (c) and across (d) the nanowire length, as denoted by the black arrows. The exposure time in (c) is 500 ms and in (d) 1 s. (e)-(h) Calculated radiation patterns corresponding to the illumination conditions measured in (a)-(d), respectively, multiplied by the transmission function.*

measurements show very good agreement with the calculations of the same polarization analysis shown in Fig. 6.5 (g) and (h). Note that the calculation in Fig. 6.5 (g) has much lower intensities than (e) and (f). For both arrays of short nanobars and single nanowires we have data sets for wavelengths in the range from 500 nm to 725 nm that are detectable by our CCD camera. In this wavelength range, we observe no strong wavelength dependence of the radiation patterns, since the resonance for a z-oriented dipole does not fall within this wavelength range. The only noticeable differences arise in array measurements from grating diffraction, as the location of the grating diffraction orders is wavelength dependent.

6.3.3 Radiation pattern of single Au nanowires oriented in the scattering plane

So far we have considered radiation patterns of single Au nanowires perpendicular to the scattering plane of the incident beam, in which case the whole wire is excited in phase. Many excitations in small nano-objects will benefit from excitation with $\mathbf{k}_{||}$ different from 0. For instance, for understanding the excitations of 1D objects like wires and particle chains, it would be advantageous to phase-match the excitation wave vector to that of guided modes. Therefore, we have also studied radiation patterns of Au nanowires that are oriented in the scattering plane of the incident wave. Fig. 6.6 (a) shows a measured radiation pattern of an array of 2 μm long Au nanowires with 40 μm lattice spacing. A nanowire that is excited with p-polarized light has a radiation pattern dominated by the sinc^2 function that is given by the total length of the object, as previously discussed. However, now the sinc function is rotated by 90° together with the wire (Fig. 6.6 (b)), and displaced from wave vector $k_{||} = 0$ to be centered at the incident wave vector $\mathbf{k}_{||}$. Of course, since we are working in TIR, the incident wave vector and hence the main lobe of the sinc^2 function is just outside the part of Fourier space accessible to our objective. In our configuration the central lobe is located at the left hand side just outside the Fourier image (red dashed line in Fig. 6.6 (b)). A striking difference with measurements with in-phase excitation (Fig. 6.4) is furthermore that the overall collected signal per bar is much weaker. We attribute this weak signal to the fact that the main lobe of the sinc^2 function is beyond the light line in air, reducing scattering into the collection side of the set up. It is for this reason that Fig. 6.6 shows data obtained without pinhole on a sample with a very dilute set of wires (40 μm lattice spacing), rather than with pinhole. Compared to data with pinhole (not shown), the advantage is a large boost in signal, though at the price of obtaining only a sparse sampling of the radiation pattern, due to grating diffraction as in Fig. 6.3.

We have measured radiation patterns for p-polarized incident light and nanowire orientation for a wide range of incident frequencies. Fig. 6.6 (b) shows the position

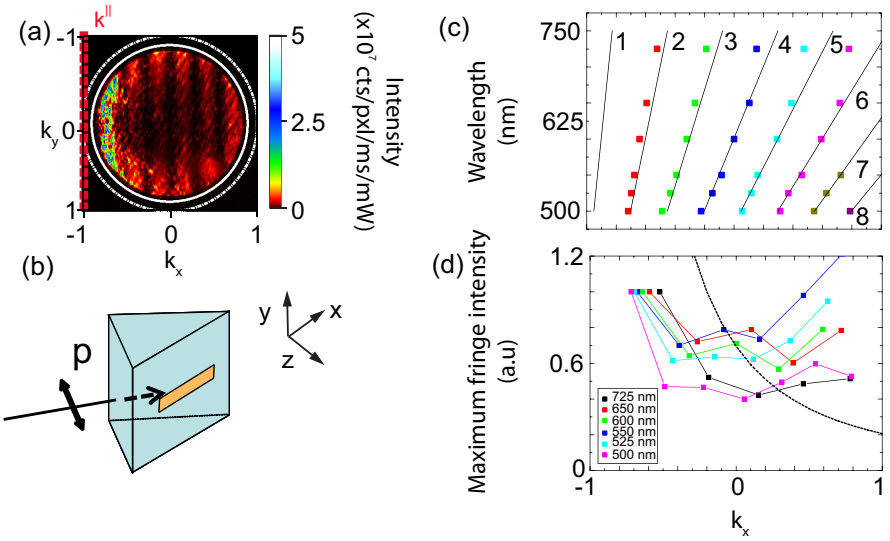

Figure 6.6: *(a) A schematic representing the position of a nanowire on the prism front facet with a long axis parallel to the x-axis, excited with p polarized incident light. (b) Fourier space image of a horizontal 2 μm long, 50 nm wide and 30 nm thick Au nanobar excited with p-polarized incident light at 550 nm and 8 μW. The exposure time is 1 s. (c) Location of the fringe intensity maxima measured in (b) along k_x. The black lines show the predicted position of the intensity lobes away from the zero-order lobe. Symbols are black, red, green, blue, cyan, magenta, dark yellow and purple for fringe orders m = 1-8, respectively, marked by numbers. (d) Symbols (connected by lines for clarity): maximum fringe intensity normalized to the m=2 fringe intensity versus parallel wave vector. The black dashed line depicts the expected $1/|k_x^{in} - k_x|^2$ behavior of the intensity lobes. Fringes with the same wavelength but different orders are color coded.*

of radiation pattern fringe maxima for a 2 μm nanowire as a function of incident frequency. As expected, the fringe maxima are equidistantly spaced by $k_x/k_0 = \lambda/L$, and originate from a central zero-order lobe just outside the diagram. Further, we would expect the fringe intensity to drop off as $1/|k_x^{in} - k_x|^2$. However, we don't observe such a monotonic fringe intensity drop off in all our data sets. Specifically, Fig. 6.6 (c) shows that all fringes are more or less comparable in brightness for $\lambda < 650$ nm across the whole back aperture. Only for $\lambda = 725$ nm and above (not shown) do we find a drop off in fringe brightness commensurate with the expected sinc^2 tail. A possible explanation is that plasmonic resonances of the wire modify the radiation patterns. Indeed, it has been predicted [20, 23] that the current distribution excited in a metal wire not only has a component directly proportional to the incident field (wave vector $\boldsymbol{k}_{||}$), but also due to standing plasmon wave oscillations along the wire. Such standing waves would add extra contributions to the radiation pattern that are again of the form of $\text{sinc}(kL/2)$, but centered at $k_x = \pm k_{SPP}$, i.e., at the guided plasmon wave vector. A detailed analysis of fringe intensity versus k_x would allow to extract the dispersion relation of the nanowire. However, in our data, this analysis is obscured by the fact that plasmon resonances in lithographically fabricated Au wires are generally not very strong due to losses, and by the fact that in total internal reflection illumination, the plasmonic x-oriented mode is only weakly driven. Indeed, for incident angles higher than the critical angle required for TIR, $\theta_I > \theta_C$, the evanescent wave at the surface of the prism has an electric field component along z, which for the incidence angle in our experiments (52°) is 2.5 times greater than the x-oriented field. Separating the non-resonant, but strongly excited polarization perpendicular to the wire from the weakly excited but possibly resonant wire plasmon radiation patterns is outside the scope of this chapter. For application of Fourier microscopy to complex resonant structures in general, it is a major challenge to simultaneously control the required incident phase gradient over the structure and achieve the desired polarization, while also remaining in total internal reflection or dark field excitation mode. We suggest that combining Fourier microscopy with wavefront phase shaping [24] may be a promising route to extract further quantitative information to benchmark models such as those proposed in [20, 23].

6.4 Summary and conclusion

In conclusion, we have built a Fourier microscope that is suited for measuring the radiation pattern of single plasmonic and metamaterial scatterers. We have successfully measured radiation patterns of single Au nanowires with different lengths down to 200 nm, even though signal levels drastically reduce with size. Since Fourier microscopes always operate in dark field mode, the incident excitation field

is limited in polarization and wavefront. We have shown that even with the class of driving fields available in total internal reflection mode one can obtain useful quantitative response characteristics, as long as the polarization and phase gradient applied over the structure are precisely known. We hence anticipate that we will be able to extend this method directly to quantify the magnetoelectric scattering properties in Fourier space of many interesting, but previously uncharted, plasmonic and metamaterial structures, such as split ring resonators, cut-wire pairs, pseudo-chiral objects, and oligomers where spectra are characterized by Fano resonances [25–27].

Bibliography

[1] H.C. van de Hulst *Light Scattering by Small Particles*, Dover, New York (1981).

[2] F. J. García de Abajo Rev. Mod. Phys. **79**, 1267 (2007).

[3] M. Husnik, M. W. Klein, N. Feth, M. König, J. Niegemann, K. Busch, S. Linden and M. Wegener, Nat. Phot. **2**, 614 (2008).

[4] I. Sersic, M. Frimmer, E. Verhagen and A. F. Koenderink, Phys. Rev. Lett. **103**, 213902 (2009).

[5] A. Pors, M. Willatzen, O. Albrektsen and S. I. Bozhevolnyi, J. Opt. Soc. Am. B **27**, 1680 (2010).

[6] I. Sersic, C. Tuambilangana, T. Kampfrath and A. F. Koenderink, Phys. Rev. B **83**, 245102 (2011).

[7] A. G. Curto, G. Volpe, T. H. Taminiau, M. P. Kreuzer, R. Quidant and N. F. van Hulst, Science **329**, 930 (2010).

[8] T. Shegai, V. D. Miljković, K. Bao, H. Xu, P. P. Norlander, P. Johansson and M. Käll, Nano Lett. **11**, 706 (2011).

[9] M. A. Lieb, J. M. Zavislan and L. Novotny, J. Opt. Soc. Am. B **21**, 1210 (2004).

[10] D. Patra, I. Gregor, J. Enderlein and M. Sauer, Appl. Phys. Lett. **87**, 101103 (2005).

[11] H. Aouani, O. Mahboub, N. Bonod, E. Devaux, E. Popov, H. Rigneault, T. W. Ebbesen and J. Wenger, Nano Lett. **11**, 637 (2011).

[12] N. LeThomas, R. Houdr, M. V. Kotlyar, D. O'Brien, and T. F. Krauss, J. Opt. Soc. Am. B **24**, 2964 (2007).

[13] A. Drezet, A. Hohenau, D. Koller, A. Stepanov, H. Ditlbacher, B. Steinberger, F. R. Aussenegg, A. Leitner and J. R. Krenn, Mat. Sci. and Eng. B **149**, 220 (2008).

[14] S. Randhawa, M. U. Gonzáles, J. Renger, S. Enoch and R. Quidant, Opt. Expr. **18**, 14496 (2010).

[15] Y. Alaverdyan, E-M. Hempe, A. N. Vamivakas, E. Haibo, S. A. Maier and M. Atatüre, Appl. Phys. Lett. **94**, 021112 (2009).

[16] C. Huang, A. Bouhelier, G. Colas des Francs, A. Bruyant, A. Guenot, E. Finot, J. C. Weeber and A. Dereux, Phys. Rev. B **78**, 155407 (2008).

[17] L. Dai, I. Gregor, I. von der Hocht, T. Rockstuhl and J. Enderlein, Opt. Expr. **13**, 9409 (2005).

[18] H. Ditlbacher, A. Hohenau, D. Wagner, U. Kreibig, M. Rogers, F. Hofer, F. R. Aussenegg and J. R. Krenn, Phys. Rev. Lett. **95**, 257403 (2005).
[19] E. J. R. Vesseur, R. de Waele, M. Kuttge and A. Polman, Nano Lett. **7**, 2843 (2007).
[20] J. Dorfmüller, R. Vogelgesang, W. Khunsin, C. Rockstuhl, C. Etrich and K. Kern, Nano Lett. **10**, 3596 (2011).
[21] P. Török, P. D. Higdon and T. Wilson, J. Mod. Opt. **45**, 1681 (1998).
[22] O. Haeberlé, M. Ammar, H. Furukawa, K. Tenjimbayashi and P. Török, Opt. Expr. **11**, 2964 (2003).
[23] T. H. Taminiau, F. D. Stefani and N. F. van Hulst, Nano Lett. **11**, 1020 (2011).
[24] I. M. Vellekoop and A. P. Mosk, Opt. Lett. **32**, 2309 (2007).
[25] M. Hentschel, D. Dregely, R. Vogelgesang, H. Giessen, and N. Liu, ACS Nano **5**, 2042 (2011).
[26] J. B. Lassiter, H. Sobhani, J. A. Fan, J. Kundu, F. Capasso, P. Nordlander, and N. J. Halas, Nano Lett. **10**, 3184 (2010).
[27] M. Frimmer, T. Coenen, and A. F. Koenderink, Phys. Rev. Lett. **108**, 077404 (2012).

Chapter 7

Outlook

The main proposition of this thesis is that split rings scatter as magnetoelectric dipoles. In this chapter we ask how can one either challenge and overturn, or further confirm this view. We suggest that the validity of a dipole picture can be directly tested by measuring radiation patterns of single and coupled split rings. Therefore, we present a theoretical investigation of the radiation patterns of single split rings, as well as stereodimers of split rings on a glass substrate. We discuss problems such experiments will likely encounter. Finally, we outline prospective applications of metamaterial scatterers that go beyond achieving negative refractive index.

7.1 Experiments to test the model

Throughout this thesis we have aimed to quantify the response of individual split ring resonators. Based on our experiments that study coupling of split rings, we have developed a fully electrodynamical model that assigns an electric, magnetic and magnetoelectric polarizability to split rings. This model successfully predicts quantitative extinction cross sections, radiation patterns and optical activity of metamaterial scatterers, as far as we have probed in array experiments shown in Chapters 2, 4 and 5. In our model, the main premise is that electric, magnetic, and magnetoelectric dipole moments, should have approximately equal strength that is large compared to the 'unitary limit' of strongest scattering while simultaneously ignoring all higher order multipole moments. Naturally, these should be assumptions of considerable debate. Firstly, as exemplary formulated by Merlin [1], many researchers would expect e.g. electric quadrupole moments to dominate over the magnetic dipole response of SRRs. Secondly, a particular problem with assigning magnetic dipole moments is that its magnitude is not origin independent. Finally,

some researchers wish to avoid the magnetic dipole moment picture altogether, stating simply that the LC resonator feels the gradient in $\boldsymbol{E}$ due to its size (which $\boldsymbol{H} = \nabla \times \boldsymbol{E}$ is arguably a part of). Hence, it is important to ask if we can devise experiments that could further confirm or falsify the hypothesis of a dipolar description. One would expect a breakdown of any dipole moment picture as soon as higher order multipole moments are excited, which happens in two circumstances. First, if the object is single, but large compared to the wavelength, even a plane wave excitation excites multipoles. Second, if strong gradients are applied over an object due to the very nearby presence of a second scatterer, or due to highly local excitation, multipoles could be excited even for small objects. Here we do not focus on this second, trivial case in which multipoles occur, since we are interested in the intrinsic single building block description. As further tests beyond array measurements, we can think of two tests in scattering experiments. Firstly, one could attempt to measure the radiative linewidth of the extinction cross section as the split ring is held in front of an interface. Buchler *et al.* [2] showed that that such an experiment is indeed feasible. He demonstrated that for a single plasmon particle, the linewidth varies with frequency due to an LDOS effect similar to the lifetime modification of a fluorophore at an interface. In this experiment, one might test if the assumed magnetic scatterer actually probes the magnetic dipole local density of states (LDOS) [3], or higher order multipolar LDOS generalizations [4]. As a second experiment, which is achievable with the tools offered in this thesis, we propose that the radiation pattern of a single split ring could be measured. In Chapter 6 we demonstrated that one can measure the radiation pattern of a single scatterer, but only provided one manages to create a dark field set up. For isolated metal scatterers, as opposed to e.g. holes in a metal screen, this means that one cannot study the radiation pattern of a split ring in homogeneous space, but only of split rings on a high-index interface, under TIR conditions. This geometry has two disadvantages. First, one cannot choose the incident field and its polarization freely. Second, a major part of the light goes into the substrate where one does not measure.

7.1.1 Fourier microscopy of split rings

Let us calculate if measuring radiation patterns of split rings would yield interesting results on the magnetoelectric dipolar behavior of split rings in a best case TIR scenario. First we calculate the driving field by calculating the field at the glass-air interface in absence of any scatterer, assuming incidence from glass under TIR incidence, for various polarizations. Next, we calculate the complex induced dipole moments ($\boldsymbol{p}$, $\boldsymbol{m}$) by multiplying the fields with the split ring polarizability. Here, care should be taken that the polarizability is modified by the presence

of the interface according to $1/\boldsymbol{\alpha} = 1/[1/\boldsymbol{\alpha}_{\text{vacuum}} - \mathcal{G}_{\text{scattered}}]$, where $\boldsymbol{\alpha}_{\text{vacuum}}$ is the electrodynamic polarizability in vacuum, and $\mathcal{G}_{\text{scattered}}$ is the scattered part of the Green function $\mathcal{G}_{\text{scattered}} = \mathcal{G}_{\text{interface}} - \mathcal{G}_{\text{free}}$ (as shown in Ref. [5], Chapter 10 and pages 494-495). This correction takes into account that both the resonance frequency and the radiative linewidth of the scatterer is modified at the interface. Intuitively this can be understood as resonance hybridization of the split ring resonance with its own mirror image in the interface. We use values for α_{vacuum} based on ω_0 =1.26×10^{15} s^{-1}, $\alpha_E = 3.4V$, $\alpha_H = 1.5V$, and $\alpha_C = 1.9V$, close to maximally cross coupled as argued in Chapter 5, where V=0.0012 μm^2 is the particle volume, and where Ohmic damping $\gamma = 1.25 \times 10^{12}$ s^{-1} is set to be negligibly small for this best-case scenario calculation [6]. As a final calculation step we calculate the radiation pattern by superimposing the electric and magnetic fields radiated by the induced electric and the magnetic dipole, far field expansions for which were first derived in [7–10].

For a single SRR 80% of the emission is directed into two lobes that point into the substrate, as shown in Fig. 7.1 (a). These lobes are close to the critical angle associated with the air-glass interface, as is well appreciated in the field of single molecule microscopy [5], where similar phenomena occur in emission. The remaining 20% is emitted into the air side, and is emitted over a broad angular range. The plots in Fig. 7.1 (b)-(f) show polar diagrams of air-side radiation converted into intensity distributions patterns as expected to be seen by our objective (NA=0.95), polarization-analyzed in the back aperture. On the air side, we expect to collect $< 20\%$ of the emission as a rather homogeneous pattern extending over the full objective, much like the pattern simply expected from a horizontal electric dipole, as shown in Fig. 7.1 (b). Note that the minute left-right asymmetry in the un-polarized and linearly polarized graphs is not an artefact, but due to asymmetric excitation in an TIR geometry. An interesting observation is that circular polarization analysis of scattered light is expected to show a handedness-dependent asymmetry in the radiation pattern. This asymmetry seen in Fig. 7.1(e) and (f) is related to the expected off-angle pseudochiral extinction and the fact that the magnetoelectric response is maximally cross coupled.

We have also studied calculated radiation patterns of stereodimer structures made of a pair of SRRs, previously reported in [11], in order to decide if stereodimers would provide sharper features that would allow for easier determination in experiments than the broad features of single split rings. Coupling in such structures results in a complex resonant behavior as a function of twist angle, where frequency splitting and the anti-crossing carry interesting physics, as shown in Fig. 3.3 that could be observed in radiation patterns. We would hope to find large differences in radiation pattern or in optical activity therein for 0°/90°/180° twist angle, and for the different resonances. We calculated the eigenfrequencies of the

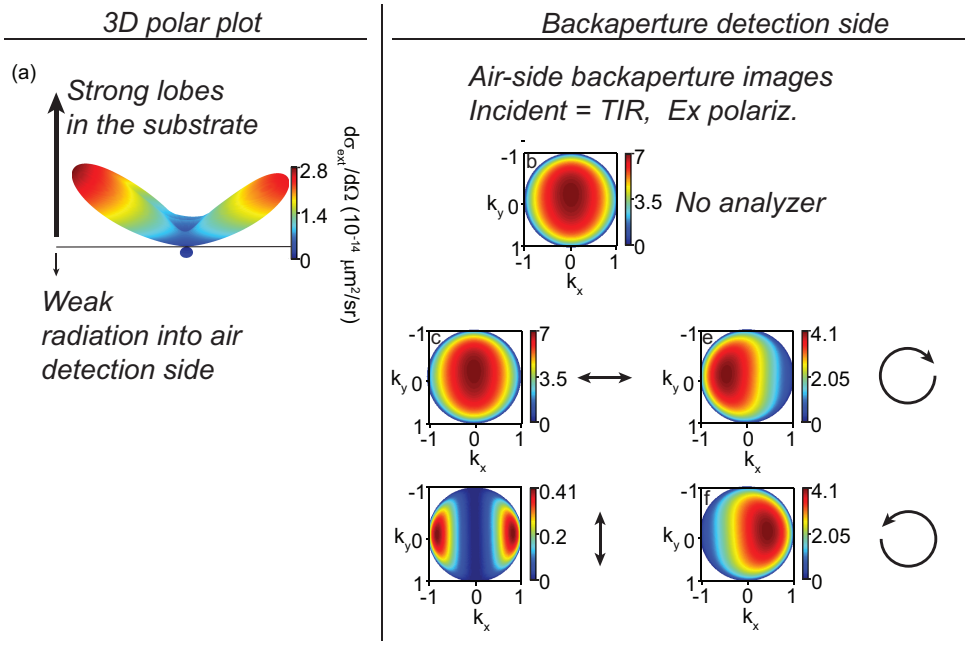

Figure 7.1: *(a) Calculated radiation pattern of a single split ring on a glass-air interface. (b) Calculated radiation pattern of an individual split ring collected by a high NA objective (NA=0.95) on the air side. The patterns in (c) and (d) are analyzed with a linear polarizer, while in (e) and (f) they are analyzed with a circular polarizer.*

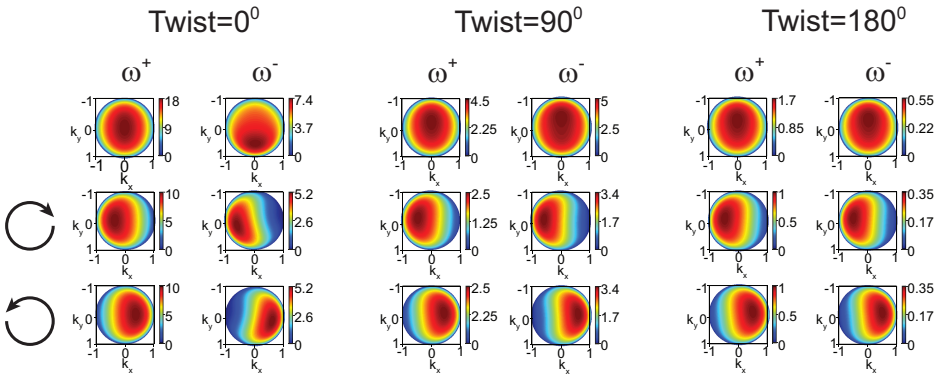

Figure 7.2: *Radiation patterns of split ring stereodimers with 0°, 90° and 180° twist angle. The radiation patterns in the second and third row are polarization analyzed with circular polarizer of handedness that is depicted by the black arrows on the left hand side.*

two anticrossing bands in presence of the dielectric interface, by obtaining normal-incidence extinction versus twist angle and versus frequency for dimers resonant at 1500 nm, buried just inside a $n = 1.5$ dielectric, and with 150 nm vertical center-to-center spacing. Next, we calculated the radiation patterns on the air side for 0°/90°/180° twist, assuming TIR incidence (45° incidence angle in glass, linearly polarized), as shown in Fig. 7.2. The extinction at this angle is very similar to normal-incidence results, as shown in Fig. 3.3. For all cases, circular analyzers again bring out handedness-dependent asymmetry in the angular radiation pattern, very much as in the single SRR case. When comparing the different resonances at set twist, or patterns at different twists for a given resonance branch, it can be noted that there are subtle differences only. Indeed, the asymmetries don't change in sign, or orientation, or magnitude significantly.

From the above analysis, it is tempting to conclude that measuring radiation patterns of single SRRs can be used to demonstrate the presence of electric and magnetic dipoles especially in the case when they are analyzed for circularly polarized light. In the case of linear analysis, the signal reaching our detector does not show large differences between a single in-plane electric dipole and a magnetoelectric scatterer such as a SRR. Circular polarization analysis, however, shows a clear handedness-dependent left-right asymmetry due to the magnetoelectric coupling that is at its maximum, as presented in Chapter 5. Such a set of measurements could therefore conceivably confirm or reject the hypothesis that a split ring is in fact a magnetoelectric scatterer consistent with our point dipole model. However, we note that the overall problem in the above mentioned measurements is the signal strength

especially at infrared frequencies, where the set up proposed in Chapter 6 has worse performance due to the poorer characteristics of IR detectors, and the fact that no feature in the radiation pattern stands out as particularly sharply defined. Therefore, we must conclude that the possibilities for quantifying SRR response and its dipolar nature via radiation patterns are slim. The essential problem is the modification of the radiation pattern by the air-glass interface. Collection into air means only a fraction of the light is collected, which gives a comparatively featureless signal. The situation is exacerbated by the fact that in our experiments (Chapter 6 and our initial attempts on split rings), either signal is too low when trying to measure from single objects, or grating diffraction patterns sample single object radiation pattern only sparsely, as demonstrated in Fig. 6.3. Pilot experiments of structures in Fig. 7.3 (a) indeed show no clear signature discriminating Fig. 7.1 against different models. One could argue that the dominating interface asymmetry could be avoided by embedding a split ring in a homogeneous medium, e.g. immersion oil. However, this would remove the dark field conditions required for Fourier microscopy. The air-glass interface could be avoided altogether if one places confidence in Babinet principle to do the reverse experiment, using air split rings in a metal film, instead of metal split rings in a dielectric [12, 13]. We have used focused ion beam milling to generate such split rings in Au, as shown in Fig. 7.3 (b). Here, both sides of the structure could be index-matched while keeping a dark-field microscopy approach. By way of pilot experiment, we have extended the Fourier microscope described in Chapter 6 to the IR regime where metamaterial scatterers have the strongest electric and magnetic responses. The IR branch of our set up is the same as the VIS branche described in Chapter 6. The addition is the illumination in the infra-red wavelength regime, where the frequency selection is performed by the IR AOTF with a range from 1100 - 1800 nm and the signal is detected by an InGaAs CCD (Vosskühler NIR-300 PGE). We show signal collected from complementary split rings (c-SRRs) in the gold film immersed in oil (Sigma 56822, n =1.516) with a high NA objective (NA=1.4). Fig. 7.3 (c) shows a Fourier space image of an array of c-SRRs with lattice spacing of 10 μm illuminated at 1550 nm with linearly polarized light along the x axis and analyzed with a circular polarizer for one handedness. Initial results indeed show that we can obtain a clear signal and asymmetry reversal under circular illumination. However, interpretation of the results is difficult due to the fact that according to simulations, the index matching liquid shifts the resonance towards the infra-red regime even beyond 1700 nm, i.e., outside the range of our Fourier microscope. Data on resonance can hence not be obtained. The asymmetry in the signal has been verified to not be an artefact, but come from the combined asymmetry of illumination and split ring orientation (52°). Upon reversing the illumination angle, the asymmetry in the signal in Fig. 7.3 (c) also reverses. In conclusion, we suggest that experiments involving c-SRRs would be a

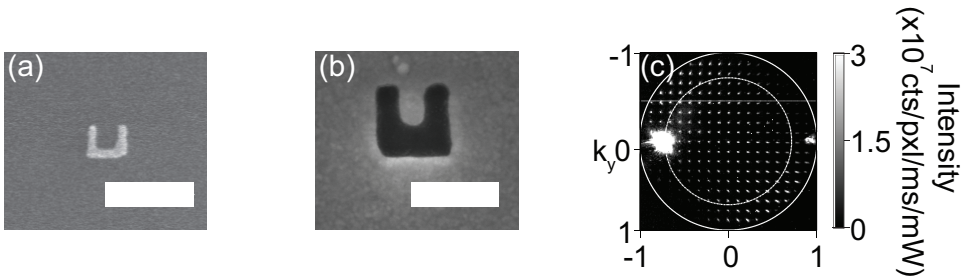

Figure 7.3: *(a) SEM image of a* $200 \times 200 \times 30$ *nm Au split ring on a glass substrate. Scale bar is 500 nm. (b) SEM image of a* $210 \times 210 \times 30$ *complementary split rings milled in a Au film. Scale bar is 250 nm. (c) Radiation pattern of an array of complementary split rings with a lattice spacing of 10* μ*m illuminated with* x*-polarized linear light and analyzed with a circular polarizer for one handedness. The bright spot on the left hand side of the back aperture image originates from the incident illumination* k*-vector at TIR angle. The dashed white line represents the vacuum light line, while the full white line is the NA of our objective (NA=1.4).*

good approach to measure radiation patterns, providing one can build a Fourier microscope that works in the range 1700 nm - 2500 nm wavelength. Due to hardware restrictions this is a daunting task, yet the only clear route to perform experiments with full control over the incident wavevector and polarization. These experiments could also be used to verify wether or not Babinet principle can be used at all to describe the response of complementary structures with the same magnetoelectric response formalism we developed for split rings, or whether e.g. plasmonic effects in the film spoil Babinet's principle.

7.1.2 Cathodoluminescence measurements

Radiation patterns might also be accessed by measuring the cathodoluminescence (CL) of split rings [14, 15]. CL spectroscopy has been used to demonstrate coupling and directivity of radiation of plasmonic structures such as ridge antennas, plasmonic whispering gallery cavities, ultrathin strip antennas and Yagi-Uda antennas [14, 16–20]. Recently, complementary measurements to CL based on electron energy loss spectroscopy (EELS) [21, 22] were demonstrated for single SRRs. We have attempted to measure radiation patterns of very small SRRs by utilizing CL. Since the CL system available at AMOLF is operational in the VIS, this requires very fine fabrication of 100×100 nm SRRs in Au layer. Therefore, we have fabricated arrays of $100 \times 100 \times 30$ nm SRRs on a silica-on-silicon substrate by e-beam

lithography as described in Chapter 2. The substrate choice is directly limited by the fact that only very few substrates provide background-free CL measurement capabilities. The SRRs are fabricated in an array with lattice spacing of 1200 nm as to ensure single SRR measurements. CL excitation maps are obtained by raster scanning the electron beam across the SRR, where the CL signal is spectrally analyzed on a silicon CCD camera [17]. In order to improve the signal to noise ratio, we have binned the data into 40 nm wavelength slices. Fig. 7.4 (a) shows a CL intensity map collected from a SRR at the wavelength range from 718 nm to 759 nm. As reported in transmission experiments, the fundamental mode of SRRs with such small dimensions ($100 \times 100 \times 30$ nm) on a dielectric substrate is found at $\lambda = 850$ nm, while higher order resonances appear at shorter wavelengths [23]. Fig. 7.4 (a) shows a distinct field distribution across the split ring, which we attribute to the second SRR mode [21, 22, 24]. The LC resonance is found at wavelengths where our detector reaches the end of its range.

Based on the above experiment, we extract the following recommendations for further experiments. Firstly, as regard detection, the current set up is equipped with a spectrometer operating in the VIS, that requires state-of-the art structure fabrication in order to shift the resonances to the VIS. Expanding the set up to the near-IR regime would benefit measurements on structures that are not easily scalable and are resonant in the IR. Secondly, as regards choice of material system, during the measurements subtle asymmetries arise when examining multiple SRRs, due to the presence of 'hot spots'. Evaporated Au is highly polycrystaline which is not suitable for fine structure fabrication where the fine features of the structure are of the same order as the crystal grain size of the Au layer. Therefore, we propose that a significant improvement could come from using Au SRRs fabricated from monocrystalline gold. Fig. 7.4 (c) shows such SRRs milled with a focused ion beam from monocrystalline gold flakes [25, 26], deposited on a 15 nm Si_4N_3 membrane (Norcada Inc.), as shown in Fig. 7.4 (b). Thirdly, the substrate choice should be carefully considered. CL measurements are extremely sensitive to background, for which reason, SiO_2 on Si, or just bare Si is always used as substrates. Unfortunately, this choice directly implies that the split ring would be right at a highly asymmetric dielectric interface that strongly changes the radiation pattern. An alternative would be to use ultrathin Si_4N_3 membranes, which are commercially available as substrate. The advantage is that for 50 nm membranes no background is generated, as electrons are simply transmitted. Unfortunatelly, initial measurements and calculations [27] indicate that even thin slabs of Si_4N_3 act as waveguides that capture most of the light radiated by the SRRs. While this poses a restriction on quantifying SRR physics per se, it at the same time could be highly interesting to study waveguide-coupled magnetoelectric antenna systems [28]. As a fourth recommendation, we anticipate that it is possible to avoid luminescence from a

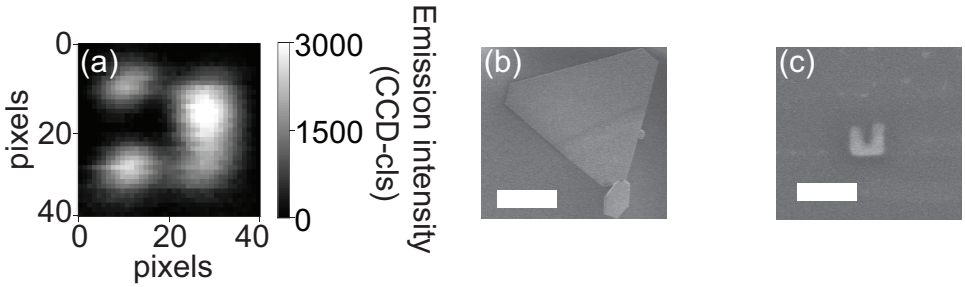

Figure 7.4: *(a) CL excitation map of split rings as a function of electron beam position. (b) SEM image of a monocrystaline Au flake on a Si_3N_4 membrane. Scale bar is 5 μm. (c) SEM image of a* $100 \times 100 \times 30$ *nm split ring milled with a focused ion beam from a Au flake deposited on a Si_4N_3 membrane [25, 26]. Scale bar is 200 nm.*

substrate and material choice by studying complementary SRRs in a gold film on top of a silica substrate. In this way, the Au film quenches the luminescence from the silica substrate.

7.2 Applications

Understanding the nature of the magnetoelectric response of metamaterial scatterers is essential for creating functional structures for future applications that rely on manipulating metamaterial responses. We strongly believe that the potential of metamaterial building blocks is not only limited to achieving negative refractive index. In this section we outline some applications which are inspired by coupling in arrays and optical activity of split ring resonators, by analogy with plasmonics.

The great appeal of plasmonic and metamaterial scatterers is the possibility of manipulating and controlling light propagation on a subwavelength scale due to strong photonic interaction in small physical volumes. For example, hallmark plasmonic structures exhibit localized field enhancement, such as in bow-tie antennas [29], or energy transfer via electric dipole-dipole far-field coupling in finite plasmonic antennas, for instance in dimer antennas, Yagi-Uda antennas, and Fano structures [30–35]. Arranging subwavelength plasmonic particles in linear arrays leads to enhancement and directivity of light emission from single molecules and quantum emitters that couple to such arrays [17, 29, 30, 32–34, 36]. Furthermore, periodic arrays of metallic nanostructures give rise to surface lattice resonances due to diffraction in the plane of the array [37]. It has been shown that by tuning localized plasmon resonances to overlap spectrally with diffractive resonances, one can create structures that enhance light emission brightness, rates and directivity

from single emitters and ensembles of emitters, such as semiconductor nanocrystals [38, 39]. Thereby, dipole-dipole and dark-bright mode coupling in plasmonic arrays is of importance for increasing the efficiency of light emitting devices, as well as in sensing.

In the proceedings of this thesis we have seen that metamaterial building blocks are, just like plasmonic structures, strong scatterers with large scattering cross sections that couple strongly in arrays. In analogy to plasmonics, one hence expects that functional structures can arise from coupling of induced electric and magnetic dipoles in split ring dimers, arrays or gratings. On the basis of their characteristics, we propose that metamaterial scatterers can add new features especially through their pseudochirality to many applications, including light sources, sensors, detectors, single-photon devices and thin optical components.

Sources Optical antennas provide an excellent way to couple photons in and out of nanoscale emitters [40]. Recently, Curto *et al.* have experimentally demonstrated directional emission from a single quantum emitter coupled to an optical Yagi-Uda antenna consisting of plasmonic particles [34]. In analogy to plasmonic structures, we propose that antennas made of split rings will result in directional light sources for photonic applications. Coupling in linear SRR arrays has been extensively studied for the microwave regime by Shamonina *et al.* [41], who have identified the existence of so-called magneto-inductive waves that arise due to dipole-dipole coupling of split rings, where the inter-ring spacing can be tuned to enable energy transfer along the antenna. Through magnetic, electric and magneto-electric dipole coupling, arrays of differently oriented split rings will exhibit bound guided modes with a complicated dispersion, that could furthermore be different for forward and backward modes [42, 43]. In addition to plasmonic structures, split rings exhibit optical activity that, combined with the prospect of directionality can result in directional sources of circularly polarized beams. Such an optically active antenna can be realized by arranging SRRs in an axial linear array with each SRR inclined at approximately 45 degrees to the axis. Due to alignment with the eigen-illumination directions, the directional lobe of the antenna is circularly polarized. Fig. 7.5 shows a schematic of the optically active photonic source driven by a molecule placed in the middle of the antenna. According to a simple calculation with our point dipole model, the radiation pattern shows equal emission distribution in the forward and backward directions with a 100:1 handedness contrast in each output beam. These types of antennas offer full polarization control of the outcoming beam that might serve to create sources in which directionality and handedness are coupled, and that spoof or selectively enhance magnetic transitions [3, 44]. An exciting prospect is to combine this control over photon spin with metamaterial antennas, with control over photon orbital angular momentum [45], which can be pos-

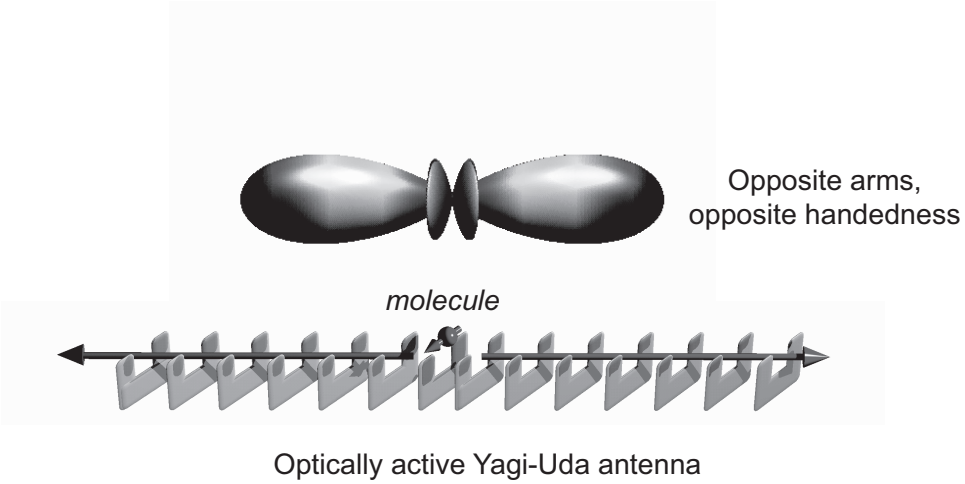

Figure 7.5: *Variation of a Yagi-Uda antenna based on coupling between split rings. Stacking split rings under an angle in which split rings exhibit optical activity can be used to generate handed sources driven by e.g. single molecules. Strong directivity of such antennas is seen in the radiation pattern.*

sibly obtained via nanoscale antenna versions of spiral phase plates. Creating such antennas could be an interesting route to obtain control over both spin-selection and orbital angular momentum selection rules in III-V quantum dots [46].

Sensor for enantiomers Split ring antennas may offer a new way to enhance circular dichroism detection of single enantiomers. A chiral molecule has a selective absorption for different handedness of circularly polarized light. Measuring circular dichroism, or a circular absorption contrast, via fluorescence detection of chiral molecule is difficult because of very low absorption cross section differences for different handedness of circularly polarized light. The difference has been reported to be less than one part per thousand [47]. Enhancing detection of molecular chirality via photonically induced chirality in the excitation field is expected to be of importance for e.g. spectroscopic discrimination of enantiomers that are known to have very different biological or pharmaceutical activity. This endeavour requires not only to optimize, but also to rethink the concept of handedness of the pump field, since in the near field the pump field will not be a transverse wave. We refer to Tang *et al.* [48] for a generalization of chirality in near fields.

Lasing spaser Recently, several groups have studied resonances of plasmonic and metamaterial scatterers in presence of gain as means to achieve lasing [49–53],

where feedback is not provided by mirrors, but by strong confinement in localized resonances. In order to reach lasing, one needs the gain to overcome the radiative and absorptive losses arising in the metallic structures. Zheludev *et al.* [54] suggested that spontaneously formed coherent current oscillations in metamaterial arrays coupled to a sufficiently strongly amplifying medium will lead to laser emission perpendicular to the metamaterial array. In Chapters 2 and 4 we have shown that lattice modes of magnetoelectric dipoles are in fact so strongly coupled to the forward direction, i.e., the $k_{||} = 0$ direction, that they show high radiative losses and superradiant broadening. Therefore, the key question is which modes, as classified by their parallel wavevector $k_{||}$, actually have the lowest loss. In Chapter 4 we presented a theory based on lattice sums that allows to classify the resonance frequency and damping of all the modes, taking all electromagnetic coupling mechanisms into account. We propose that calculating the complex dispersion relation using this theory would help to calculate both the radiative and the guided array modes [55] in search for the lowest loss mode.

Thin film filters and optical components As already proposed by Gansel *et al.* [56], thin films of 3D helices can be used as an analog of Hertz's linear polarizer, but for circular polarization generation. Our findings on optical activity of split rings have important consequences for such applications, where a circular polarizer can be realized by potentially simpler, 2D structures, due to the extinction dependence on the light handedness and incidence angle, at any wavelength. As previously suggested, the angular dependence means one can selectively transmit or block light of a certain handedness into specific angles, which could be used to make circular polarization beam splitters. Another exciting application of split ring arrays is as diffractive beam splitters, where arranging split rings in arrays with carefully engineered lattice spacings could be used to engineer all aspects of the polarization state of diffracted orders, both on the reflected and transmitted side of the grating. Such 2D arrays of SRRs could furthermore be directly imprinted on top of light emitting diodes (LEDs) to control emission polarization and directivity, similar to the application of diffractive plasmonic gratings [57]. Also, new forms of polarization control in integrated photonic platforms could be obtained, for instance by direct application of metamaterial lattices on top of vertical cavity surface emitting lasers (VCLSs), as well as on top of integrated photodetectors.

Bibliography

[1] R. Merlin, Proc. Natl. Acad. Sci. U.S.A. **106**, 6 (2009).

[2] B. C. Buchler, T. Kalkbrenner, C. Hettich, and V. Sandoghdar, Phys. Rev. Lett. **95**, 063003 (2005).

[3] S. Karaveli and R. Zia, Phys. Rev. Lett. **106**, 193004 (2011).

[4] M. L. Andersen, S. Stobbe, A. S. Sørensen, and P. Lodahl, Nature Physics **7**, 215 (2011).

[5] L. Novotny and B. Hecht, *Principles of Nano-Optics*, Cambridge University Press, UK (2006).

[6] We use a Lorentzian model including radiation damping, so polarizabilities are actually complex. Quoted values are the on-resonance magnitudes.

[7] W. Lukosz and R. E. Kunz, J. Opt. Soc. Am. **67**, 1615 (1977).

[8] W. Lukosz and R. E. Kunz, J. Opt. Soc. Am. **67**, 1607 (1977).

[9] W. Lukosz and R. E. Kunz, J. Opt. Soc. Am. **69**, 1495 (1979).

[10] W. Lukosz and R. E. Kunz, J. Opt. Soc. Am. **71**, 744 (1981).

[11] N. Liu, H. Liu, S. N. Zhu, and H. Giessen, Nature Photonics **3**, 157 (2009).

[12] T. Zentgraf, T. P. Meyrath, A. Seidel, S. Kaiser, H. Giessen, C. Rockstuhl, and F. Lederer, Phys. Rev. B **76**, 033407 (2007).

[13] C. Rockstuhl, T. Zentgraf, T. P. Meyrath, H. Giessen, and F. Lederer, Opt. Expr. **16**, 2080 (2008).

[14] T. Coenen, E. J. R. Vesseur, and A. Polman, Appl. Phys. Lett. **99**, 143103 (2011).

[15] T. Suzuki and N. Yamamoto, Opt. Exp. **17**, 23664 (2009).

[16] M. Kuttge, E. J. R. Vesseur, A. F. Koenderink, H. J. Lezec, H. A. Atwater, F. J. García de Abajo, and A. Polman, Phys, Rev. B **79**, 113405 (2009).

[17] T. Coenen, E. J. R. Vesseur, A. Polman, and A. F. Koenderink, Nano Lett. textbf11, 3779 (2011).

[18] T. Coenen, E. J. R. Vesseur, and A. Polman, ACS Nano **6**, 1742 (2012).

[19] E. J. R. Vesseur and A. Polman, Nano Lett. **11**, 5524 (2011).

[20] E. S. Barnard, T. Coenen, E. J. R. Vesseur, A. Polman, and M. L. Brongersma, Nano Lett. **11**, 4265 (2011).

[21] G. Boudarham, N. Feth, V. Myroshnychenko, S. Linden, J. García de Abajo, M. Wegener, and M. Kociak, Phys. Rev. Lett. **105**, 255501 (2010).

[22] F. von Cube, S. Irsen, J. Niegemann, C. Matyssek, W. Hergert, K. Busch, and

S. Linden, Opt. Mat. Exp. **1**, 1009 (2011).
[23] A. de Hoogh, B. Hommersom, and A. F. Koenderink, Opt. Express **19**, 11405 (2011).
[24] T. Zentgraf, J. Dorfmüller, C. Rockstuhl, C. Etrich, R. Vogelgesang, K. Kern, T. Pertsch, E. Lederer, and H. Giessen, Opt. Lett. **33**, 848 (2008).
[25] Z. Guo, Y. Zhang, Y. DuanMu, L. Xu, S. Xie, and N. Gu, Colloids and Surfaces A: Physicochem. Eng. Aspects **278**, 33 (2006).
[26] J. Huang, V. Callegari, P. Geisler, C. Brüning, J. Kern, J. C. Prangsma, X. Wu, T. Feichtner, J. Ziegler, P. Weinmann, M. Kamp, A. Forchel, P. Biagioni, U. Sennhauser, and B. Hecht, Nature Comm. **1**, (2010).
[27] H. P. Urbach and G. L. J. A. Rikken, Phys. Rev. A **57**, 3913 (1998).
[28] F. Bernal Arango, and A. F. Koenderink, *in preparation*
[29] A. Kinkhabwala, Z. Yu, S. Fan, Y. Avlasevich, K. Müllen, and W. E. Moerner, Nature Photonics **3**, 654 (2009).
[30] O. L. Muskens, V. Giannini, J. A. Sánchez-Gil, and J. Gómez Rivas, Nano Lett. **7**, 2871 (2007).
[31] J. Li, A. Salandrino, and N. Engheta, Phys. Rev. B **76**, 245403 (2007).
[32] T. H. Taminiau, F. D. Stefani, and N. F. van Hulst, Opt. Expr. **16**, 10858 (2008).
[33] A. F. Koenderink, Nano Lett. **9**, 4228 (2009).
[34] A. G. Curto, G. Volpe, T. H. Taminiau, M. P. Kreuzer, R. Quidant, and N. F. van Hulst, Science **329**, 930 (2010).
[35] B. Luk'yanchuk, N. I. Zheludev, S. A. Maier, N. J. Halas, P. Nordlander, H. Giessen, and C. T. Chong, Nature Mat. **9**, 707 (2010).
[36] S. Kühn, U. Håkanson, L. Rogobete, and V. Sandoghdar, Phys. Rev. Lett. **97**, 017402 (2006).
[37] S. R. K. Rodriguez, A. Abass, B. Maes, O. T. A. Janssen, G. Vecchi, and J. Gómez Rivas, Phys. Rev. X **1**, 021019 (2011).
[38] S. R. K. Rodriguez, O. T. A. Janssen, A. Abass, B. Maes, G. Vecchi, and J. Gómez Rivas, arxiv.org:1110.3260v1
[39] S. R. K. Rodriguez, G. Lozano, M. A. Verschuuren, R. Gomes, K. Lambert, B. De Geyter, A. Hassinen, D. Van Thourhout, Z. Hens, and J. Gómez Rivas, Appl. Phys. Lett. **100**, 111103 (2012).
[40] H. Giessen and M. Lippitz, Science **329**, 910 (2010).
[41] E. Shamonina and L. Solymar, J. Phys. D: Appl. Phys **37**, 362 (2004).
[42] O. Sydoruk, O. Zhuromskyy, E. Shamonina, and L. Solyimar, Appl. Phys. Lett. **87**, 072501 (2005).
[43] H. Liu, Y. M. Liu, T. Li, S. M. Wang, S. N. Zhu, and X. Zhang, Phys. Stat. Solid. B **246**, 1397 (2009).
[44] S. Karaveli and R. Zia, Opt. Lett. **35**, 3318 (2010).

[45] J. Berkhout, *Fundamental methods to measure the orbital angular momentum of light*, PhD thesis, Leiden University, 2011.
[46] G. F. Quinteiro and P. I. Tamborenea, Phys. Rev. B **79**, 155450 (2009).
[47] Y. Tang and A. E. Cohen, Science **332**, 333 (2011).
[48] Y. Tang and A. E. Cohen, Phys. Rev. Lett. **104**, 163901 (2010).
[49] D. J. Bergman and M. I. Stockman, Phys. Rev. Lett. **90**, 027402 (2003).
[50] S. Wuestner, A. Pusch, K. L. Tsakmakidis, J. M. Hamm, and O. Hess, Phil. Trans. R. Soc. A **369**, 3525 (2011).
[51] J. M. Hamm, S. Wuestner, K. L. Tsakmakidis, and O. Hess, Phys. Rev. Lett. **107**, 167405 (2011).
[52] S. Wuestner, A. Pusch, K. L. Tsakmakidis, J. M. Hamm, and O. Hess, Phys. Rev. Lett. **105**, 127401 (2010).
[53] M. A. Noginov, G. Zhu, A. M. Belgrave, R. Bakker, V. M. Shalaev, E. E. Narimanov, S. Stout, E. Herz, T. Suteewong, and U. Wiesner, Nature Lett. **460**, 1110 (2009).
[54] N. I. Zheludev, S. L. Prosvirnin, N. Papasimakis, and V. A. Fedotov, Nature Photonics **2**, 351 (2008).
[55] A. F. Koenderink and A. Polman, Phys. Rev. B **74**, 033402 (2006).
[56] J. K. Gansel, M. Thies, M. S. Rill, M. Decker, K. Bade, V. Saile, G. von Freymann, S. Linden, and M. Wegener, Science **325**, 1513 (2009).
[57] J. Gómez Rivas, G. Vecchi and V. Giannini, New J. Phys. **10**, 105007 (2008).

Summary

Research in the field of metamaterials is driven by the possibility to create materials with optical properties, such as electric permittivity ϵ and magnetic permeability μ, that can be tuned arbitrarily, unlike naturally occurring materials that offer only a limited range of responses to light. This allows for exciting applications that are based on phenomena such as negative refraction and arbitrary rerouting of light through space. Realizing arbitrary optical parameters is far from trivial and requires a fundamental understanding of metamaterial building blocks.

In general, metamaterials are made by fabricating dense arrays of building blocks that exhibit a response to both electric, as well as magnetic fields of light. Split ring resonators (SRRs) are metamaterial building blocks known to exhibit magnetic resonances in the visible and infra-red regime. Thus far, arrays of split rings have been considered as effectively homogeneous media with effective ϵ and μ. In this thesis we show that single SRRs are in fact strong scatterers, with cross sections exceeding their physical volume so that metamaterials should rather be viewed as strongly scattering media. Due to their large scattering cross sections, we expect split rings to couple strongly in arrays and give rise to interesting radiation patterns. To this end, we have performed optical measurements on arrays of metamaterial scatterers and developed an electrodynamic point dipole theory to quantify the electric and magnetic responses captured by the polarizability α.

In Chapter 2, we present experimental observations of strong electric and magnetic interactions between split rings at 1.4 μm. Using electron beam lithography, we fabricated gold split rings on glass substrates arranged in periodic arrays. Our transmission measurements show blueshifts and redshifts of the magnetic resonance, depending on split ring orientation relative to the lattice. The shifts are the first evidence for magnetic dipole-dipole coupling at optical frequencies in planar split ring arrays. We also find that these interactions induce superradiant broadening of the resonance, accompanied by a decrease in effective cross section per split ring with increasing density.

In Chapter 3, we derive a fully electrodynamic point scattering theory to quantify the scattering behavior of arbitrary systems of point-like magnetoelectric scatterers. We have taken proper account of reciprocity and radiation damping for electric and magnetic scatterers with any general polarizability tensor. Specifically, we show how reciprocity and energy balance put constraints on the electrodynamic

polarizability tensor and predict which set of experiments will provide full information about all the terms in the polarizability tensor. We show how the differential scattering cross section can be translated back to retrieve split ring polarizabilities and magnetoelectric cross polarizabilities. Our theory sheds new light on cross sections, pesudo-chirality, and differential scattering cross sections of split ring scatterers and stereodimers of split rings.

In Chapter 4, we use the 6x6 dyadic Green function to analytically solve for the response of finite periodic arrays, allowing us to simply predict their transmission and reflection. We show that all features of transmission measurements on split ring arrays are quantitatively reproduced by our electrodynamic model, including resonance peak shifts due to electric and magnetic dipole coupling and resonance broadening due to superradiant damping.

In Chapter 5 we experimentally demonstrate a surprising result that geometrically non-chiral split rings exhibit chirality in their optical response. Predicted by our electrodynamic model, strong magnetoelectric coupling in the polarizability of split rings implies optical activity for all magnetoelectric scatterers whose response can be described by a single equation of motion derived from circuit theory. Optical activity offers an additional route to achieving transparency for one handedness and angle of incidence, while it results in strong scattering for the reverse handedness and incidence.

In Chapter 6, we present a custom built Fourier microscope to image radiation patterns of single nanoscatterers. Although plasmonic and metamaterial building blocks have extinction cross section exceeding their geometrical area, the intensities scattered by single structures are low compared to the incident field, making them exceptionally difficult to detect. In this chapter we report on a background free experimental technique in which the sample is excited by means of total internal reflection and the angular distributions of scattered light is retrieved from microscope back-aperture imaging. To demonstrate the operation of our set up, we present measurements on gold nanorods and show that they have a radially polarized single dipole radiation pattern. Our dark-field microscope is excellently suited for measuring angular distribution of light of metamaterial and plasmonic scatterers with small absolute cross sections that are expected to have anisotropic radiation patterns due to magnetoelectric coupling.

In Chapter 7, we present a set of measurements that will challenge the point dipole view of metamaterial building blocks and propose applications beyond negative refraction of such magneto-electric scatterers. We theoretically study how one can measure radiation patterns of split rings and split ring stereodimers, thereby proving, or disproving, our magnetoelectric theory. We present the difficulties that such experiments will entail. In addition, we present suggestions to demonstrate the magnetoelectric character of split rings by utilizing cathdoluminescence exper-

iments, as well as resorting to experiments that rely on Babinet's principle. Finally, we suggest applications of split rings that extend beyond achieving negative refractive index and transformation optics, such as in lighting, sensing and as thin film optical components.

Samenvatting

Licht kan beschreven worden als een golf die bestaat uit een elektrisch en magnetisch veld. Natuurlijke materialen koppelen alleen met licht via het elektrisch veld met een sterkte die beschreven wordt door de elektrische permitiviteit ϵ. Metamaterialen zijn kunstmatige materialen die ook aan het magnetisch veld van licht koppelen, beschreven door een magnetische permeabiliteit μ. Nanofotonica onderzoek aan metamaterialen is met name gedreven door de mogelijkheid om metamaterialen te ontwerpen waarvan zowel ϵ als μ naar believen aangepast kan worden. Deze materialen zouden tot nieuwe toepassingen kunnen leiden die gebaseerd zijn op fenomenen zoals negatieve brekingsindex en het willekeurig afbuigen van licht. Het realiseren van zulke materialen is echter niet eenvoudig, zonder een fundamenteel begrip van de bouwstenen van metamaterialen. In het algemeen worden metamaterialen gemaakt door het fabriceren van nanodeeltjes die een elektrische en magnetische respons op licht hebben, geordend in een dicht rooster. Een 'split ring resonator' (SRR) is een voorbeeld van een bouwsteen voor metamaterialen die zo een respons in het zichtbaar en infrarood deel van het spectrum heeft. Tot nu toe is in de literatuur een rooster van SRRs als een homogeen medium met een effectieve ϵ en μ beschouwd. In dit proefschrift laten we zien dat een enkele SRR in feite een sterke licht verstrooier is, met een verstrooiingsdoorsnede groter dan zijn fysiek oppervlak. Vanwege deze eigenschap verwachten we dat SRRs een sterke interactie met elkaar hebben. Om dit te bewijzen hebben we optische experimenten gedaan aan periodieke roosters van SRRs, en hebben we een elektrodynamische theorie ontwikkeld die een SRR beschrijft als een elektrische alsmede magnetische dipool. Met deze theorie kunnen we de elektrische en de magnetische respons van SRRs kwantificeren. We verwachten dat deze responsen aanleiding zullen geven tot interessante stralingspatronen.

In Hoofdstuk 2, bespreken we onze experimentele waarneming van sterke elektrische en magnetische interactie tussen SRRs in het nabije infrarood. Met behulp van elektronen bundel lithografie hebben we gouden SRRs op een glazen substraat gemaakt, geordend in roosters. Transmissiemetingen aan roosters van verschillende vorm en dichtheid laten frequentie verschuivingen zien van de magnetische resonantie. Deze verschuivingen van de resonant respons zijn het eerste bewijs van sterke interactie tussen magnetische dipolen in vlakke roosters van SRRs. Deze interacties zijn ook zichtbaar in de verbreding van de resonante respons, en de ver-

mindering van de effectieve doorsnede van een SRR met de toename in dichtheid.

In Hoofdstuk 3, leiden we een volledig elektrodynamische theorie af om het verstrooiingsgedrag van willekeurige systemen van magnetoelektrische dipolen, zoals SRRs, te kwantificeren. Deze theorie is gebaseerd op reciprociteit en energie behoud en stelt grenzen aan de algemene polariseerbaarheidstensor, welke de basis vormt van de magnetoelektrische respons. Met deze theorie kunnen we effectieve doorsneden, pseudochiraliteit in de respons op circulair gepolariseerd licht, en de richting in welke SRRs licht verstrooien berekenen.

In Hoofdstuk 4, maken we gebruik van voornoemde elektrodynamische theorie om transmissie en reflectie van oneindige periodische roosters van magnetoelektrische verstrooiers te voorspellen. De frequentieverschuiving en verbreding van de resonante respons gemeten in hoofdstuk 2 wordt succesvol gereproduceerd met ons model.

In Hoofdstuk 5, laten we zien dat geometrisch niet-chirale SRRs een asymmetrische optische respons hebben die, afhankelijk van de invalshoek, sterk afhangt van de draaizin van inkomend circulair gepolariseerd licht. Deze opvallende 'optische activiteit' komt door sterke koppeling tussen de magnetische en elektrische termen in de polariseerbaarheidstensor voor SRRs, zoals voorspeld door onze elektrodynamische theorie. We concluderen dat zo'n asymmetrische respons noodzakelijkerwijs optreedt voor alle magnetoelektrische verstrooiers die beschreven kunnen worden met een enkele bewegingsvergelijking afgeleid uit de benadering dat de strooier een platte resonante stroomkring is. De asymmetrische respons betekent dat de dipolen licht sterk verstrooien bij een bepaalde draaingsrichting van de polarisatie van het licht en hoek van inval, terwijl ze bij dezelfde draaizin geen licht verstrooien voor een complementaire hoek van inval.

In Hoofdstuk 6, wordt een zelfgebouwde Fourier microscoop beschreven. Deze microscoop kan het verstrooiingspatroon (differentiele werkzame strooingsdoorsnede) van een enkele nanoverstrooier afbeelden. Zulke stralingspatronen zijn moelijk detecteerbaar, omdat de verstrooier een heel zwak signaal geeft vergeleken met het invallende licht waar het mee aangeslagen wordt. Onze microscoop biedt een achtergrondvrije techniek waarin de verstrooier aangeslagen wordt in totale interne reflectie. De hoekverdeling van het verstrooide licht is meetbaar door te kijken naar de 'back aperture' van het microscoop objectief. Om de functionaliteit van onze microscoop te demonstreren, laten we resultaten van metingen aan gouden nanostaafjes zien. In vergelijking met SRRs bestaan deze nanodeeltjes uit alleen elektrische dipolen, zoals de gemeten verstrooingspatronen aantonen. Onze microscoop kan gebruikt worden om de hoekverdeling van het verstrooide licht te meten van magnetoelektrische verstrooiers die een asymmmetrisch verstrooingspatroon hebben.

In Hoofdstuk 7, testen we onze elektrodynamische theorie en we stellen toepasingen voor van magnetoelektrische verstrooiers, naast voornoemde negatieve brek-

ingsindex. Zo stellen we voor dat onze theorie nader getest kan worden door verstrooingspatronen van SRRs te meten. We hebben deze patronen theoretisch berekend voor de realistische experimentele situatie dat de SRRs zich op een glas substraat bevinden. We bespreken welke problemen we in zulke experimenten verwachten. Daarom stellen we ook alternatieve routes voor om het magnetoelektrische karakter van SRRs te demonstreren met behulp van cathodoluminescentie of met het principe van Babinet. Tot slot stellen we toepassingen voor die gebruik maken van de sterke interactie in roosters én de asymmetrische optische respons van SRRs, in verlichting, sensoren en optische componenten van dunne lagen.

Acknowledgments

Looking back to the four years spent at AMOLF, there are many people who were directly and indirectly involved in the making of this little book. The following paragraphs name some of the people whom I would like to thank for contributing to this work with their knowledge and experience. First of all, I would like to thank my supervisor Femius. I have learned a lot from you about Matlab, about scattering, and amongst others, about clocks. Furthermore, I would like to thank Albert Polman for always being supportive and eternally optimistic, Kobus Kuipers for his advice and endless interest in the wellbeing of students, and Ad Lagendijk for inspiring scientific discussions. I would like to thank the group of Resonant Nanophotonics: Martin, Andrej, Felipe, Abbas, Lutz, Hinke, and two master's students, Christelle and Marie-Anne, for their contributions and fruitful discussions during group meetings and journal clubs. I appreciate numerous opportunities the group had to join meetings of the aforementioned group leaders, it was the most dynamic manner in which a starting PhD student could learn and exchange ideas. Therefore, I would like to thank the members of these groups for their valuable input.

Doing a PhD would be almost impossible without the support staff that always strives to do their best. Thank you Marko, Leon, the Amsterdam nanoCenter: Chris, Dimitry, Johan, Gijs, and Hans for being a great manager and for creating a very pleasant working atmosphere, Hinco for exotic lunch topics and awesomeness, Sjoerd, Marco Konijnenburg and Frank from the software engineering group, the design department, mechanical workshop, electronic engineering department, ICT department, secretaries, communications department, Anouk, Wouter and Nelly for their efficiency and readiness to help, facilities service department, the canteen staff, and Esther, Betty, Juliette, Marjo, and Ad for being the most pleasant people to meet upon arriving at AMOLF in the morning.

During my PhD I have had the opportunity to venture into a patent formulation, for which I would like to thank the Nanosoil team, it was a fun ride and a good experience: Timmo, Jochen, Marjon and Niels, and of course Bart van Leijen for mental and financial support. Throughout the four years I had the privilege to share offices with post-docs that I would like to thank for sharing their knowledge, advice, and for making it all a lot of fun: Tobias, Robb, Patrick, Nir and Per. You were wonderful! A special thanks goes to Dries, Ewold and Jean from whom I

learned a lot. I would like to thank Marko (Snezana), Bergin (Dashurie), Jochen (Gertrude), and Ronald (Your Mother) - I can only repeat what a wise man once said: with our adventures we could write a novel! Lots of persistent measurements, concentration, and sitting behind the computer would not be the same if it was not for back pains, neck pains and other aches - thank you Muck for you support, and for making mine better. Finally and most importantly, I would like to thank my parents Vlado and Mirjana, my sister Jasna, and Gijs for their immense support, understanding, and love.